TÉCNICO LISBOA

Experimental characterization of pedestal density fluctuations and correlation with pedestal evolution on JET

Daniel José Lopes da Costa

Thesis to obtain the Master of Science Degree in

Engineering Physics

Supervisor: Prof. Carlos Alberto Nogueira Garcia da Silva

Examination Committee

Chairperson: Prof. Horácio João Matos Fernandes
Supervisor: Prof. Carlos Alberto Nogueira Garcia da Silva
Member of the Committee: Prof. Rui Miguel Dias Alves Coelho

March of 2021

Aos meus pais e amigos.

Acknowledgments

There are many people that made this thesis possible that I would like to thank. All of them made this strange period of our lives much more bearable.

Many thanks to my supervisor Carlos Silva, for helping me throughout my work, guiding me through the many obstacles and helping me explore this theme. Also to IPFN for hosting me in this thesis.

I appreciate my dog Sigma for keeping me company and for the regular walks that helped me stay focused.

I cherish my friends for keeping me company online and helping me clear my mind. Even though we were all separated, hanging out virtually every once in a while kept me motivated and happy. I also enjoyed a lot the trails exploration with some of them that broke the routine and let me breath some fresh air.

Finally, I would like to say that I deeply valued what my parents did for me during these hard times, they provided a welcoming home and were supportive throughout this long project.

Resumo

Fusão nuclear controlada é uma fonte segura e abundante de energia que pode ajudar a equilibrar o mix energético de futuras gerações. Atualmente, os melhores resultados são obtidos de tokamaks que confinam um plasma magneticamente e aquecem-no a temperaturas acima de 100 milhões de graus Celsius. O modo de operação preferível para tokamaks é o modo H, que, apesar de fornecer confinamento melhorado, é preocupante devido ao aparecimento de instabilidades como Edge Localised Modes (ELMs). Estes eventos não apenas danificam componentes das paredes, mas também não permitem o plasma de alcançar temperaturas e densidades críticas para ocorrer fusão. Perceber as instabilidades que causam ELMs é bastante importante e foi um dos objetivos desta tese. Um conjunto de 3 descargas do JET foram analisadas através de um sistema de reflectometria de micro-ondas a operar em modo Doppler. Este diagnóstico permite estudar flutuações de densidade, δn_e, na periferia do plasma. Neste trabalho diferentes métodos numéricos foram aplicados e foi desenvolvida uma forma de caracterizar um modo coerente no δn_e da periferia do plasma. O foco deste estudo foi em perceber o comportamento geral de um modo específico assim como determinar a sua localização. Reparamos que a intensidade do modo estava mais correlacionada com a evolução da densidade em vez da temperatura. Caracterizamos o modo entre ELMs com frequência à volta de 80 kHz, que estava localizado na metade superior da região de gradiente elevado. A sua frequência tendeu a decrescer conforme o raio aumenta.

Palavras-chave: ELM, modo H, reflectometria, flutuações de densidade, plasma.

Abstract

Controlled nuclear fusion is a safe and abundant energy source that may help balance the energy mix of future generations. Currently, the best results are obtained in tokamaks that magnetically confine a plasma heated to temperatures over 100 million degrees Celsius. The preferable mode of operation for tokamaks is the H-mode, that although provides improved confinement, is worrying because of the emergence of instabilities such as Edge Localised Modes (ELMs). Not only do these events damage the wall components, but they may also inhibit the plasma from reaching the critical densities and temperatures required for fusion. Understanding the instabilities causing ELMs is rather important and was one of this thesis' objectives. A set of three discharges from JET were analysed through a microwave reflectometry system operating in Doppler mode. This diagnostic allows the studying of density fluctuations, δn_e, at the plasma edge. In this work different numerical methods were applied and a method was developed to characterize a coherent mode in δn_e. The focus of the study was on both understanding the general behaviour of a specific mode as well as determining its location. We noted that mode intensity was more correlated with density evolution rather than temperature. We characterised the mode between ELMs with frequency around 80 kHz and located around the upper half of the steep gradient region. Its frequency tended to decrease as the radius increased.

Keywords: ELM, H-mode, reflectometry, density fluctuations, plasma.

Contents

List of Tables

List of Figures

List of Abbreviations

ELM	Edge Localized Mode
H-mode	High confinement mode
L-mode	Low confinement mode
NBI	Neutral Beam Injection
ILW	ITER like wall
B_t	Toroidal Magnetic Field
I_p	Plasma Current
δ_{n_e}	Electron density fluctuations
HFS	High Field Side
LFS	Low Field Side
P_{LH}	Power threshold for the L-H transition
m	Poloidal mode number
n	Toroidal mode number
PF	Probing Frequency
savgol	Savitzky-Golay
CR	Correlation Reflectometer
ETB	Edge Transport Barrier

Chapter 1

Introduction

Mankind has seen great improvements in standards of living due to advancements in many areas. From science, technology and health, to transport and accessibility to goods. However, developments in these fields came at the cost of overuse of natural resources and unsustainable production of electricity. Energy demand is prospected to increase by nearly 50 percent between 2018 and 2050[1]. Therefore, research and development for a clean and abundant energy source is crucial.

1.1 World Energy Consumption

Understanding how unsustainable our energy production has become can be seen in figure 1.1. It gives the time evolution of our energy production mix. Fossil fuels such as oil, natural gas and coal make up nearly three fourths of the current global energy mix.

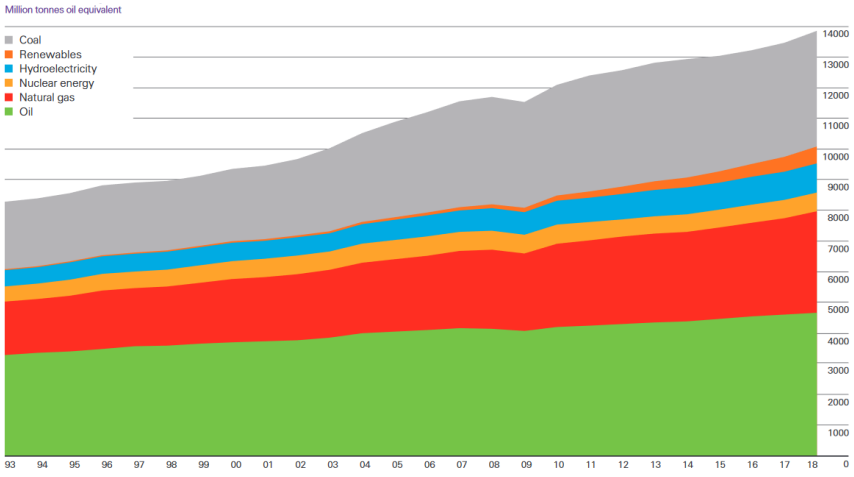

Figure 1.1: Global energy consumption (1993-2018) [2]

The present and foreseeable future energy mix is problematic for two major reasons: (i) fossil fuels are non renewable, so once we deplete our reserves, an energy crisis will ensue; and (ii) the IPCC[1] concluded that there is over 95% probability that resultant gases from the burning of fossil fuels have caused the

[1] Intergovernmental Panel on Climate Change

increase in Earth's temperature[3]. The correlation between the increase in concentration of CO_2 and the abnormality in global temperatures is visible in figure 1.2.

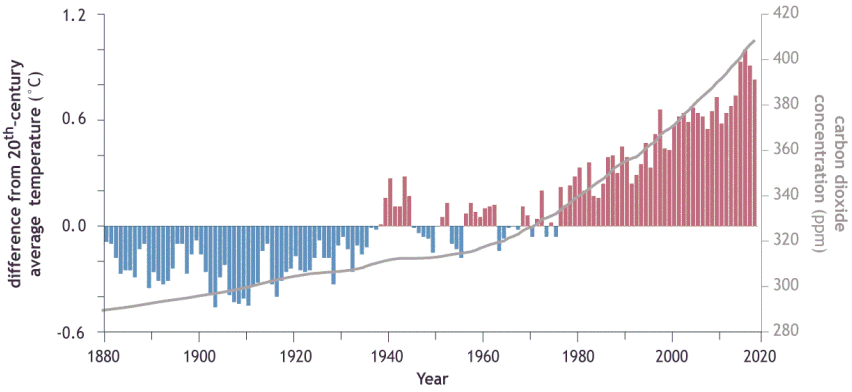

Figure 1.2: Atmospheric carbon dioxide and Earth's surface temperature (1880-2018) [4]

The most commonly proposed alternatives to phase out fossil fuels are renewables and nuclear fission. Although they will be the principal contributors to face climate change, they may not be reliable enough to sustain humanity's energy needs in the long term.

Renewable energy has significant drawbacks. They have an intermittency problem as they highly rely on the weather. Intermittency requires massive storage capabilities so that the energy surplus can be stored and then used at moments of lower energy production. Although storage of energy is still expensive, it may improve with time. Finally, these energy sources depend highly on geographic limitations, implying that not all countries have the capabilities to sustain themselves solely on this type of energy production. This can lead to inequality and dependence[5].

Nuclear fission energy has the downsides of being non renewable, since it depends on fuel reserves, and also of producing radioactive waste that lasts for centuries. Nuclear fission can also be dangerous in the wrong hands, leading to the manufacture of nuclear weapons (nuclear proliferation).

An energy solution that could help solve these problems may be in nuclear fusion.

1.2 Controlled Nuclear Fusion

Nuclear fusion occurs when two lighter atoms join to form a heavier one. The resultant particles' mass is smaller than the sum of lighter atoms' masses, with the missing mass from this reaction being released as kinetic energy.

For these two lighter atoms to join, they must overcome the inter-particle Coulomb potential. A strong repulsive force that increases as two positively charged nuclei come closer. The Coulomb force diverts the orbits of the particles and results in a less likelihood of nuclear reaction. A way to surpass this problem is to give particles sufficiently high kinetic energy, so that the repulsive force is surpassed. This implies reaching very high temperatures, in the order of 150 million degrees Celsius, corresponding to 10 times the temperature of the sun's core.

The aim of nuclear fusion research is to achieve these reactions on earth and harness the extra energy

it produces. There are many reactions that can achieve fusion, but the most interesting are the ones that require relatively low temperatures. The reaction most suitable, nowadays, is the Deuterium-Tritium reaction given by 1.1. It satisfies the temperature condition and has high energy output.

$$\mathrm{D} + \mathrm{T} \rightarrow \alpha + \mathrm{n} + 17.6 \text{ MeV} \tag{1.1}$$

Deuterium is a stable isotope of hydrogen, with one extra neutron in its nucleus. Tritium is an unstable isotope of hydrogen that has two extra neutrons. Joining these isotopes results is an α-particle, He^{2+}, and a neutron with 3.5 MeV and 14.1 MeV of kinetic energy, respectively.

To fuel this reaction, we can easily extract deuterium from the ocean, making it a virtually unlimited supply of inexpensive fuel. The reaction also requires tritium, which there is no natural supply of on earth. Any reserves would not endure the 12.26 years half-life. To solve this problem, engineers and physicists found a way of breeding tritium within the fusion reactor. To achieve that, we require a lithium supply, whose known reserves are sufficiently large to last thousands of years. Concerns of fuel availability for fusion reactors are not the most important issue [6].

As mentioned before, fusion requires such high temperatures that cause the appearance of a new state of matter known as plasma. A plasma is a gas of ions and free electrons having collective behavior. To reach the high temperatures required for nuclear fusion, the plasma must be contained in a vessel. There must be the least contact between vessel material and the plasma to avert damage or energy dissipation. Wall contact is avoidable considering that plasma, being made up of positive nuclei and negative electrons, can be influenced by magnetic fields. This is the basic principle of magnetic confinement.

A tokamak is the most promising configuration using magnetic confinement, visible in figure 1.3. It consists of a torus shaped vessel, in which the plasma is confined through the imposed magnetic field. The main magnetic components present are toroidal and poloidal: toroidal field created by external toroidal field coils; poloidal field generated by a toroidal current induced in the plasma. This current is obtained through electromagnetic induction by varying the current within the inner poloidal field coils (primary coil). The primary coil and the plasma are comparable to the primary and secondary windings of a circuit transformer. For plasma shaping and position control there are poloidal field coils.

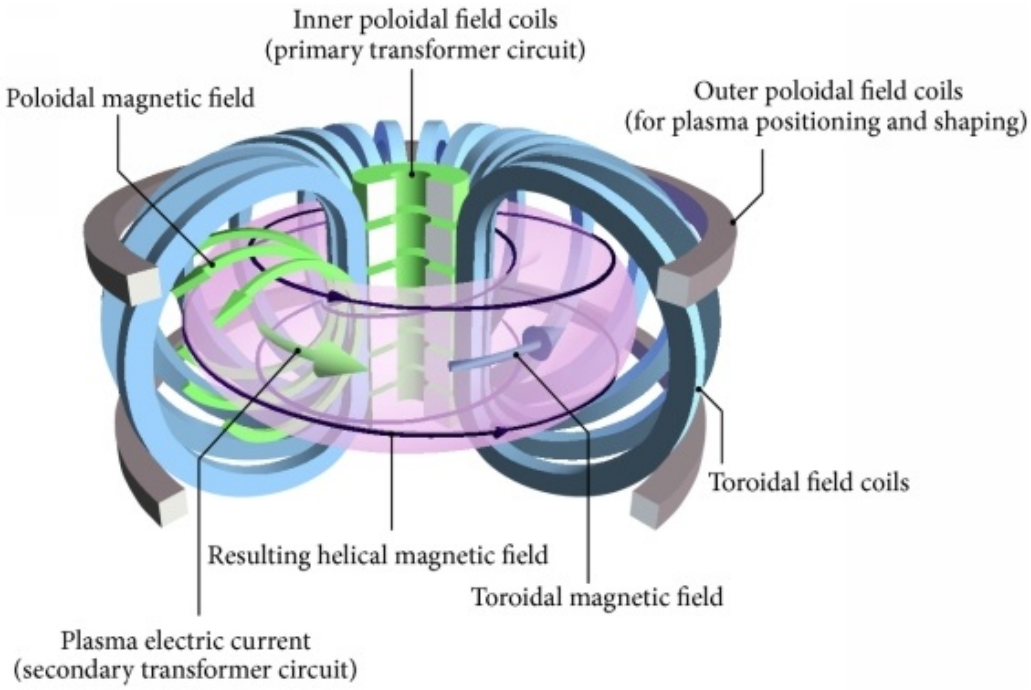

Figure 1.3: Schematic of a tokamak configuration and the associated magnetic field lines [7]

In a D-T plasma, initially, an external heating source is required to increase the temperature to fusion levels. However, once this temperature is achieved, the α particles also provide heating, when confined. This reduces need for external heating and the plasma can eventually be sustained by internal heating. At this point of self sustainable fusion we call ignition. The minimum conditions for ignition of this reaction are of $T_{min} = 15$ keV, and $(p\tau_E)_{min} = 8.3$ atm s.

The motivation to get this technology working are immense:

- The abundance of energy provided. When fusing atoms in a controlled manner, 4 million times more energy is released than burning fossil fuels and 4 times as much as a nuclear reaction, using the same mass.
- Fusion fuels' reserves are practically limitless.
- When these reactions occur, they do not emit harmful toxins like carbon dioxide or other greenhouse gases. The major component expelled is the inert and non-toxic gas, helium. This makes fusion a very environmental option.
- The type of fusion reactor to be built commercially is a safe reactor. It is very difficult to reach some uncontrollable fusion chain reaction since any strong disturbance to the plasma can easily lead to a disruption of the plasma (sudden energy and particle loss). This implies it does not promote situations of meltdown and radioactive risk presented by fission reactors. Even though there is toxic waste production, it is of low activity and not long lived nuclear waste.
- It presents a power output and an electricity price similar to the one of a fission reactor, without all its inconveniences [8].

The most recent project being worked on progressing the fusion goal on earth is ITER. A large scale, international experiment with the purpose of demonstrating scientific and technological feasibility of fusion as an energy source. It will allow the study of plasmas in similar conditions to the ones in fusion power plants, while also testing new technologies for fusion, such as heating, control, diagnostics and remote maintenance [9]. This project is being executed in collaboration with the European Union, India, Japan, China, Russia, South Korea and the United States.

1.3 Motivation and thesis outline

Advancing nuclear fusion into a state of commercial availability is the main objective for the plasma physics community, but there are still many hurdles to overcome when it comes to understanding certain phenomena. A special concern involves the high confinement mode (H-mode), an improved confinement state of plasmas found in many tokamaks. Although this mode provided better conditions to achieve fusion with an increase in the density and temperature of the plasma, it also causes the emergence of instabilities called Edge Localised Modes (ELMs). These are events that can damage the plasma-facing components (PFCs), so exploring its cause may help control or mitigate them to make the best use of this H-mode. In this work the objective is to study a coherent mode that seems to be correlated with these ELM events using reflectometry and other diagnostics.

In this introductory chapter, an overview of nuclear fusion as an alternative energy source is given.

Chapter 2 provides experimental and theoretical background for the H-mode and the associated ELMs.

Chapter 3 explains the diagnostic tools of JET that were used in this work with an extended exposition on the principles of operation for microwave reflectometry, the main diagnostic used.

Chapter 4 presents the methods developed to analyse the data provided by the different diagnostic tools so to extract relevant information about the plasma behaviour.

In chapter 5 three discharges from JET are studied form the L-H transition up to the appearance of ELMs. The mode associated with ELMs is studied in detail, localised and correlated with plasma parameters.

Finally, chapter 6 gathers conclusions and shows possible future work.

Chapter 2

Background Research

2.1 L-mode and H-mode in tokamaks

The low confinement mode (L-mode) was the regime in which most reactors worked until another mode was discovered. During neutral beam heating experiments on ASDEX, under certain experimental conditions, there was a sudden transition to higher confinement. This high confinement regime is the H-mode. It is characterized by an abrupt reduction in heat and particle transport across the edge of the plasma. The improvement originates from the edge and propagates to the core plasma [10]. The increased confinement mitigates some technological obstacles and allows for the construction of smaller and cheaper devices. It is now the preferable regime of operation for fusion reactors worldwide, being responsible for the highest controlled fusion power that a reactor ever achieved of 16.1 MW in the Joint European Torus (JET). The future world's largest tokamak, International Thermonuclear Experimental Reactor (ITER), is projected to operate in this mode.

In order to attain this H-mode, experiments have shown that a minimum level of external heating is required, named threshold power, P_{LH}. External heating is usually supplied using methods such as Neutral Beam Injection (NBI) or Electron Cyclotron Resonance Heating (ECRH). The way the P_{LH} is projected for a new machine is derived from an empirical scaling law expressed in global plasma parameters. There is not a tested quantitative theory that accounts for all observations of the L-H transition [10]. The transition from L-mode to H-mode can be observed in figure 2.1. As the external power increases, at a certain P_{LH}, there is an abrupt increase in the plasma's kinetic energy. This moment signals the mode transition.

Other factors that ease the access to the H-mode are adequate edge conditions. Namely, low recycling regimes and a suitable magnetic geometry of the plasma. The plasma configuration that more easily achieves the H-mode is the divertor geometry, presented in figure 2.2. There are clear advantages when comparing this geometry to a simpler one, where a limiter controls the plasma-wall interaction. Although the divertor leads to a smaller plasma volume, compared to the limiter, it improves isolation of the plasma from the first wall and impurities. In the divertor configuration, the open field lines are directed to target plates that support high heat loads from the plasma.

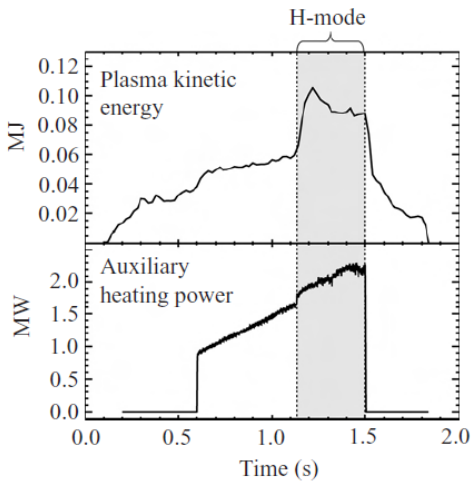

Figure 2.1: Experimental data showing the sudden transition from L to H-mode confinement when the power threshold is reached[6].

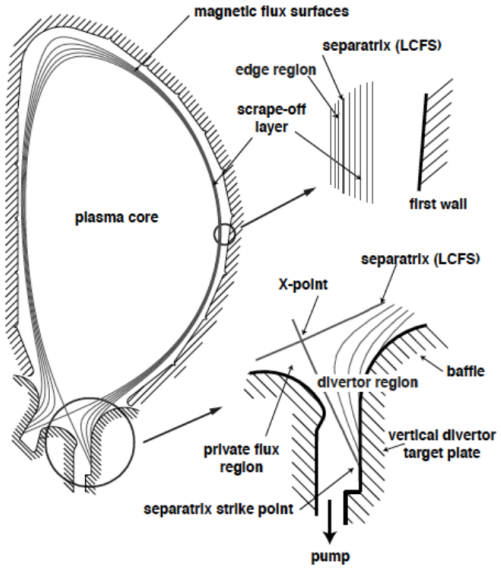

Figure 2.2: Divertor geometry in a tokamak[11].

As mentioned before, the improved confinement of the H-mode takes place at the edge of the plasma. After the L-H transition there is a reduction of fluctuations responsible for transport and an emergence of an Edge Transport Barrier (ETB). The barrier allows for steeper gradients of density and temperature that consequently cause a steeper pressure gradient. The ETB is noticeable when comparing the L-mode and H-mode pressure profiles along the normalised poloidal flux coordinate ρ_{pol} of figure 2.3a ($\rho_{\text{pol}} = \sqrt{\Psi_{\text{N}}}$ is a radial like coordinate in which Ψ_{N} is the normalised poloidal magnetic flux). When the edge pressure gradient steepens, the core pressure is overall increased. This happens with a mostly unchanged core pressure gradient, visible in figure 2.3b. The steep pressure gradient region of the ETB is commonly named pedestal.

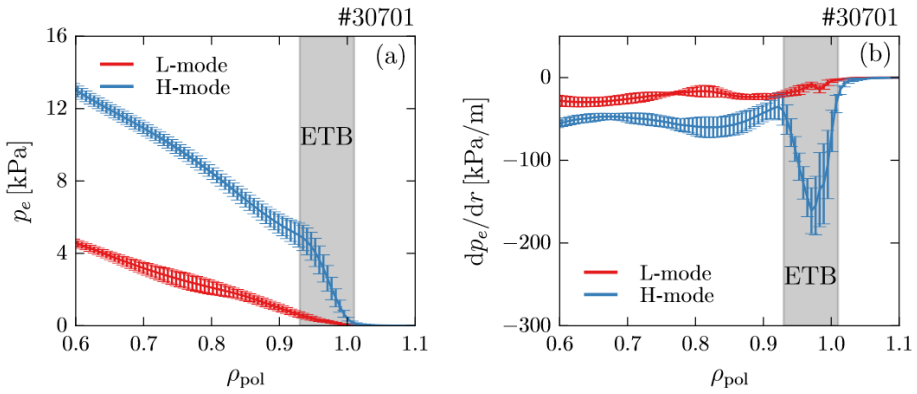

Figure 2.3: Electron pressure profile p_e(a) and its gradient $\frac{dp_e}{dr}$(b) in L-mode (red) and in H-mode (blue).[12]

Although the H-mode has clear advantages, some disadvantages come with this higher confinement. Specifically, the buildup of a steep edge pressure gradient, which can be unstable. Edge localized instabilities can be excited in the plasma, known as Edge Localized Modes. These limit the operation of

tokamaks and are still being explored by the fusion community.

2.2 ELMs - Edge Localized Modes

The appearance of ELMs in H-mode brought a new phenomenon to study. These events deteriorate periodically the pedestal and release high heat fluxes into PFCs. After each crash, the pedestal recovers, setting up the next ELM and completing an ELM cycle. ELMs are believed to result from large edge pressure and current gradients associated with H-mode operation.

These events are concerning in tokamaks for different reasons. Specifically, they limit energy confinement and they control the density and temperature in the outer zone of the plasma. They also produce the aforementioned large heat pulses on the divertor and first wall materials, that increase sputtering. All these effects on confinement, but particularly the heat loads on the divertor, make it rather important to understand how ELMs form. Understanding them will help develop techniques that mitigate or control them.

ELMs are mostly characterized experimentally since these are complex phenomena and no first principles theory describing them exists [13]. Four different ELM regimes are observed in experiments.

ELM-free operation is generally a transient behaviour leading to the large increase in edge density and impurities. The impurities in the plasma lead to a radiation collapse of edge density that contaminates core plasma. However, stationary ELM-free regimes are also being developed.

Type II ELMs are producers of moderate amplitude bursts, clearly separated in time. They equilibrate the averaged edge pressure at a reasonably high level so that the benefits of H-mode are present. This regime requires high plasma shaping and high density. These ELMs appear to be reactor relevant because of their reduced size.

Type III ELMs are described as "small" ELMs happening with very high frequency. These ELMs keep the averaged pressure at low levels, because of their constant outbursts of particles and energy. Reduced pressures translate to a substantial deterioration of confinement, making it a less favoured mode of operation even though it provides low divertor heat loads.

Type I ELMs are identified as "large" ELMs. These are shown in D_α radiation as big isolated bursts. Type-I and type-III are distinguishable based on the response of ELM frequency, f_{ELM}, to the heating power. While for the type-I ELMs, as the heating power rises, the f_{ELM} increases, for the type-III it decreases [14]. The type-I ELMs are of special interest, being the most common type in situations of high confinement, required for reactors. However, they are a particular threat because of the high release of energy and particles that puts the divertor under serious risk. It damages their material and requires replacement after a few of these outbursts.

2.2.1 Experimentally observed ELM Cycle

There have been previous studies that revealed different recovery time scales for n_e and T_e along the ELM cycle [15]. This allows for the ELM cycle categorization into different phases regarding these quantities at the top of their respective pedestal. The major phases of the ELM cycle are similar for all experiments [16]. There are 3 main phases:

Pre-ELM phase

This phase is characterized by the transport and edge plasma being near marginal stability and thus very close to becoming unstable. Both gradients of n_e and T_e, at the pedestal, are clamped [16]. How long this stays stable partially determines the length of the ELM cycle.

ELM crash phase

The non-linear interaction of modes causes the triggering of the ELM resulting in large losses of pedestal T_e and n_e, at the millisecond time scale. By the end of this phase there are high levels of transport. Nonetheless, before the phase ends, there is a recovery of the T_e and n_e.

Recovery phase

After the edge profiles of T_e and n_e are deteriorated, during this period they steepen up to their original pre-ELM shape. Studies in ASDEX Upgrade [16] allowed to separate this phase into several stages. These are illustrated in figure 2.4(in these stages, n_e and T_e are measured at the top of the pedestal).

(I) this stage is right after the ELM crash, it is characterized by an almost full recovery of n_e. A slow increase in T_e is noticeable with the particle transport over the separatrix decreasing.

(II) at this point, the T_e recovery accelerates and n_e reaches its maximum. The transport across the separatrix reaches its minimum, but by the end of this stage it starts to increase.

(III) the T_e recovery slows down again and the n_e somewhat decreases as the transport increases. By the end, the transport reduces slightly as it approaches stage (IV).

(IV) in this stage the decrease in transport causes a slight increase in n_e. The temperature slowly increases until its maximum. The transport finds its equilibrium value, which is much higher than the stage (II). At the end of this stage, it merges into the Pre-ELM phase with all its characteristics.

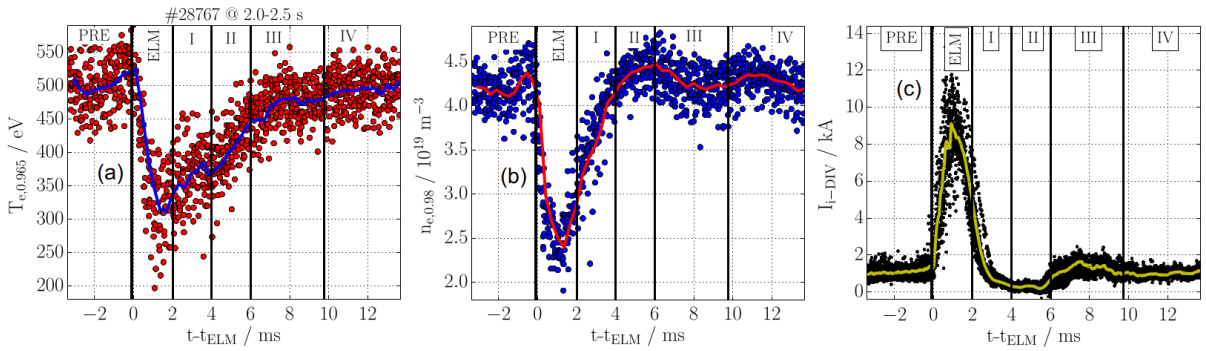

Figure 2.4: ELM synchronized data points and smoothed signal of (a) the electron temperature T_e and (b) density n_e at their pedestal top, (c) the inner divertor shunt current as a measure for the transport over the separatrix. [16]

2.3 Edge instabilities

To understand how ELMs develop it is necessary to study the various instabilities that can form at the plasma edge. The pedestal stability is also very important and usually correlated with the instabilities at the edge. Two important quantities are drivers of instabilities, the thermal pressure, p, and the current flowing in the plasma, j [16].

The most favored theory to describe the type-I ELM cycle is the Peeling-Ballooning theory [17].

2.3.1 Peeling Ballooning Modes (PBM)

Edge H-mode plasmas are characterized by strong pressure gradients, which are known to cause ballooning modes. Ballooning modes are instabilities that, owing to the particular distribution of the poloidal spectra of the fluctuations, yield a dominant amplitude at the low field side of the torus, in the region of unfavourable curvature. After a critical pressure gradient, α, is exceeded, this mode sets in and decreases the pressure gradient such that the edge is stable again. This allows for the buildup of pressure to happen again [17]. However, the pressure gradient alone is not responsible for ELMs. After the α is exceeded, the plasma stayed fairly stable for some time before an ELM occurred. Not only this but also the ballooning mode increased transport more than expected. So another component must help the triggering of the ELMs.

That is where the edge current density complements this theory, since, when high enough, results in peeling modes. Peeling modes cause kinking of a plasma tube [17].

These two factors are the central elements for this theory, that hypothesizes ELM events to follow this order:

1. After an ELM crash, the plasma is stable and the pressure gradient rises. The increase goes on until a critical α is achieved.

2. The plasma becomes unstable against localized ballooning modes, which generates enough transport to limit the pressure gradient. But, the bootstrap current still rises because of the reduction of collisionality in the edge (caused by the temperature increase there)[17].

3. This makes, at a certain point, the peeling mode unstable, which causes the ELM to occur.

2.3.2 Kinetic Ballooning Modes (KBMs)

The KBMs are thought to limit the edge pressure gradient, making them of interest to understand.

KBMs are the kinetic analogues of ideal ballooning modes [16]. They are pressure fluctuations parallel to magnetic field lines which are not considered in ideal MHD equations. Similar to ballooning modes, these appear above a critical β value. They propagate poloidally in the ion flow direction, because of the diamagnetic drift caused by $\nabla p \times B$.

2.3.3 EPED model

The EPED model is a predictive model for the pedestal height, p_{ped}, and width, Δ. It is based upon two constraints: the onset of non-local PB modes, at low to intermediate toroidal mode number, and of the KBMs, at high toroidal mode number. The constraints can be quantitatively predicted using sets of model equilibria. These allow direct comparisons of the model to current experiments and predict the performance of future experiments [18].

2.4 The Sawtooth Cycle

The sawtooth instability can be defined as a quasi-periodic relaxation of the tokamak core. It results in the hot plasma being ejected from the core, leading to a sudden drop of temperature and density around this region. These events are observed in both L- and H-mode of either large or small tokamaks [19].

The cycle of this instability can be experimentally characterized by three regimes shown in figure 2.5:

i) sawtooth ramp phase - it is a dormant period when density and temperature of the plasma core increase approximately linearly with time

ii) precursor phase - in this phase there is a growth of a helical magnetic perturbation. It is caused by the toroidal rotation of the plasma, and increases until the collapse phase [19]

iii) collapse phase - a brief interval in which the plasma's core density and temperature decrease abruptly

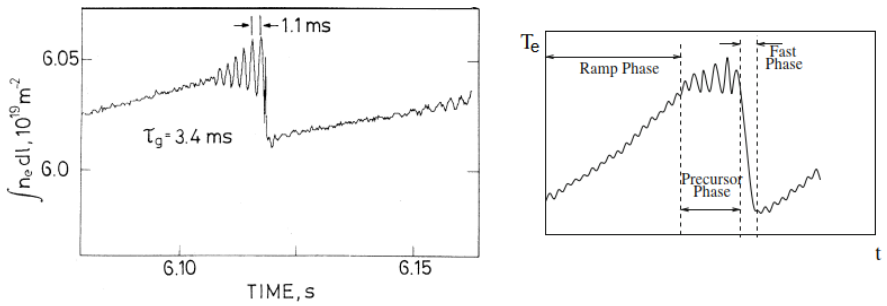

Figure 2.5: The line-integrated electron density of a JET plasma (left) and representative electron temperature (right) both exhibiting a sawtooth oscillation

Chapter 3

Experimental set-up and diagnostic tools

3.1 JET

JET is the largest operational magnetically confined plasma physics experiment. It is a tokamak device operated at the Culham Centre for Fusion Energy in Oxfordshire, UK. Used by over 40 European laboratories, it is the focal point of the European fusion research programme. This is because it is designed to study fusion in conditions similar to a power plant, being the only experiment that can operate a deuterium-tritium fuel mix [20]. Operating since 1983, JET has made major advances in fusion. It has increased confidence in the tokamak as a design for future fusion power plant. This device lead to the construction of the first commercial-scale fusion machine, ITER [20].

The discharges from which the data was obtained used the JET ITER-Like Wall (ILW) configuration. This tokamak configuration uses an inertial cooled full tungsten (W) divertor and beryllium (Be) main chamber first wall. Both components were installed in 2011 to substitute the carbon wall. This set-up provides an environment closer to ITER in order to verify physics models and modelling tools. While also allowing the study of how PFCs interact with the plasma [21].

Diagnosing plasmas involves the most advanced measurement techniques of physics and electronic engineering. There are over fifty different approaches applied at JET [22]. Some of these diagnostics used for this thesis are briefly explained.

3.2 Neutral Beam Injection (NBI)

Neutral beam injection is a method used to increase both the temperature and density of magnetically confined plasmas. It does so by injecting high energy neutral particles.

The process to increase the plasma temperature happens after the neutral particles, such as deuterium or tritium, are injected across the plasma. They travel through the magnetic and electric fields undisturbed until they start colliding with ions and electrons. These collisions make the neutrals ionised

and consequently magnetically confined. The newly formed ions still have high speeds that transfer to the plasma through Coulomb Collisions, increasing the overall plasma temperature [6].

The speed at which the neutrals are injected into the plasma must be optimized. A low energy beam, stores most of the energy at the outer layers of the plasma. An unnecessarily high energy beam goes through the plasma and stores its energy on the opposite wall [6]. Both situations are unfavorable for the well functioning of this heating system. Ideally, the speed is set to increase the core temperature.

3.3 Reflectometry

Measuring densities with high temporal and spatial precision is crucial for the study and operation of magnetically confined plasmas. Material probes are limited because they cannot support the high temperatures of fusion plasmas. So these can only be placed at regions of low density, the plasma edge. A viable option to track density evolution is the use of electromagnetic waves to probe the plasma. Most tokamaks apply this technique in diagnostics, such as multichannel interferometry and Thomson scattering. And although these have been very reliable in fusion research, they are two of the most demanding diagnostics for plasma accessibility. Microwave reflectometry presents itself as an alternative that has lower requirements for plasma accessibility. This diagnostic not only allows measurements of electron density profiles but also the detection of electron density fluctuations [23].

How it operates consists of launching a microwave radiation with a certain frequency, ω_0, into the plasma along the electron density gradient. The wave travels through the plasma and reflects at a layer where the electron density equals a critical value, n_c. It then goes back and is received at an antenna. The received wave is mixed with a reference beam to determine phase changes caused by propagation and reflection in the plasma [24]. How much the phase varies allows to infer the plasma density at the reflecting layer. There are two different polarization modes in which reflectometry can be operated [24]:

- the **O-mode**, that uses **ordinary waves** to probe the plasma. These waves are emitted with the electric field, E_1, parallel to the magnetic field of the plasma, B_0, so $E_1 \parallel B_0$. The wave can be sent with an angle, $\theta_\circ$, regarding the normal of the reflecting surface. The reflection occurs when the refractive index of the plasma, $N(\omega_0, x)$ given by equation 3.1 [25], is equal to 0.

$$N(\omega_0, x) = \sqrt{1 - \frac{\omega_{pe}^2}{\omega_0^2} - \sin^2\theta_\circ} \tag{3.1}$$

where ω_{pe}, shown in equation 3.2, is the plasma frequency and ω_0 is the probing frequency. Assuming the wave is emitted perpendicularly to the reflecting surface, $\theta_\circ = 0$, the wave will be reflected at $\omega_0 = \omega_{\mathrm{pe}}$.

$$\omega_{\mathrm{pe}} = \sqrt{\frac{n_{\mathrm{e}} e^2}{m_{\mathrm{e}} \epsilon_0}} \tag{3.2}$$

- the **X-mode** that uses **extraordinary waves**. These waves are polarized with the electric field perpendicular to the plasma's magnetic field, $E_1 \perp B_0$. Total reflection for these waves can be calculated from the $N(\omega_0, x)$ given by equation 3.3 [25].

$$N(\omega_0, x) = \sqrt{1 - \frac{\omega_{pe}^2}{\omega_0^2} \frac{\omega_0^2 - \omega_{pe}^2}{\omega_0^2 - \omega_{ce}^2} - \sin^2 \theta_\circ} \tag{3.3}$$

where ω_{ce} is the electron cyclotron frequency, given by $\omega_{\mathrm{ce}} = \frac{eB}{m_e}$. When $\theta_\circ = 0$, from the equation 3.3 being set to 0, the frequency at which the wave will be reflected can be calculated. For this mode there is an upper and lower cut-off frequencies for which the reflection occurs presented in equation 3.4.

$$\omega_{\mathrm{U,L}} = \sqrt{\frac{\omega_{\mathrm{ce}}^2}{4} + \omega_{\mathrm{pe}}^2} \pm \frac{\omega_{\mathrm{ce}}}{2} \tag{3.4}$$

As aforementioned, the information from which one can infer the plasma density is through the phase delay of the reflected wave. It is given by equation 3.5 [23]

$$\phi(\omega_0) = 2\frac{\omega_0}{c} \int_{x_0}^{x_c(\omega_0)} N(\omega_0, x) dx - \frac{\pi}{2} \tag{3.5}$$

where the limits of the integral, x_0 and x_c are the coordinates of the plasma boundary and the cut-off layer, respectively. The $\frac{\pi}{2}$ component is added because of the reflection in the plasma.

3.3.1 Profile Measurements

At the cut-off layer, the position and the electron density can be determined for both ordinary and extraordinary waves. To do so, we must know the phase delay in the received wave as well as the magnetic profile along the tokamak. If we send multiple frequencies into the plasma and gather the inferred positions and densities, we can calculate an electron density profile.

In many tokamaks, the n_e profile is obtained with the fast sweep reflectometry. In JET, this diagnostic was developed to measure density profiles from the plasma edge to mid radius. Depending on the plasma density and magnetic profile, it can measure up to the center. The set-up is very similar to ITER's projected reflectometer's accessibility. It is installed outside the JET torus hall, in a room away from any damaging neutron emission. The configuration for development of these profiles is of six reflectometers with different polarizations and frequency ranges, presented in table 3.1 [26]. They are integrated with the four correlation reflectometers into a system that allows these to share four waveguides. Three of them are used for microwave emission and one is used for reception [26]. This system allows the measurement of up to 100000 profiles at a minimum of 1 ms time resolution. We can vary the time resolution throughout the discharge by previously defining different sampling rates [26].

	Frequency band	Polarization
1	Q(33-51 GHz)	X-mode
2	V(49-76 GHz)	X-mode
3	W(74-111 GHz)	X-mode
4	D(109-150 GHz)	X-mode
5	V(49-76 GHz)	O-mode
6	W(74-111 GHz)	O-mode

Table 3.1: The reflectometers used for the determination of the n_e profile [26]

3.3.2 Fluctuations Measurements

Microwave reflectometry can also be used for the measurement of density fluctuations. To do so, a method where the antenna is tilted purposely by an angle $\theta_\circ$ is employed, named Doppler reflectometry or Doppler Backscattering (DBS). This angle acts as a band-pass filter in the $K_\perp$-space of perturbations that selects specific fluctuations of $K_\perp$. It also allows to determine the perpendicular velocity of the plasma [27]. The intensity of the returning signal also contains information about the amplitude of density fluctuations.

A reflectometer comprises a microwave source, transmission lines and a detection system. The Homodyne reflectometer, in figure 3.1, is the most simple configuration of a reflectometer. This system launches a wave, with constant amplitude and angular frequency ω_0, into the plasma. The wave is reflected at a critical density and scattered along the path until captured by an antenna. The received signal, $s_r(t) = A(t)cos[\omega_0 t + \phi(t)]$, in both $A(t)$ and $\phi(t)$ contain a stochastic component that carries information on the statistical properties of the density fluctuations of the reflected layer and travelled plasma. After being received, the $s_r(t)$ signal is then mixed with the original signal and a low-pass filter applied. Although this system is simple and cheap, it comes at a cost: the system has poor sensitivity; the mixer inputs an inherent 1/f noise; and the system loses the sign of $\Delta\omega$ [25].

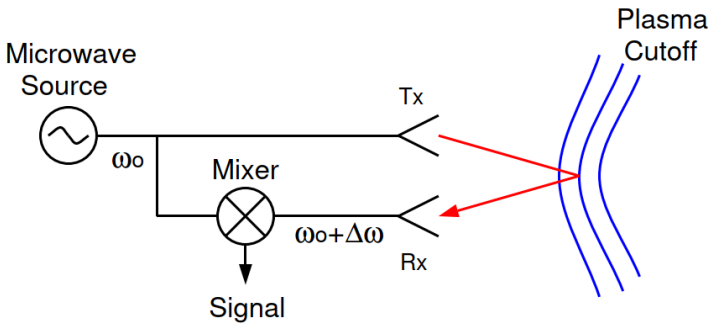

Figure 3.1: Circuit diagram of Homodyne Reflectometer [25]

An alternative, albeit more complex and more expensive, that fixes the loss of the signal of $\Delta\omega$, is the heterodyne system. This system, presented in figure 3.2, uses a local oscillator with a different frequency, ω_1, for down-shifting the frequency of the reference and received signals. The heterodyne system also has a Phase-Locked Loop (PLL) that helps remove frequency jitters and drifts that reduce the signal quality in the microwave source [25].

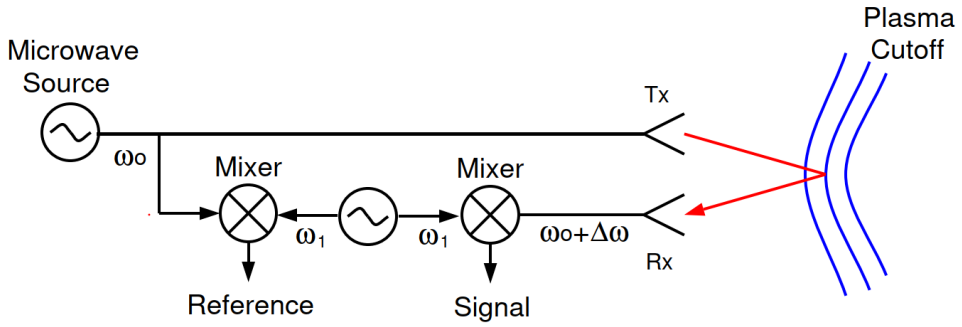

Figure 3.2: Circuit diagram of part of Heterodyne Reflectometer [25]

In order to separate the behaviour of the $A(t)$ and $\phi(t)$, quadrature detection is essential. To do so, the received and reference signals are provided to an IQ detector, as seen in figure 3.3.

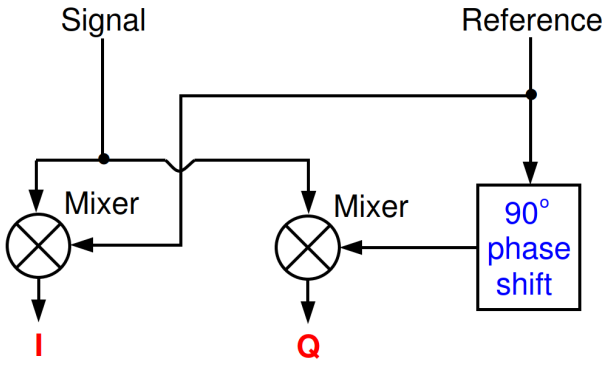

Figure 3.3: Circuit Diagram of IQ detector [25]

This circuit outputs an In-phase signal (I) by mixing the reference and received signals, and a Quadrature signal (Q) by shifting the reference signal by 90^{o} and mixing it with the received signal. The resulting signals are given by 3.6.

$$\begin{aligned} I &= A\cos(\phi) \\ Q &= A\sin(\phi) \end{aligned} \tag{3.6}$$

From these, it is possible to get individually both the phase, $\phi = arctan(Q/I)$, and the amplitude, $A = \sqrt{I^2 + Q^2}$.

Correlation Reflectometer System at JET

The JET correlation reflectometer (CR) used in this work contain two X-mode fast frequency hopping channels. These launch from the Low Field Side (LFS) mid-plane and are designed for normal incidence [28]. In the studied discharges, there is a deliberate vertical shift of the plasma column that causes both strike points, of the separatrix on the divertor region, to be positioned at the vertical targets (VT configuration). Such configuration is illustrated in figure 3.4. Its intent is to cause a small oblique angle between the incident beam and the cut-off magnetic surfaces. This way the diagnostic operates as Doppler

Reflectometry so we can study fluctuations in the plasma. The scattering wavenumber of the density fluctuations is determined via ray tracing as shown in figure 3.4.

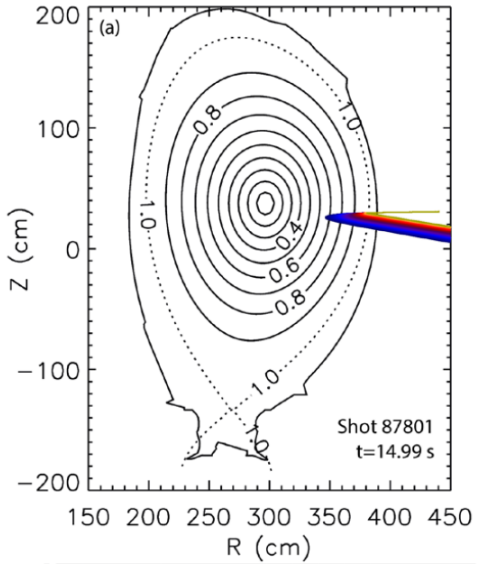

Figure 3.4: Doppler Backscattering ray tracing results for all the 165 probing frequencies (from 74.125 to 93.805 GHz) launched horizontally in a VT configuration [28]

Each channel can be pre-programmed to emit a specified launch frequency pattern, being repeated continuously throughout the discharge [28]. For the chosen discharges, it operates in the W-band(75–110 GHz) with a sampling rate of 2 MHz [29]. It records the in phase and quadrature phase of heterodyne signals, providing separate measurements of the amplitude and the phase. Most of this thesis' work was done using data from this diagnostic.

3.4 Additional Diagnostics

3.4.1 Electron Cyclotron Emission (ECE)

ECE is the emission of microwave radiation, with a certain frequency caused by the gyro motion of electrons. Gyro motion occurs when charged particles experience the Lorentz force because of the strong toroidal magnetic fields. The frequency of the radiation emitted by these electrons follows equation 3.7.

$$f = \frac{\omega}{2\pi} = l\frac{eB(R)}{2\pi m_e} \tag{3.7}$$

where l is the harmonic number. In tokamaks, the main toroidal magnetic field follows $B \propto \frac{1}{R}$, allowing a correspondence between the light received and its origin in the plasma.

This phenomenon is used as a diagnostic tool to get the temperature of electrons at different radii along the plasma. Radiometers receive various frequencies of microwave light from the plasma at different intensities. From the resultant spectrum, the temperature profile can be inferred under certain conditions. Namely, that the plasma is optically thick and that the energy distribution is close to thermal equilibrium. Under these circumstances we can assume the plasma's radiated Intensity follows the Black

Body radiation(I_{BB}), in equation 3.8 [16].

$$I_{\mathrm{BB}}(\omega) = \frac{\omega^2}{8\pi^3 c^3} k_{\mathrm{B}} T_{\mathrm{e}} \tag{3.8}$$

The Black Body assumption allows us to attribute to each frequency a certain temperature. Knowing the radius associated with each emitted frequency we can develop a temperature profile for different radii. This diagnostic tool is widely used but fails close to the pedestal. There, the plasma density is not high enough to be considered optically thick, so the black body assumption does not hold.

The data used in this work was obtained through a multi-channel (96 channels) radiometer that gives reliable temperature measurements with a sampling frequency of up to 5 kHz.

3.4.2 Magnetic Coils

Magnetic loops or coils can extract different properties of a plasma in a tokamak. They can measure the plasma current, the loop voltage, plasma position and shape, stored plasma energy and current distribution [24].

The plasma stored energy is a good indicator of the performance of the plasma. It is calculated using data from a flux loop and Rogowski coils, shown in figure 3.5. The flux loop provides the evolution of the toroidal flux, while the Rogowski coils measure the current of the plasma. Knowing these quantities, it is possible to calculate the plasma's stored energy.

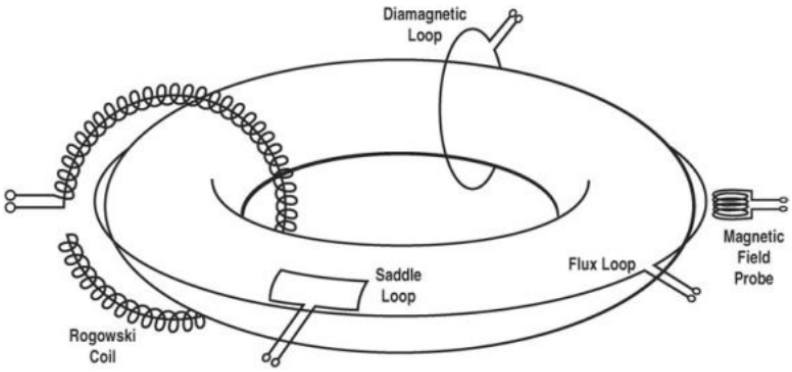

Figure 3.5: Different types of magnetic coils for plasma probing

For this work, the most important information magnetic diagnostics provide is about plasma instabilities.

The functioning principle for a magnetic coil is the Faraday's law, presented in equation 3.9.

$$\mathcal{E} = -N\frac{\mathrm{d}\Phi_B}{\mathrm{d}t} = -N\frac{\mathrm{d}(\vec{B}\cdot\vec{A})}{\mathrm{d}t} \tag{3.9}$$

Whenever there is a varying magnetic field in a wire loop with area $\vec{A}$, a voltage $\mathcal{E}$ emerges. Detecting this voltage in a coil reveals fluctuations of magnetic nature. Depending on how these are mounted they can measure toroidal, poloidal or radial magnetic flux fluctuations. Although magnetic coils are versatile and low cost, alone, they provide limited information on the localization of the fluctuations. Using a coil

only, one can not distinguish between a fluctuation that is smaller and closer to it, and a high amplitude fluctuation more centralized in the plasma.

The JET fast magnetic coils used to describe the magnetic fluctuations observed are displayed in figure 3.6. The coils used were the I803, P802 and P803 that have a sampling frequency of 1 MHz and T001 with 2 MHz. All the coils are on the LFS, the outside half of the torus more separated form the center solenoid, except for I803 that is positioned in the High Field Side (HFS), the inside torus half closest to the center solenoid.

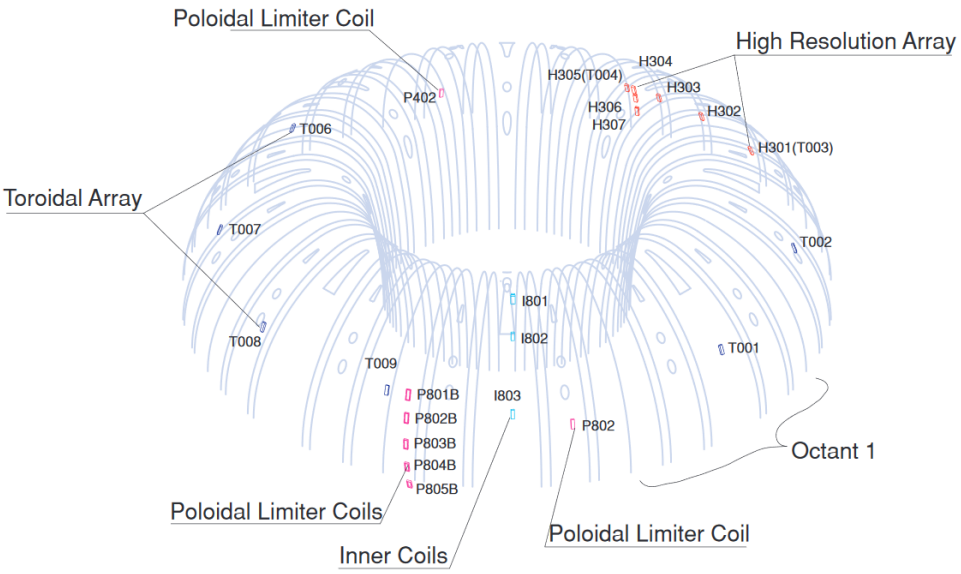

Figure 3.6: JET layout of Fast magnetic coils [30].

3.4.3 D_α radiation

D_α radiation is emitted by an excited deuterium after a $n = 3 \rightarrow n = 2$ electron transition. It is usually measured using photomultipliers mounted at different points of a tokamak. These have filters to only allow the detection of the D_α spectral line. Photomultipliers positioned near the divertor region allow the detection of ELMs and help identify transitions between confinement modes. In this work D_α radiation was sampled at a frequency of 10 kHz.

3.4.4 Be II radiation

The Be II radiation arises from ELM events. They cause the Beryllium walls of the JET tokamak to receive an enormous amount of energy. Such energy is received as particles lost from the plasma that impact the wall and cause the sputtering of Beryllium particles. These particles are ionized and subsequently neutralized, resulting in the emission of radiation. Spectrometers detect this radiation that helps show ELM events. Similar to the D_α signal, the sampling frequency was 10 kHz.

3.4.5 Interferometry

Laser interferometry measures the line integrated density along a line of sight, named chord, through the plasma. It sends the same electromagnetic wave through both plasma and vacuum. Then, these two waves are compared to determine a phase shift. The phase shift is caused by the refractive index difference between plasma and vacuum. When the wave is sent in O-mode the phase shift is given by equation 3.10

$$\varphi = \lambda_0 r_e \int_0^L n_e(x) \mathrm{d}x \tag{3.10}$$

where L is the distance through the chord in the plasma, r_e is the classical electron radius, λ_0 is the wavelength of the wave and $n_e(x)$ is the varying electron density along the used chord.

At JET, interferometry is applied using the far infrared (FIR) diagnostic. It initially used deuterated cyanide (DCN) lasers, operating at a wavelength of 195 μm. Later, it was upgraded by incorporating a CO_2 laser optically pumping two FIR methanol cavities that emit at 118.8 μm. It provides electron line-averaged densities every 15 ms along the lines of sight of presented in figure 3.7.

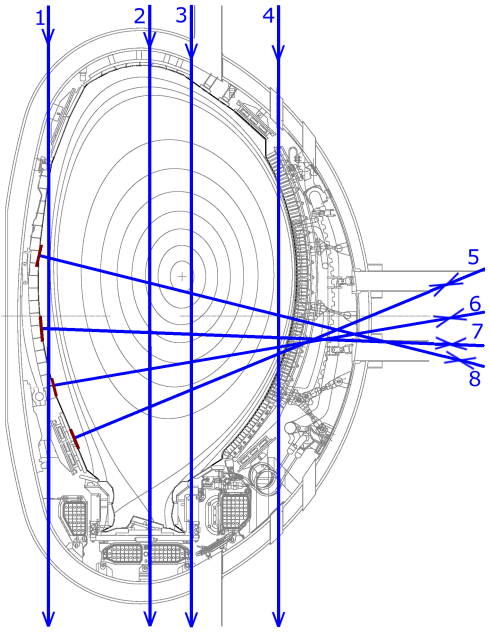

Figure 3.7: Chords configuration for the FIR diagnostic at JET

Chapter 4

Methods of data analysis

This chapter describes the tools developed to more easily analyse the experimental data provided by the diagnostics. Firstly, it was important to develop methods to identify events such as ELMs and sawteeth. Some of the data of electron density profiles, from the fast sweep reflectometry, had to be further processed before being used in the data analysis. However, the core analyses revolves around the doppler reflectometry data. It was processed to facilitate the identification of coherent modes from the background caused by turbulence. Algorithms for mode characterization and visualization were also developed.

4.1 ELM and Sawtooth detection

ELMs are important instabilities that need to be monitored so we can correlate them with the evolution of instabilities. In order to track these events, an algorithm was developed to signalize their start by analyzing the Be II signal. The blue line in figure 4.1 shows how this quantity reacts to these disruptive events. The signal is quite noisy, making it harder for peak detection. To circumvent this problem, the data is smoothed by applying a Savitzky–Golay (savgol) filter, resulting in the orange line overlaid in the Be II signal. The number of points and the interpolation degree used by this savgol filter is presented in table 4.1. Using a peak finder algorithm in this new filtered signal allowed to clearly identify the maximum of the ELM event (red points). The minimum amplitude for peak detection, $A_{threshold}$, was set for each discharge according to table 4.1. For this work the identification of the beginning of ELM events is more important as we are interested on its triggering mechanism. It was possible to get the ELMs start by calculating the difference between a Be II signal shifted by t_{step} and the original signal. The t_{step} is set so **Be II [t+t_{step}]-Be II [t]** is maximized at the beginning of most ELMs, the average rising time of the ELMs satisfied this condition. Visually inspecting the studied discharges, the average time length of an ELM is around 4-6 ms, if we set the rising time as half of that, the average rising time is around $t_{step} = 2.5$ ms. Since each point is separated by 0.1 ms, it is equivalent to comparing points separated by $N_{step} = 25$. Resulting in the **Be II [N+N_{step}]-Be II [N]** represented by the green line of figure 4.1. From this modified signal, the maxima were identified (black points) and from these the ones

closest to each ELM peak were selected as an ELM onset (green points).

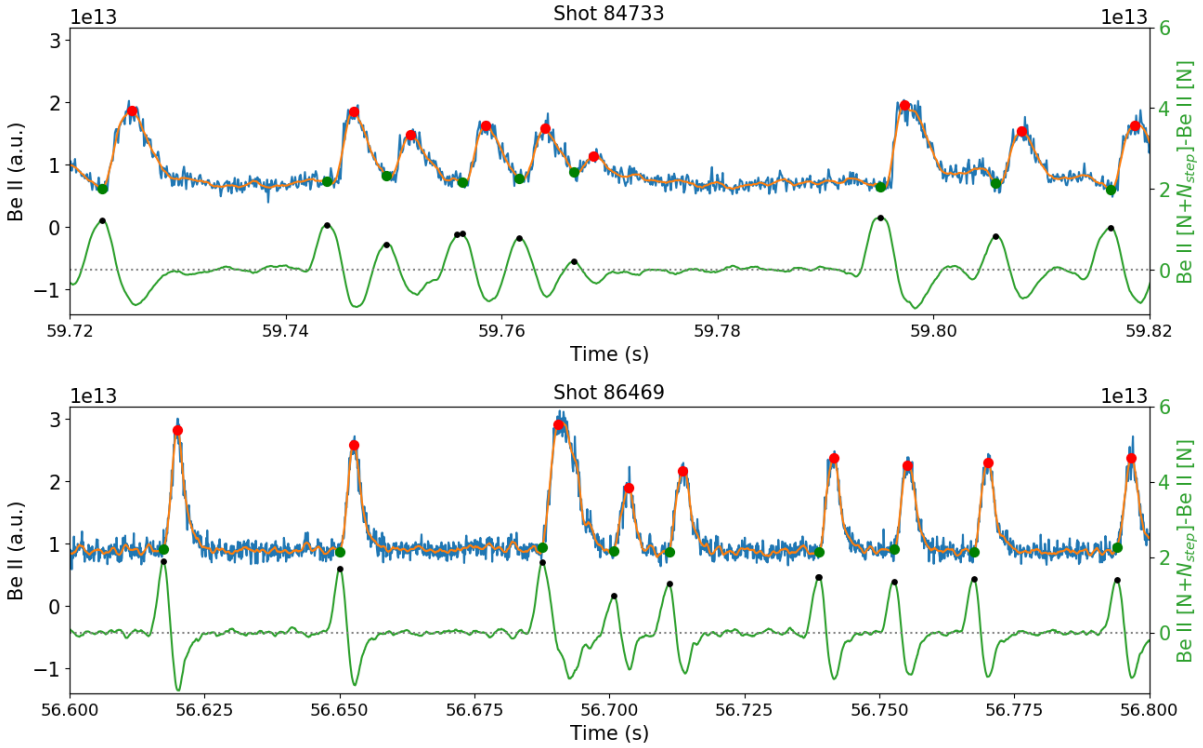

Figure 4.1: Results form ELM detection algorithm. Be II signal is plotted (blue line) as well as the smoothed signal (orange line). The ELMs peaks (red points) and onsets (green points) are signaled together with the auxiliary quantity **Be II** [**N**+N_{step}]-**Be II** [**N**].

# Shot	$A_{threshold}$ (10^{13} a.u.)	t_{step} (ms)	# points Savgol	Savgol interpolation degree
84733	1.10	2.5	35	4
86469	1.40			
86470	1.23			

Table 4.1: Parameters used for the detection of ELM start

Sawteeth were noticeable influencers of the intensity of the modes studied here making it important to track them. From the quantities used to check the plasma evolution, the temperature at the core is the best indicator of the sawtooth evolution. Visible in the figure 4.2, in blue, is the typical temporal evolution of the temperature at the core with significant falls signalizing sawtooth events. Identification of these drops was done calculating a difference between temperatures separated by 3 consecutive data points, T_e [**N**]-T_e [**N+3**], this number of points was the optimized difference in order to identify these events accurately. The result of this calculation is visible in the green line, which has identifiable peaks whenever a signal drop happens. The peaks, sign of sawteeth, were identified and are shown with red dots.

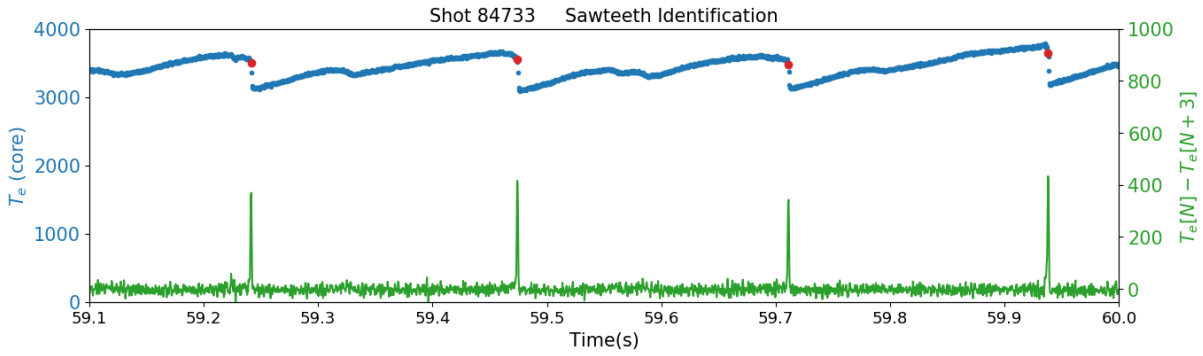

Figure 4.2: Example of detected Sawteeth (red points) in the plasma core T_e (blue points).

4.2 Correction of electron density profiles

The fast sweep reflectometry system provides profiles of electron density and the correspondent probing frequencies. The diagnostic has been designed to have a repetition interval as low as 15 μs but also to monitor density profiles for the whole discharge with a 1 ms time resolution. In this thesis, the electron density radial profiles were developed using intervals of up to 1 s along the discharge, that were used to localize the Doppler reflectometry measurements. First, the profile closest in time to the CR data is determined, for example the one presented in figure 4.3, where we have plotted one electron density profile and the probing frequencies used to obtain that profile in the edge plasma.

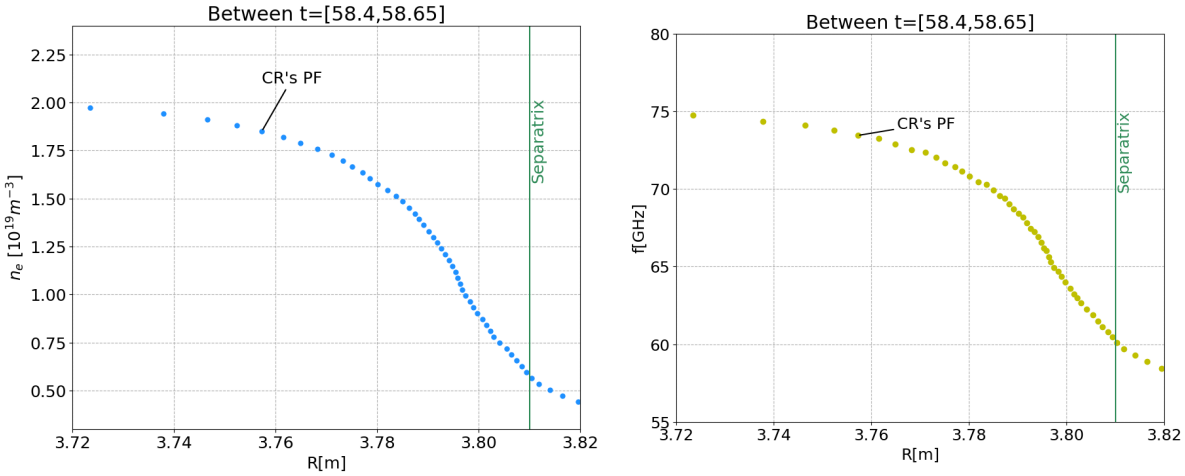

(a) Electron density profile

(b) Probing frequencies used for the density profile

Figure 4.3: Electron density and probing frequency profile for #84733 in the interval t=[58.4,58.65] s

From the probing frequency profile, figure 4.3b, we search for the frequency of the fast sweep reflectometer closest to the CR frequency, then the radius of that probing frequency is defined as the layer at which the CR is measuring. Density profiles measured by reflectometry are highly dynamic having often fluctuations that may not be relevant for our analysis. Therefore averaged density profiles of roughly stationary periods are done. These averaged profiles show often a clear radial shift between them as the steep gradient region is not aligned. A method to align these profiles was developed based on the identification of the inflection point. All the profiles were shifted so the inflection points were aligned with

the one from a representative density profile of JET. The calculation of the point of inflection required several steps. Profiles are not smooth as can be seen in the electron density profile of figure 4.4. Maybe this occurs because of fluctuations in the plasma affecting the measurement. To ease the detection of the inflection point, profiles were smoothed by a savgol filter. However, this method requires equally spaced points to work, which is not the case of the experimental density profiles. To fix it, we did an interpolation of the data followed by extraction of equally spaced points in radius. Using these points, a savgol filter is applied and the derivative calculated. The filtered data is shown by the orange line of the electron density profile of figure 4.4, with the derivative on the right. The most negative point visible in the derivative marks the inflection point, which is signaled in both plots by the vertical yellow line. Understanding how the gradient at the point of inflection varied along the discharge was of interest to understand the density profile evolution along the discharges. In order to have a robust estimate of this gradient it was estimated by doing a linear fit that used points in an interval of 2.5 mm to bigger and smaller radii of the inflection point, which are signaled in this figure by the blue vertical lines. This way the gradient at the inflection point was less sensible to randomly shifted points in the density profile that would overestimate or underestimate this gradient, if calculated like the derivative using only two points.

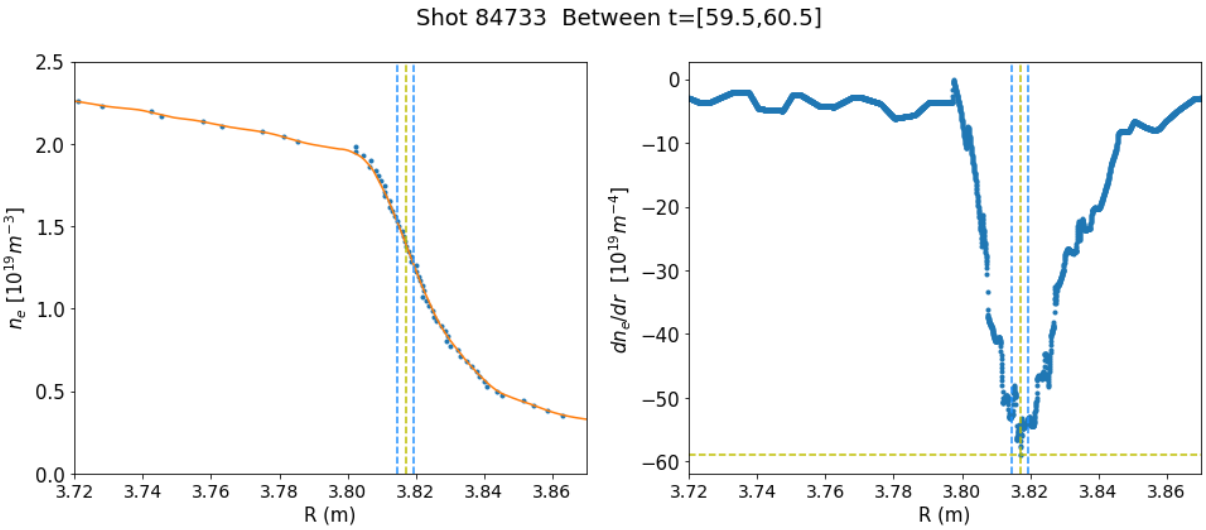

Figure 4.4: Electron density profile of interval t=[59.5,60.5] s with savgol filter (left) and the derivative of the density profile used to determine the inflection point (right), signaled by the vertical yellow dashed line.

Using the inflection points obtained through this method, a shift is performed to all the density profiles. The result of this shift is shown for some representative density profiles in figure 4.5. The profiles are taken along the discharge 84733.

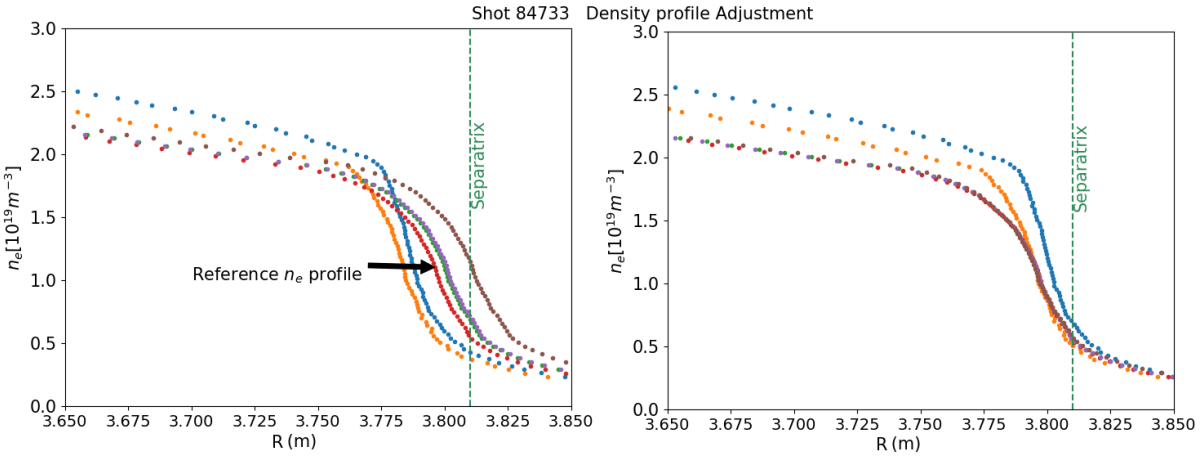

Figure 4.5: Electron density profiles before (left) and after (right) the radial shift adjustment. It is shown the reference profile used for the shifts.

4.3 Study of density fluctuations from the reflectometry signal

The main aim of this work is to investigate coherent modes using refletometry data. As mentioned in the previous chapter, the I.Q. signals provided by this diagnostic store valuable information on density fluctuations, in both the amplitude, A, and the phase, ϕ, of these signals. A way to combine the information they provide is to define a complex signal $Ae^{j\phi}$, which is equivalent to $Ae^{j\phi} = I + jQ$, considering equation 3.6. For conventional reflectometry (perpendicular incidence) most information on the density fluctuations is contained in the phase, while in Doppler mode this is obtained from the complex amplitude signal.

An essential tool to track the evolution of coherent fluctuations is the spectrogram of the I+jQ signal. This process consists of dividing a signal into equally numbered segments of data and applying a Discrete Fourier Transform (DFT) to each segment. The division of the data in this process means that the signal gets cutoff at the boundaries, which results in the appearance of fake frequency components (spectral leakage) in the estimated Power Spectral Density (PSD). The spectral leakage can be reduced by applying a window function to the points of each segment. This process weakens the intensity of the points at the boundary so they affect less the DFT. After each segment has a corresponding PSD, these are ordered in time and a spectrogram is obtained like the one illustrated in figure 4.6, of one of the discharges. In this work the study of fluctuations in the H-mode is the main concern, which is achieved for this discharge at t=57.2 s. In H-mode, there is often no noticeable Doppler shifted component in the fluctuations spectra resulting in a roughly symmetric spectrum in frequency. This makes it unnecessary to track modes in both positive and negative frequencies. So, for this work, only the positive frequencies of the spectrogram are considered and analysed.

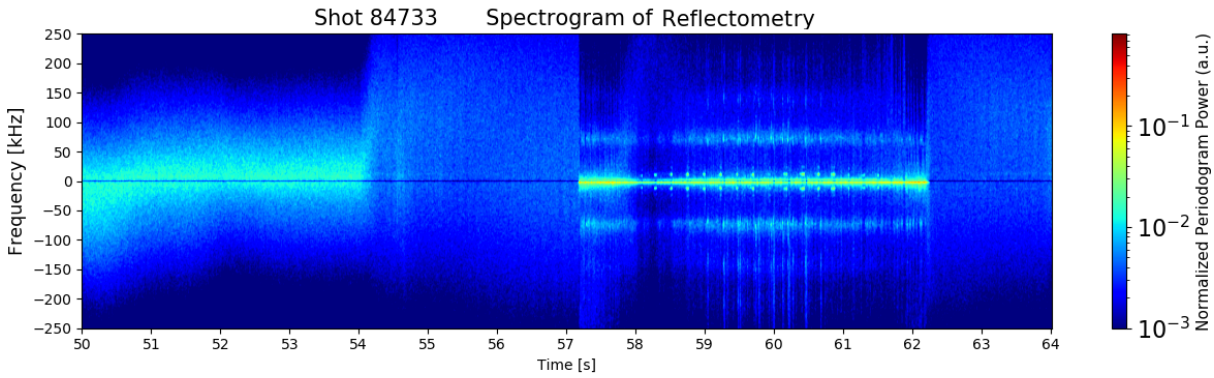

Figure 4.6: Spectrogram of signal I+jQ from discharge 84733

4.3.1 Modified Welch method

Although relevant information can be extracted from a normal spectrogram, there is a way to improve the amplitude estimation of each spectral component by using the Welch method. This method takes each segment from a normal spectrogram and subdivides it into many overlapping smaller segments. After applying a window function, it calculates the DFT for each smaller segment, then with the resulting PSDs an average is done with them. The resulting power spectrum is built with reduced uncertainty compared to a normal PSD. The Welch method causes a variance reduction proportional to the number of intervals that the original segment is divided into. However, reducing the length of each segment causes the frequency resolution to decrease. So a trade-off between variance reduction and frequency resolution arises.

For the analysis of the fluctuations done, a modified Welch method was developed to improve time resolution. This is achieved with a normal Welch method, using a Hanning window function and 50 % overlap of points with a slight modification in order to have better time resolution. The modification was the implementation of 50 % overlap of points between consecutive PSDs. The mean value of the signal segment is removed before each PSD is calculated since this offset results in a large spectral component at zero frequency. Along the discharges with varying probing frequency, the amplitude of the signal often varies significantly between probing frequencies because of the potency used for the emitted wave. In order to facilitate the analysis and the comparison of the mode behaviour, a normalization of the PSD is done. We did so by normalizing each probing frequency's PSDs with a corresponding total power, which was defined at the beginning of each discharge when the plasma is operating in the L-mode. This permitted the visualization of coherent modes in probing frequencies where the signal amplitude is reduced.

4.3.2 Determination of the mode amplitude and width

The correct determination of the coherent modes amplitude is crucial in this thesis. Initially, it was set as the integrated power of the PSD over specific frequency ranges. However, this is problematic because of the nature of the PSDs observed along the discharges. It was noticeable that the PSD had often a background component with an amplitude decaying with frequency typically as of $1/f^2$. The variability of the background made this defined intensity a poor indicator of mode amplitude. So, we implemented

a way to subtract this baseline component. Since the mentioned baseline varies in height and form, the aim was to fit a somewhat versatile function. The chosen function was the equation 4.1.

$$y(f) = \frac{a}{(f-c)^2} + b + df \tag{4.1}$$

where y is the power spectrum and f is the frequency. The constants a, b, c and d are free parameters to be fitted.

When trying to fit the PSDs, the existence of modes made it difficult to fit the data since they would induce in error and the baseline was overestimated. The calculation of the baseline had to be done ignoring frequency ranges where the modes existed. To do so, the PSDs were visually analyzed and these frequency ranges determined. The algorithm to get an adequate baseline from the PSD was:

1. Apply a savgol filter that would smoothen the noisy data.
2. Exclusion of points in the frequency ranges of modes, so these do not interfere with baseline detection.
3. Interpolation of the data in order to connect the points missing that were excluded from the modes' frequency ranges and ease the fit.
4. Use points from the interpolated function to fit equation 4.1.
5. Use the points that are below the fitted function to fit once again to equation 4.1, so the baseline is more accurate.

The second fit was done to make sure that the baseline is not overestimated, because after a general analysis of the first fit, it was generally above the visually identifiable baseline. After implementing the second fit, we identified an adequate baseline for most of the PSDs. An example of the application of the method is presented in figure 4.7a. The first fit is determined utilizing the smoothed data outside the green and red vertical lines. These lines marked the frequency ranges where modes usually appeared, and which data was ignored. The resulting first fit is displayed in red. The second fit, using only the points below the red fit, is displayed in green and is used as a baseline. The execution of the second fit required some constraints on the fitting parameters because of the scarcity of points that lead to some incorrect fits. Two conditions were imposed. If the parameter a was less than 0 and/or the parameter c was bigger than 0, then, the second fit would be ignored and the first fit was reused as baseline.

Having the baseline calculated, it was removed from the PSDs as shown in figure 4.7b, and only the points above the baseline were considered. The modified PSD facilitated and supported the mode detection and characterization. This was done by initially setting frequency ranges for the study of modes. These allow to track one mode within each interval. Based on the typical PSD components, we defined them as seen in figure 4.7b, in a range of 5-50 kHz, 50-100 kHz, 100-150 kHz and above 150 kHz. In each interval we carried out a peak finding algorithm resulting in the points marked in black. Determination of the mode's base is done by checking when the PSD is equal to zero. This is done for both higher and lower frequencies of the identified peak. These points are signaled in red and set the width of the mode. Using this data, it was possible to define three fundamental characteristics that outline mode behaviour:

- The width of the mode, that defines how wide in frequency it is.
- The frequency weighted by the PSD, defines the mean frequency of the mode. It is calculated through averaging the frequency weighted by the PSD, along the width of the mode.
- The intensity of the mode, that defines its strength, is the integrated power along the width of the mode.

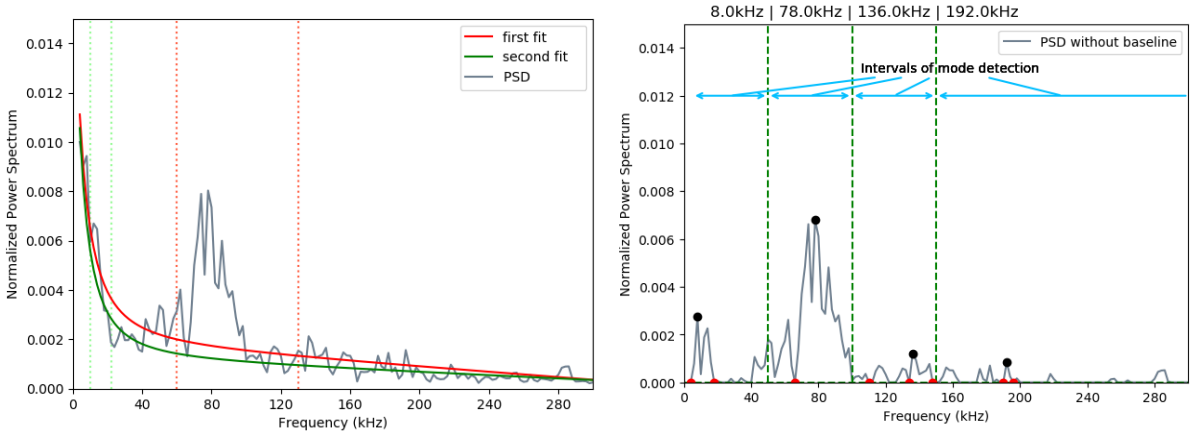

(a) Baseline detection

(b) Power spectrum without baseline and mode detection

Figure 4.7: Detection and subtraction of baseline as well as mode detection in frequency ranges.

4.3.3 Display of the mode evolution

The two quantities described above were estimated along the discharge so modes could be tracked. Plasma quantities were displayed alongside to relate them to characteristics of the mode. An example of this analysis is displayed in figure 4.8. In plot a), indicators of ELMs are presented (D_α and Be II signals). In all plots the beginning of ELMs are signalised by vertical green lines. In plot b), the temperature at the top of the pedestal and the edge line-averaged density are shown, in blue and red respectively. The line-averaged density is obtained from interferometry and divided by the length of the chord, which is why the units are in m^{-3}. In the plots c), d) and e), the mode identified in each frequency range is plotted. The width of the mode is also displayed by a vertical line. Different frequency ranges have a certain color to identify their mode. However, for every instant, the most intense mode from the frequency ranges is marked in orange. Note that due to the background fluctuations in the spectrum, even after removing the baseline there is a minimum detectable mode amplitude (horizontal green line in figure 4.8). The minimum intensity for a mode to be detected and plotted has the horizontal green line was set at $Int_{min} = 30$ and was determined by looking at the power spectra for all discharges. The intensity along time for each frequency range is marked by the magenta points, if the point is below Int_{min}, then the frequency and the width of the mode are not plotted. We attributed different symbols to the mode frequency to convey more information about it. Specifically, if the mode width is shared or not with other modes:

- $\triangle$ - the mode width is shared with the higher frequency range, the mode plotted above

- $\bigtriangledown$ - the mode width is shared with the lower frequency range, the mode plotted below
- $\Diamond$ - the mode is so wide that shares the base with the higher and lower frequency ranges
- $\circ$ - the mode width is not shared with other modes

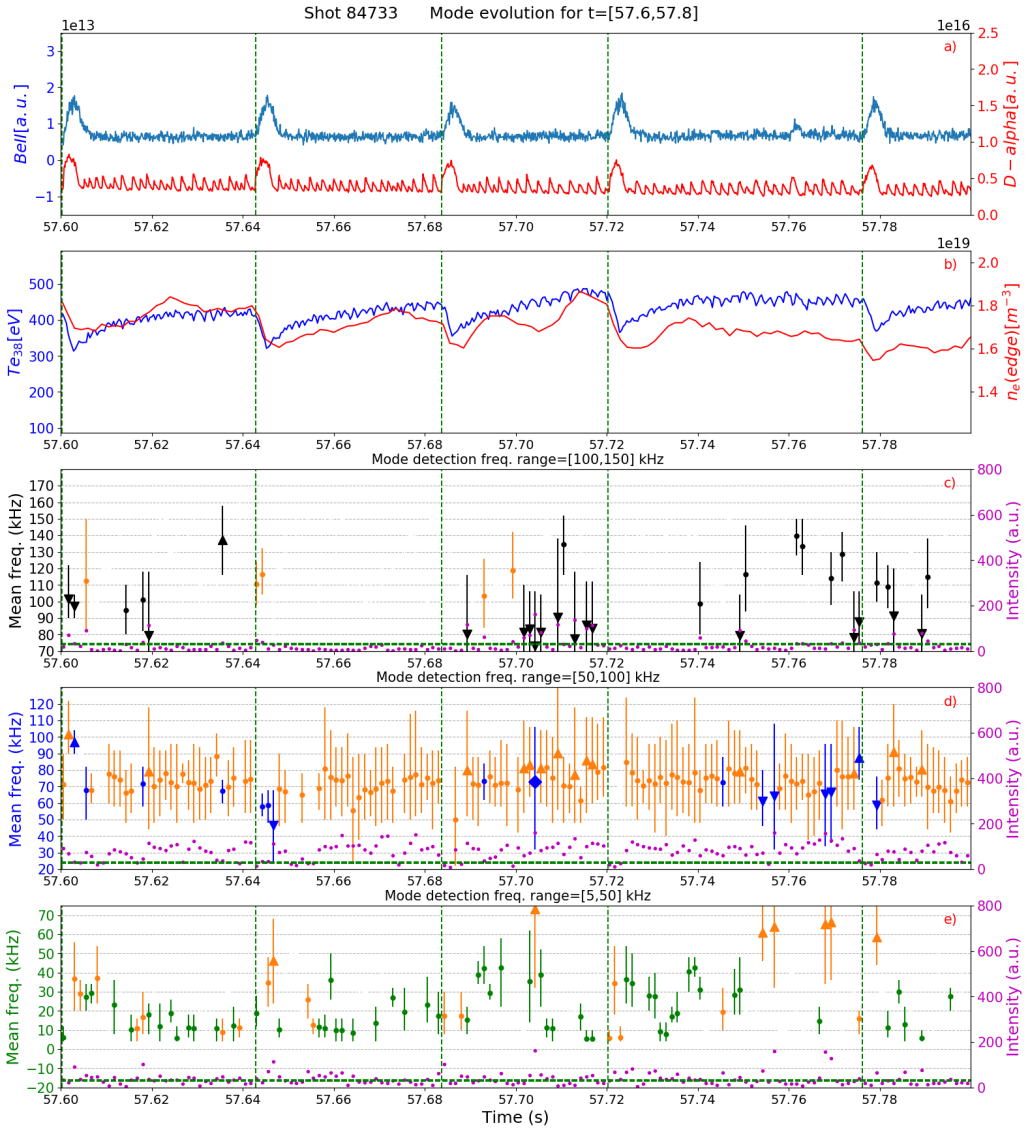

Figure 4.8: Mode evolution in between ELMs. a) Be II and D_α signals, b) Te_{38} and n_e(edge) and frequency of the modes and their intensity (in magenta) identified in different ranges: c) 100-150 kHz; d) 50-100 kHz; e) 5-50 kHz, the green horizontal lines are the $Intensity_{min}$ that indicate if the mode is present.

Chapter 5

Experimental Results

Several L-H threshold experiments were performed on JET to investigate the dependencies of the P_{LH} [31], [32]. Three representative discharges are analysed here with heating provided by NBI. The discharge 84733, with a toroidal field $B_t = 2.4$ T and plasma current $I_p = 2$ MA, was used primarily to characterise the evolution of a mode associated with ELMs and relate that evolution with plasma parameters. The other two, the #86469 and #86470, with higher $B_t = 3$ T and $I_p = 2.5$ MA, had the additional aim of trying to localise this mode.

In this chapter, a brief description is given of the discharges and data used to characterise them. Followed by a more in-depth description and selection of plasma parameters from which we can extract more information. Information which is then compared to the results from the study of the specific mode, visible in the reflectometry's signal in the H-mode phase of the discharges. This mode is the main focus of this thesis and its evolution is analysed at different radii of the plasma and finally a radial profile for this mode is determined.

5.1 Evolution of the plasma parameters

5.1.1 Temporal evolution along the discharge

Discharge 84733

The main parameters needed to study a discharge are illustrated in figure 5.1. In plot a), a spectrogram of the Doppler Reflectometry signal is presented. It was estimated to have a resolution of 0.25 ms using successive DFTs of 0.5 ms of data with 50 % overlap of points. To each segment, a Hanning window function was applied before each DFT. In plot b) we have the plasma stored energy, W_p, (in blue) and the heating power, P_{NBI}, (in red). ELM identification is done with the help of signals Be II (in blue) and D_α (in red) plotted in c). The D_α helps signalise the confinement mode of the plasma, as well as identify important small oscillations that affect the coherent mode. In order to keep track of these oscillations, the spectrogram of the D_α is displayed in plot d). It was built like the spectrogram of reflectometry but with larger windows of 50 ms because of the reduced sampling frequency of this quantity. The temperatures from the ECE are also plotted for different regions of the plasma in e), with the respective

locations shown in the legend. The locations of the temperatures do not vary significantly over time, so an average over the whole discharge is performed for each channel. All the temperatures T_{xx} have a subscript corresponding to one of the 96 channels of the ECE system (mentioned in chapter 3). The interferometry system provided the line-averaged densities plotted in f). These are of the core (in blue) and the edge (in red) plasma and correspond to chords 3 and 4 of figure 3.7. Finally in plot g), the spectrogram of a LFS magnetic coil (T001) is shown, estimated similarly to the spectrogram of Doppler Reflectometry.

An overall description of this discharge starts at the L-H transition, illustrated in figure 5.1, at t=57.2 s. Its trigger seems to be related with the increase in the P_{NBI}. The transition is characterised by an immediate fast decrease of D_α radiation and later by the emergence of ELMs. Also noticeable is the increase of plasma parameters like density, electron temperature and plasma stored energy. In the D_α spectrogram, the appearance of oscillations at low frequency clearly mark the transition. After the H-mode is achieved the plasma stored energy follows the increase in the heating power, reaching a maximum around t=60.3 s and decreasing until the transition back to the L-mode.

In this discharge ELMs are most likely type-III and appear in two periods. First near the L-H transition with small distinguishable outbursts. Then, from t=58.6 s until the back transition with ELMs one after another at high frequency. The ELM frequency in this latter period decreased with increased plasma power, which is characteristic of type-III ELMs [14].

The evolution of the plasma parameters is affected not only by ELM events but also by sawteeth. They are clearly identifiable through the abrupt periodic decreases of the electron temperature and line-averaged density most close to the core, Te_{88} and $n_e(core)$. We estimated the frequency of these sawtooth events based on the drops in Te_{88} between t=[57.2,62.5] s, resulting in a $f_{sawtooth} = 4.6 \pm 0.6$ Hz.

In the spectrogram of reflectometry, a coherent mode around 70-90 kHz is visible with varying intensity and affected by ELM events. The following sections will explore it in deeper detail.

In figure 5.2 are plotted in deeper detail the evolution of the edge density, as well as blue horizontal arrows that represent the intervals used by the fast sweep reflectometry to develop density profiles. These were taken along the discharge and were used to locate the probing frequencies of the correlation reflectometer. Each interval signals in the y axis a corresponding density gradient calculated at the point of inflection, as explained in chapter 4. The density gradients, from the many density profiles presented in figure 5.2, show a tendency of following the evolution of the edge density. This is expected since they are deeply correlated, if the density profile is steep, and the density gradient is high, so is the line-averaged edge density since the interferometer is probing the edge plasma that covers the steep gradient region. Despite most of the density profiles following the edge density tendency, there are some whose value seems to be overestimated like the ones at t=[59.4,59.7] s; [60.3,60.5] s; [61.7,62.0] s. What happens in these density profiles, shown in figure 5.3, is that they are taken in small periods while ELMs are occurring, which causes the density profile to drop momentarily and induce in error when building the averaged density profile for that period. The result is that the points are shifted randomly by a small distance from where they are supposed to be, reducing the fidelity of the density profile and causing the density gradient at the inflection point to be overestimated. When there are a lot of ELMs it is better to use

longer periods to average the density profile so these shifts are averaged out and become less noticeable.

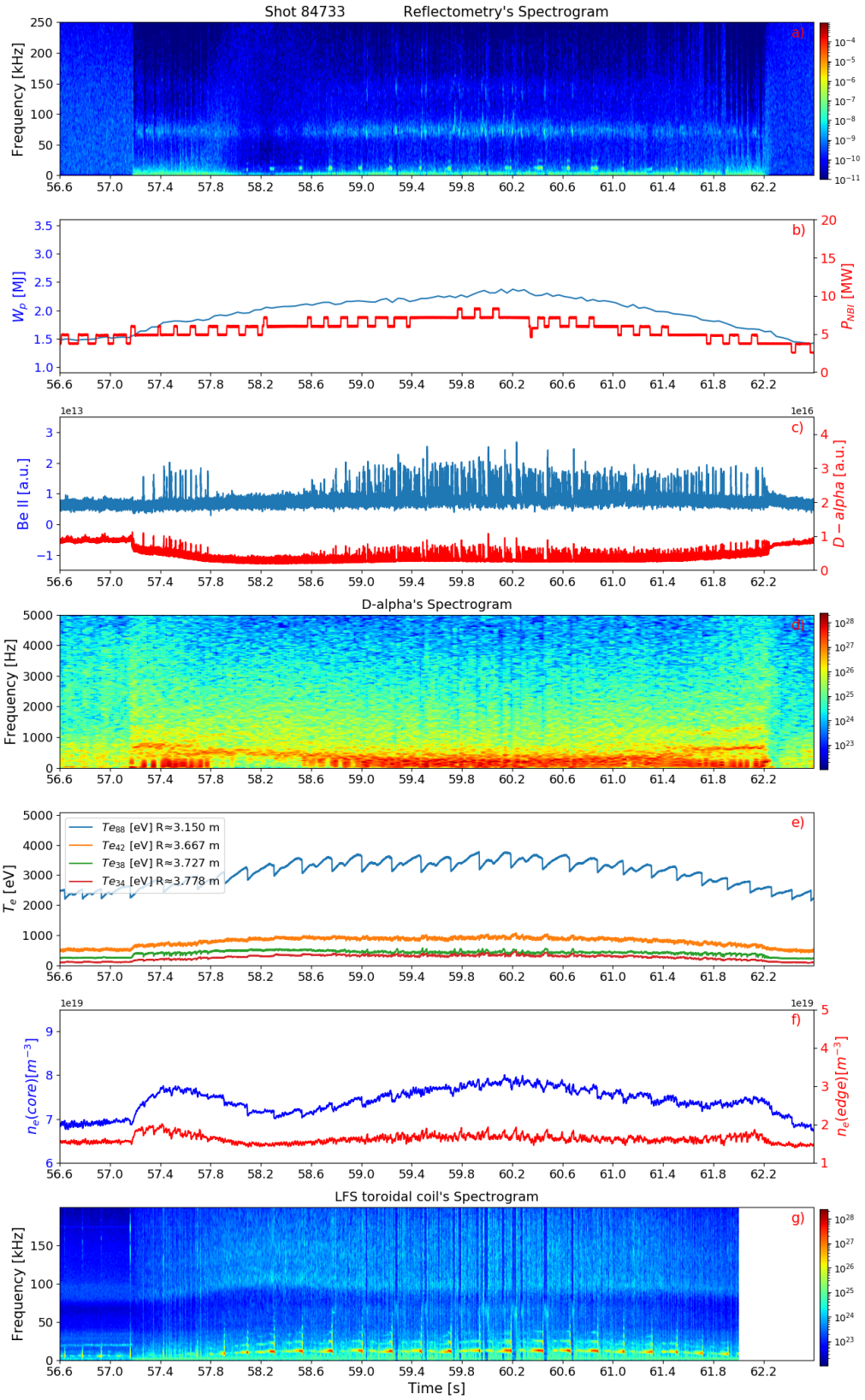

Figure 5.1: Evolution of Discharge 84733. a) Reflectometry's spectrogram; b) plasma's stored energy and NBI power; c) Be II and D_α's signals; d) D_α's spectrogram; e) electron temperatures, T_e, at different radial positions ; f) electron line-averaged density; n_e, at the plasma edge and core; g) coil T001's spectrogram

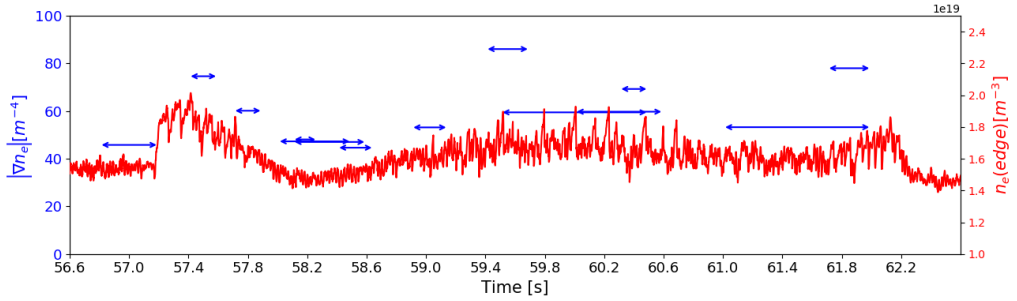

Figure 5.2: Evolution of the edge density in more detail (red line), intervals of density profiles and their absolute gradient at the inflection point at the steep gradient region (horizontal blue arrows)

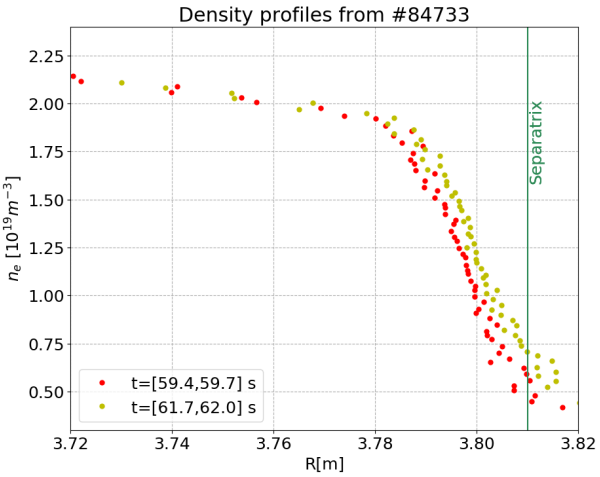

Figure 5.3: Density profiles of periods where the density gradient was overestimated.

Discharge 86469

The discharge 86469 is presented in the figure 5.4. Compared to the previous discharge, in the H-mode, it has an overall higher P_{NBI} with the maximum at around 10 MW compared to 8 MW in the previous shot. This translates to an increased plasma's stored energy, with an overall increase of 60% compared to #84733. The line-averaged density at the core is also greater, the maximum being around 16% higher.

The L-H transition occurs at t=56.3 s, indicated by the D_α's spectrogram, through the appearance of low frequency oscillations. The emergence of ELMs shortly after and the increase in the core's line-averaged density corroborates the occurrence of this transition. Compared to the preceding discharge, the change in temperatures and edge's line-averaged density was almost unnoticeable. This may be because the P_{NBI} waveform remains constant after the transition and does not increase much past the P_{LH} throughout the discharge. The H-mode is maintained until t=59.1s, and then changes back to the L-mode.

Looking at the electron temperature and line-averaged density most close to the core, Te_{72} and $n_e(core)$, the present sawteeth in this discharge between t=[56.5,59] s have a $f_{sawtooth} = 4.6 \pm 0.5$ Hz.

The evolution of the density gradients at the points of inflection seems to follow with the edge density with no outliers for this discharge.

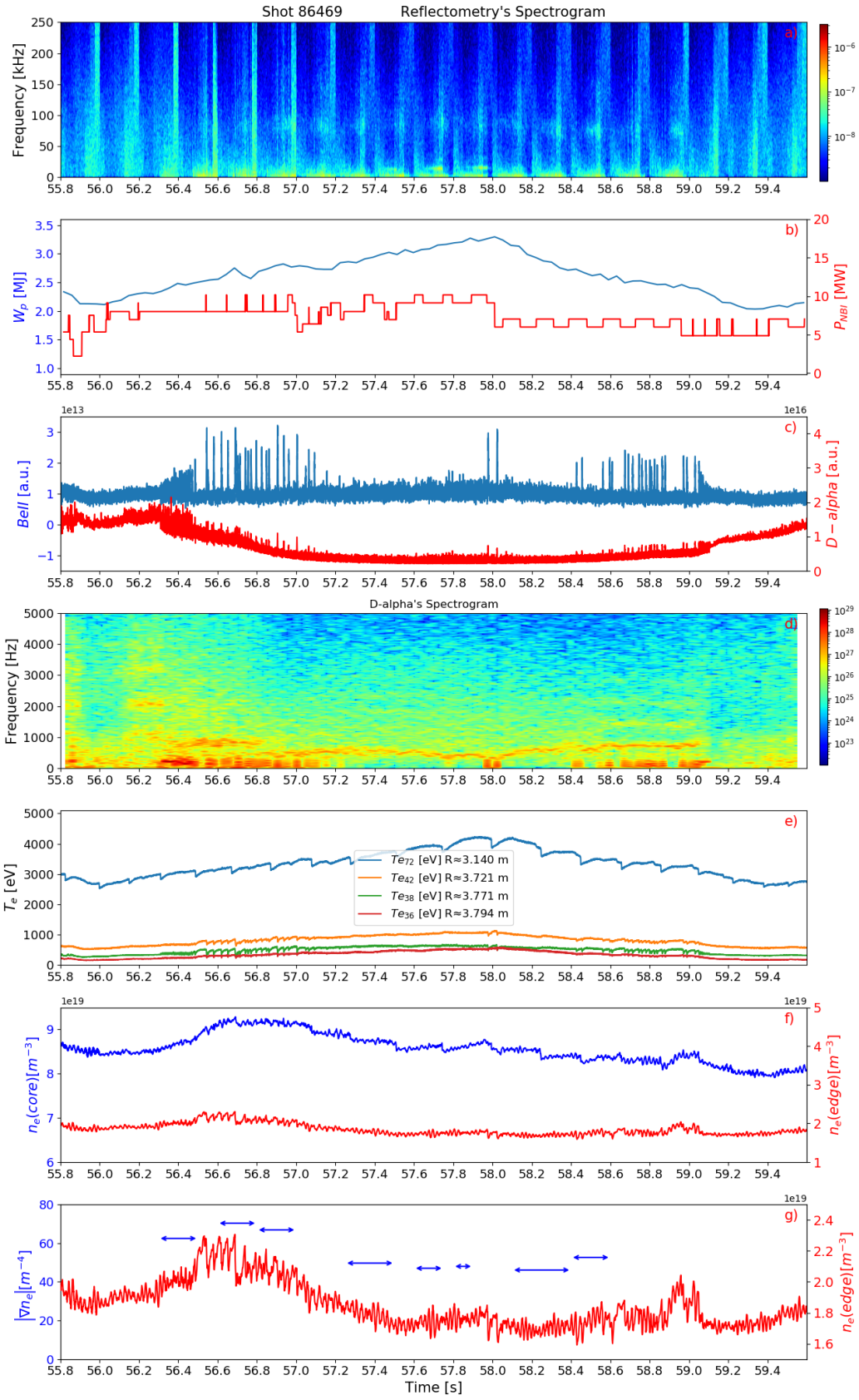

Figure 5.4: Spectrogram of reflectometry and D_α signals, time evolution of the main plasma parameters and density profiles and their absolute highest gradient (plot g) along discharge 86469 .

Discharge 86470

The discharge 86470 analysed is presented in figure 5.5. Compared to the other discharges, this one maintained the highest plasma stored energy. Electron temperatures of this discharge were much higher, specially at the core with differences of around 1 keV and almost 2 keV, for #86469 and #84733, respectively. The line-averaged density is not as high as the discharge #86469 and fluctuates throughout the discharge.

The L-H transition for this discharge is not as well defined because of the P_{NBI} waveform, once again, not increasing much beyond the P_{LH}. The plasma starts in the L-mode until t=53.85 s, where it changes to the H-mode. In this regime, although the density pedestal steepens notably, a weakened electron temperature pedestal forms as indicated by the modest increase in the edge T_e. This regime is characterised by axisymmetric magnetic oscillations called M-mode that have a frequency around 1-2kHz, with toroidal and poloidal mode numbers, n=0 and m=1 [33]. These oscillations that define this mode are present in the D_α signal until t=55.1s. At this moment they start to fade and oscillations of lower frequencies emerge. Only after t≈57 s, with an increase in the NBI power, there is a clear increase in the densities and ELMs appear. The H-mode exists until around t=60.6s.

The occurrence of stronger sawteeth is clear in the core temperature Te_{72} and its frequency between t=[56.4,60.4] s is $f_{sawtooth} = 3.5 \pm 0.5$ Hz.

The density gradients at the points of inflection also follow the evolution of the edge density in this discharge.

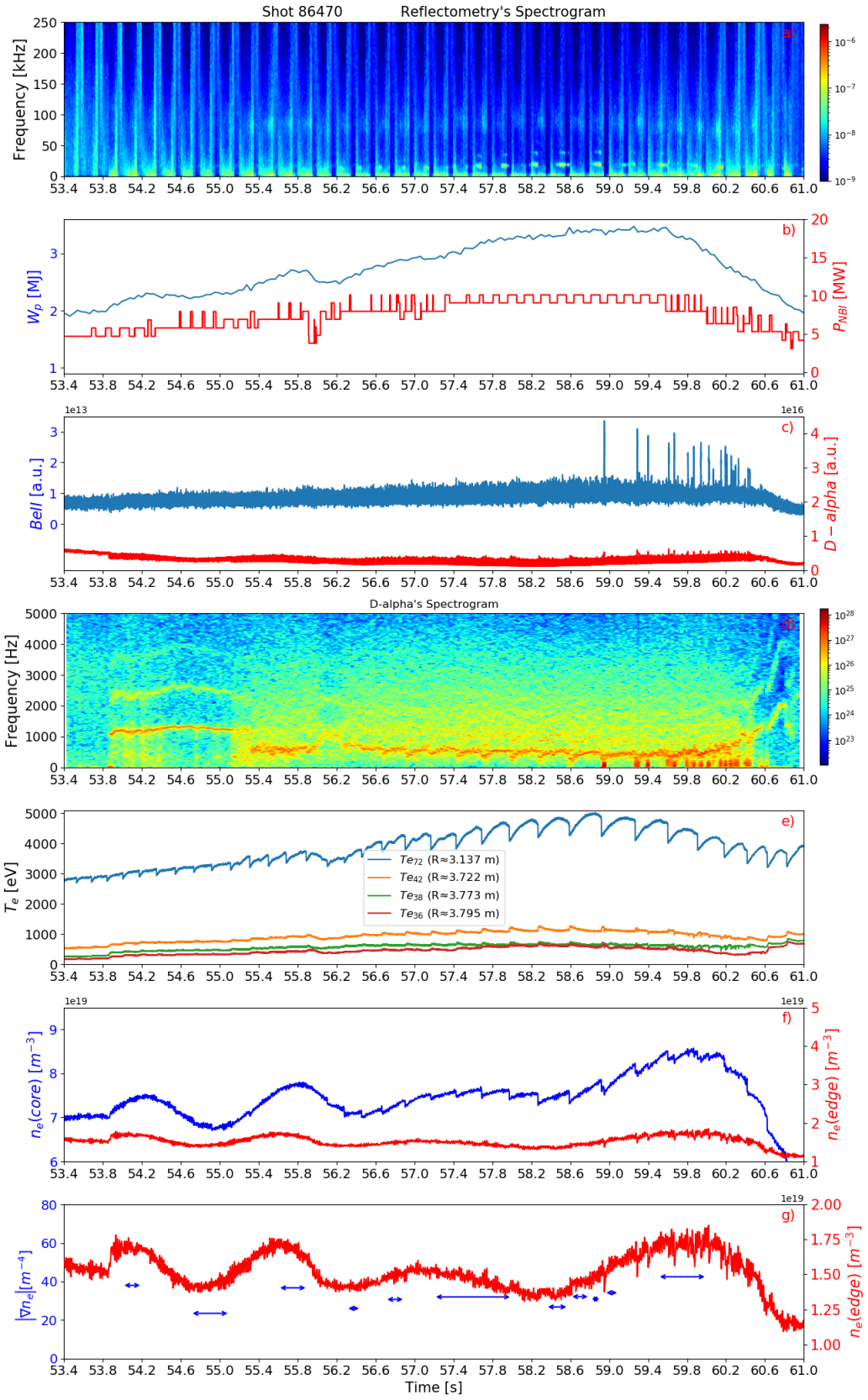

Figure 5.5: Spectrogram of reflectometry and D_α signals, time evolution of the main plasma parameters and density profiles and their absolute highest gradient (plot g) along discharge 86470.

5.1.2 Temporal evolution along the ELM cycle

Understanding the behaviour of the plasma quantities within the ELM cycle is important so we can eventually correlate them to the mode behavior.

Discharge 84733

In this discharge there are 2 sets of ELMs with different behaviour presented in the figure 5.6. One set at the beginning of the H-mode with regular ELMs of $f_{ELM} = 25 \pm 14$ Hz. Another set which has both ELMs of similar frequency and smaller ones that happen irregularly that increase slightly the Be II signal.

Whenever an ELM occurs, the Be II and D_α signals help identify it. The ELM causes events of strong heat fluxes into the divertor and first wall materials, which leads to the emitted radiation by the Deuterium and the sputtered Beryllium to rise abruptly. After the ELM, it decreases back to the baseline signal. For Be II, the baseline is mostly constant along the discharge, while for the D_α varies with different modes of confinement. When ELMs occur, the D_α signal is similar in shape to the Be II signal. But between ELMs, it has low frequency oscillations that are present throughout the discharge.

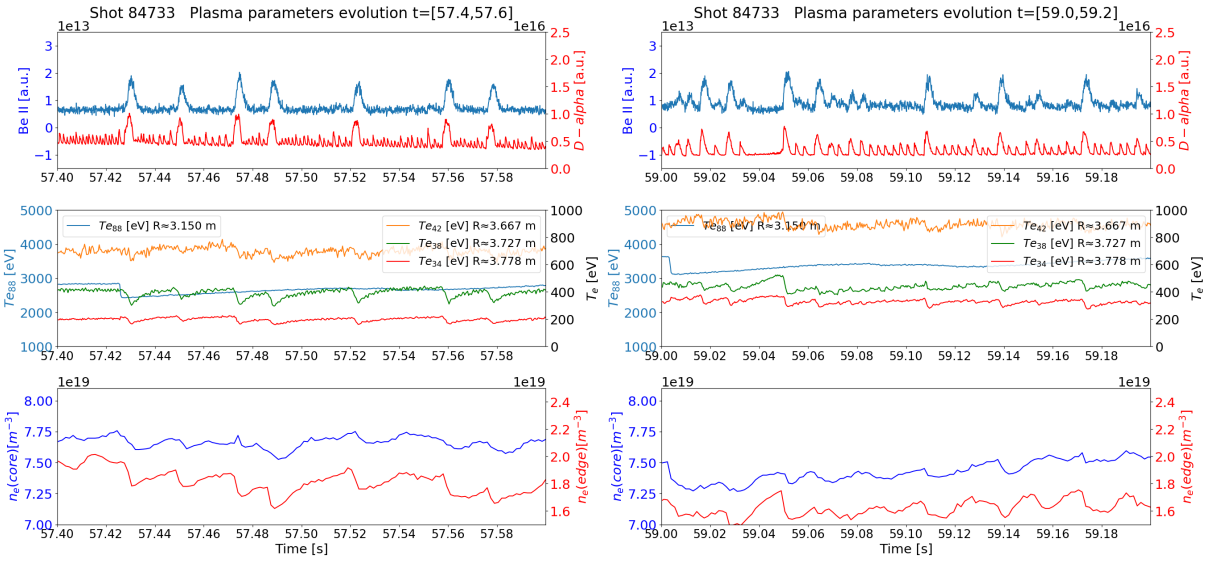

Figure 5.6: Example of set of ELMs, for the discharge 84733. The Be II and D_α's signals are plotted along with the temperatures at different radii (each axis is set for temperatures in closest legend) and electron line-averaged densities, n_e, at the plasma edge and core.

The electron temperature evolution between ELMs varies along measurement location. The temperature profile has a pedestal similar to the density profile but not as steep. Te_{88} ($R \approx 3.150$ m) is measured very close to the core plasma. As expected it does not show any influence of ELMs but rather of sawtooth events, with sudden drops in value. A few cm away from the top of the pedestal, Te_{42} ($R \approx 3.667$ m) is acquired. Because of some proximity to the edge of the plasma, Te_{42} shows some ELM effects that cause a dip in value followed by a slow recovery. Overall, the signal is very noisy and reacts very little to smaller ELMs, making it unreliable to correlate it to the ELM cycle. Te_{38} ($R \approx 3.727$ m) and Te_{34} ($R \approx 3.778$ m) are on the top of the pedestal and at the middle of the steep density gradient region, respectively. They have a very clear correlation and evolution affected by the ELMs. There are well

defined drops followed by a slow recovery until the next ELM. By being at the top of the pedestal, Te_{38} is the most sensible to the relaxation that the ELM causes to the temperature profile.

The line-averaged densities have abrupt drops in value after ELM events and usually have a steady recovery until the next one. Because these events occur near the pedestal, it is noticeable that the edge's chord density is more reactive than the core's. The core density barely fluctuates in some ELMs.

Discharges 86469/86470

The ELMs for these two discharges have smaller frequency which allows for better analysis of its parameters compared to the #84733. We show this in figure 5.7 of some ELM events and their associated plasma parameter evolution. There is a more coherent evolution of temperatures positioned slightly inside the plasma (Te_{42}) and at the top of the pedestal (Te_{38}). These quantities have a consistent behaviour of a fast drop after the beginning of the ELM, followed by an initial fast recovery and a slow build up until the next ELM. Te_{36} is at the middle of the steep density gradient region and is less reactive to ELMs, but, after they occur, the heat flux that propagates until the edge causes a slight increase in this quantity, followed by a reduction back to pre-ELM value. The Te_{72}, very close to the core, behaves similarly to Te_{88} of #84733.

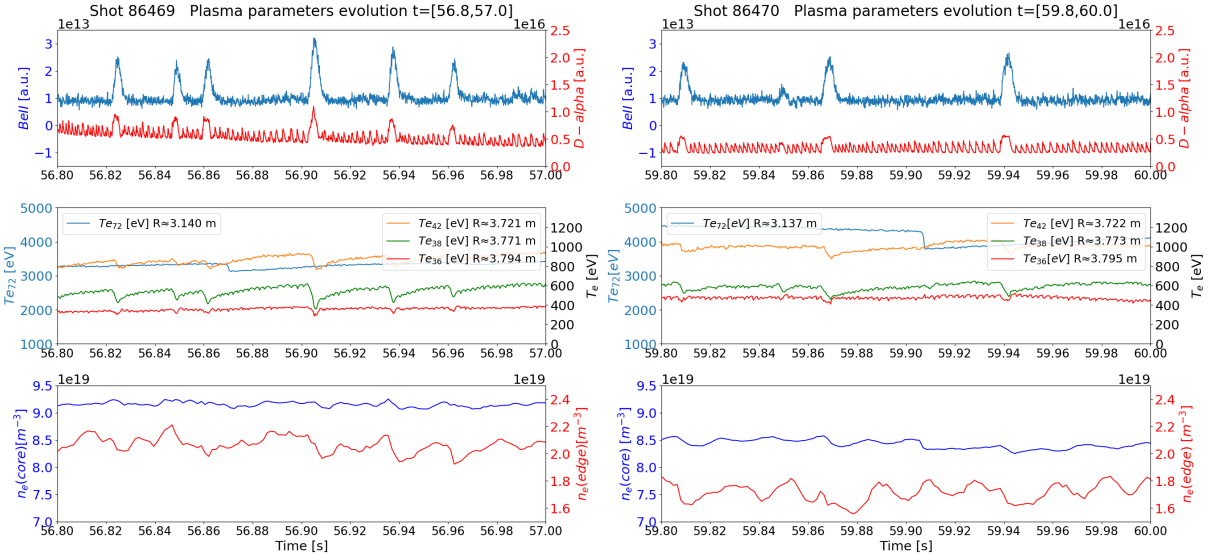

Figure 5.7: Evolution of plasma parameters through ELM events in discharges 86469 (left) and 86470 (right).

The core line-averaged density is reactive to sawtooth events in these discharges as well, more for the #86470 that has more intense sawteeth. The core density is somewhat responsive to ELMs. This density being influenced by ELMs could be counter-intuitive, since the data is supposedly from the core. This is probably because the measurement is not local but line-averaged, having therefore a contribution from the edge along the line of sight of the interferometer. Consequently, it includes the behaviour of the weakened pedestal at the edge after each ELM event. The edge density is, as expected, affected by the ELM perturbations, with a slower drop, compared to Te_{38}, followed by a fluctuating increase until the next ELM.

5.2 Characterization of measured fluctuations by reflectometry and comparison to the magnetic coils' signals

In this section we will study a mode with a frequency in the range 70-90 kHz visible in the density fluctuations of the edge plasma. The density fluctuations, δ_{n_e}, are observed through a radial correlation reflectometry system operating in Doppler mode because of the configuration of the plasma. Although Doppler reflectometry is normally used to measure rotation velocities of the turbulence, for the H-mode, turbulence is strongly reduced by the E×B shear. For this mode, the Doppler signal is very weak, giving opportunity for modes to dominate and become visible in the spectrogram. This allows for a better study of mode evolution. However, the interpretation is not straightforward, since in principle, for large modes, both δ_{n_e} and rotation velocity can contribute to the measured signal. This system provides heterodyne signals of in-phase and quadrature-phase (I.Q.), each with information about the amplitude and the phase. This diagnostic will be complemented by the input from Mirnov coils that measured from 4 positions in the tokamak as seen in figure 3.6. One in the HFS belonging to the Inner Coils group (I803); and three positioned in the LFS, with two in the Poloidal Limiter Coils group (P802B and P803B) and another in the Toroidal array (T001).

This section analyses the mode evolution in the context of the whole discharge and then in more detail along the ELM cycle. In each subsection, we show the results for the discharge when the CR is probing a single layer (#84733) and for the discharges with the CR probing multiple layers (#86469 and #86470).

5.2.1 General overview

Density fluctuations at a fixed layer

In the discharge 84733, the master and slave channel of the CR were pre-programmed to emit certain frequencies. The master channel was set to launch a single frequency while the slave channel was set to hop among 13 different frequencies, both channel configurations are shown in table 5.1. Using the I.Q. signals from the master channel, the spectrogram in figure 5.8 was estimated, only the positive frequencies are displayed and analysed due to the aforementioned symmetry of the complex amplitude spectrum in H-mode. A general analysis of the spectrogram show the presence of a mode at 70-90 kHz after the H-mode is achieved at t=57.2 s. This coherent mode is only present in the H-mode and seems to be correlated with ELM events. It is broad in frequency, strongest between ELMs and exists intermittently along the discharge.

# Shot	# PF	PFs (GHz)	Time step between PF (ms)
84733 (master)	1	73.44	0
84733 (slave)	1	73.46	2
	2	73.61	
	3	73.76	
	4	73.91	
	5	74.06	
	6	74.21	
	7	74.36	
	8	74.51	
	9	74.66	
	10	74.81	
	11	74.96	
	12	75.11	
	13	75.26	
86469 / 86470 (master)	1	73.5	25
	2	75.5	
	3	77.5	
	4	79.5	
	5	81.5	
	6	83.5	
	7	85.5	
	8	87.5	

Table 5.1: Emitted frequencies by the hopping reflectometry system and their time step for different discharges

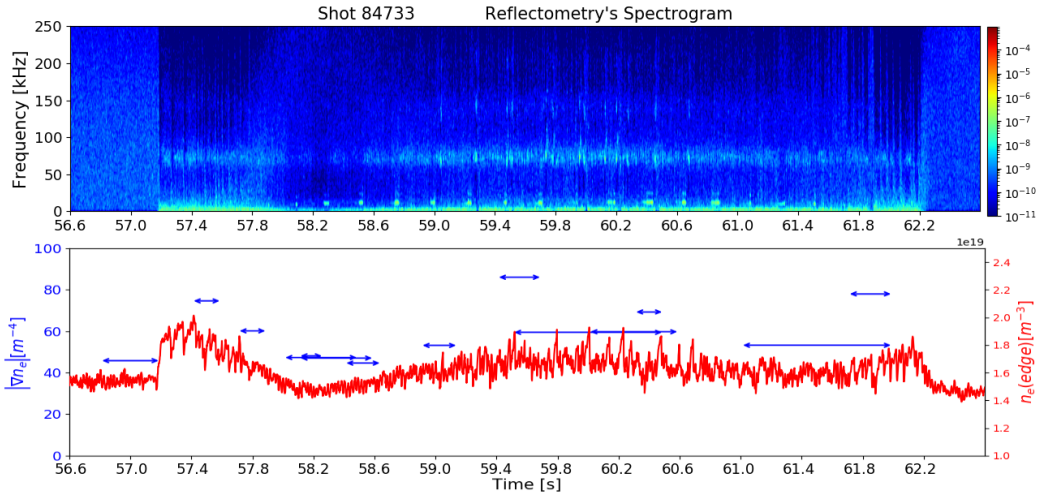

Figure 5.8: Spectrogram of reflectometry, density gradient at the inflection points of multiple density profiles and edge line-averaged density.

After looking more in-depth to this intermittent behaviour, it is not only characteristic to this coherent mode but is general to the Power Spectral Density (PSD), throughout the H-mode. The reason for this behaviour is visible in figure 5.9, where it is plotted the spectrogram of the master channel from CR (with D_α overplotted), the indicators of ELMs like Be II and D_α, the temperatures at different radii, the edge line averaged densities and the spectrograms of the used magnetic coils. The overplotted D_α in these spectrograms indicates that the smaller oscillations present in this signal are the cause of the intermittent behaviour. These oscillations have a similar shape to smaller scale ELMs. Whenever these

pulsations in the D_α reach their peak, there is an overall reduction of activity and disappearance of the mode. Such behaviour could be explained by a variation of the reflectometry signal amplitude associated with each oscillation. However, after normalising each PSD by its total power, the behaviour of the mode persisted, so we disregarded this possibility. In the magnetic signals, these oscillations cause momentary broadband fluctuations in the spectrogram that range up to 200 kHz. The oscillations in the D_α emerge as the H-mode is achieved and have a regular pulsating behaviour of up to 1 kHz. As W_p rises they reduce in frequency and in some intervals seem to evolve into type-III ELMs. These characteristics accompanied by their appearance just above the L-H threshold indicate they may be Limit Cycle Oscillations (LCO), that are observed in many other machines [34]. LCOs are regular pulsations in the low kilohertz range that occur at the edge of the plasma. By looking at a segment of the D_α pulsations from figure 5.9 in more detail and compared with the magnetic signals, we obtain figure 5.10. In this figure are plotted the signal evolution of two LFS coils (P802B and T001) and of one HFS coil (I803) signals with an added offset so we can distinguish them, also plotted is the D_α signal. This plot outlines the perturbation of the poloidal magnetic fields associated with these D_α pulsations. There is a magnetic pulsation synchronised with each D_α oscillation which is clear and present in all of the studied coils, being proportional in intensity with the D_α pulsations, confirming their correlation. This magnetic component in the D_α pulsations indicate they are LCOs since these also have a magnetic perturbation associated that was verified in other machines [34]. Although these oscillation may have interesting physics, they complicated the analysis of mode characteristics, so in order to have a more robust estimate of the mode evolution, we implemented for all discharges a spectrogram using a modified Welch method (described in chapter 4). It was built using 10 windows of 0.5 ms each, with overlap of 50 % of the points, resulting in averaged PSDs that are 2.5 ms long. There was also a overlap of 50% of points between consecutive PSDs that caused the final resolution of the spectrogram to be of 1.25 ms. Because each averaged PSD is using 2.5 ms of data and the oscillations have a period of about 1 ms, this means that the PSD will overlook the repetitive disappearance of the mode and allow for it to be more continuously studied.

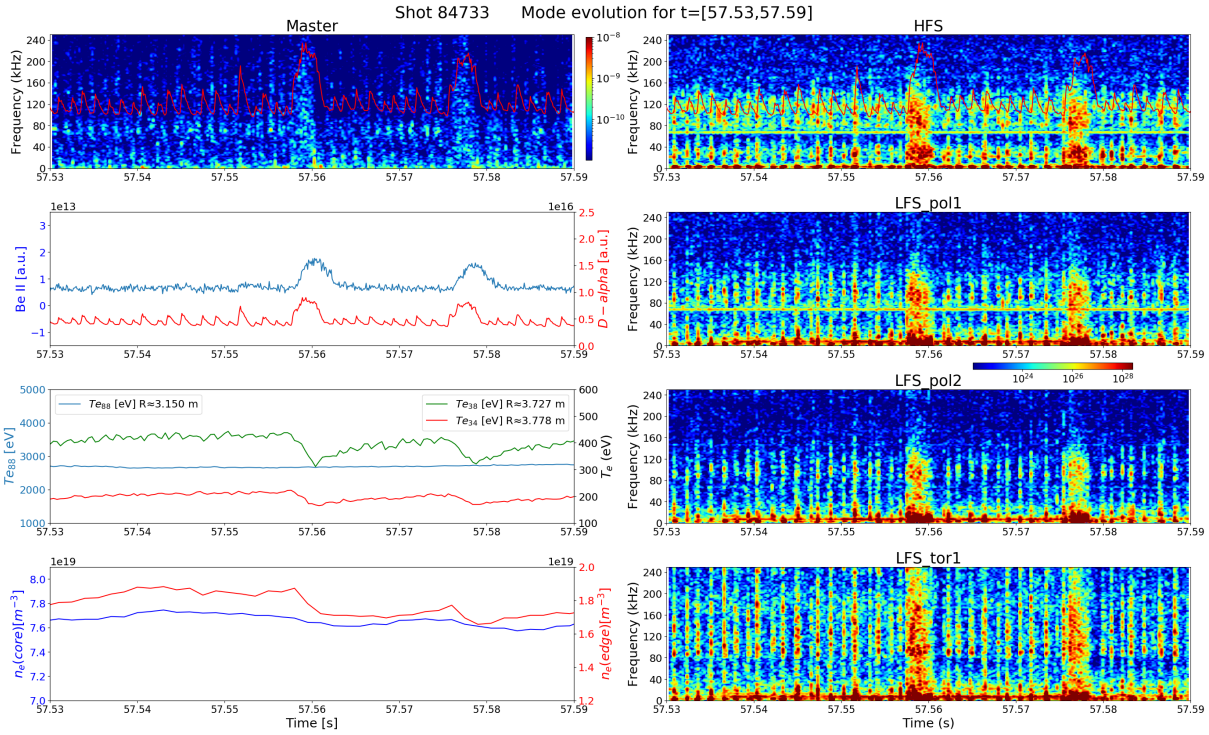

Figure 5.9: On the left are the spectrogram of the master signal with superimposed D_α signal and the plasma parameters. On the right, the spectrograms of the magnetic coils are plotted: I803 (HFS) with D_α on top (red line), and the rest are LFS coils P802B (LFS_pol1), P803B (LFS_pol2) and T001 (LFS_tor1)

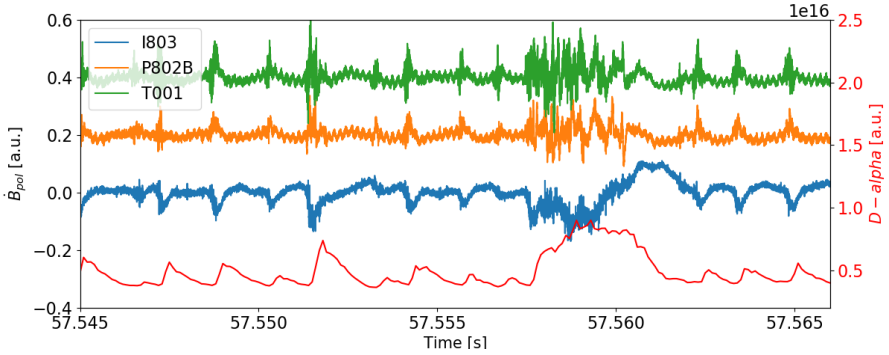

Figure 5.10: Short segment of the LCOs in the Magnetic and D_α signals

In the spectrogram of this discharge, visible in figure 5.8, the mode varies intensity along time. It becomes very faint when the edge density drops below $\langle n_e \rangle \approx 1.6 \times 10^{19} m^{-3}$, at t=58 s, and is noticeable again after a recovery in density at t=58.538 s, a few tenths of a second before ELMs reemerge. The electron density profiles give insight on why the intensity is reduced in some regions. Plotted in figure 5.11 are the density profiles of regions where the mode varies in intensity. The mode is clearly visible and intense in the CR just after the L-H transition (t=[57.4,57.6] s) and at around t=[59.5,60] s. These density profiles are steep and the probed region is similar in the two periods at $R \approx 3.788$ m. In the period when the mode seems to disappear, the density profile (t=[58.1,58.6] s) shows a lower gradient and the CR probing more inside the plasma at $R \approx 3.76$ m. From these observations, the mode intensity seems to be correlated with the density gradient, becoming more intense as the gradient steepens. However,

this correlation is debatable since the density profile varying also causes the plasma region being probed to change. This could be the cause of the mode intensity reduction since the CR changes from probing the top of the pedestal (where the mode could be localised) to more inside the plasma (where the mode is faint or nonexistent).

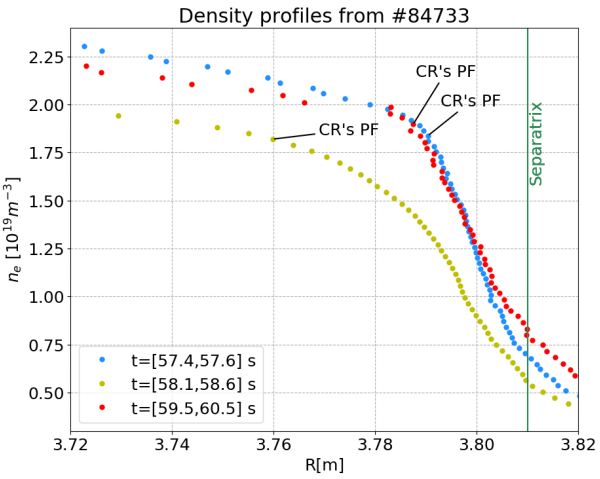

Figure 5.11: Density profiles in periods where the mode (60-90 kHz) intensity varies, annotated are the regions being probed by the reflectometer

Density fluctuations in multiple layers

The reflectometer allows, for each channel, to be pre-programmed with a specified launch frequency pattern. The chosen frequencies are repeated continuously throughout the discharge, allowing a radial scan of the measurement location. For the discharges 86469 and 86470, one of the reflectometer channels (master) was set to a 8 point frequency sweep. Each frequency had a duration of 25 ms, with the full sweep taking 200 ms. The set of frequencies used are in table 5.1. By changing the layer being observed every 25 ms, it allows to identify the mode's frequency and intensity along the radius. However, the localisation of the mode comes at the cost of the ability to follow its temporal evolution, since each probing frequency (PF) is only repeated every 200 ms. The resultant spectrograms with this launch frequency pattern are in figures 5.12 and 5.13. For the same reasons mentioned before for the discharge 84733, the spectrogram studied for mode detection uses a modified Welch method. Taking into consideration the change in the probing frequencies along time, the windows of the spectrogram were selected to include data only for one PF, therefore avoiding the interpretation difficulties resulting from using data of two PFs in the same PSD.

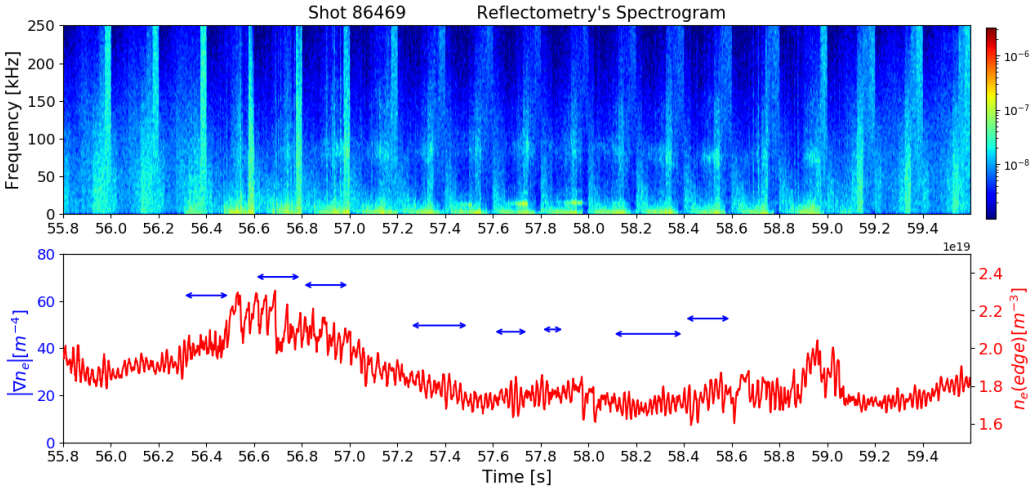

Figure 5.12: Spectrogram of reflectometry, density gradient at the inflection points of multiple density profiles and edge line-averaged density.

A similar mode to the previous discharge also appears in the reflectometry spectrograms of these two discharges. Initially very wide, it varies the frequency around 70-90 kHz and seems to emerge after the H-mode is achieved. It only becomes better defined at t=56.8 s for the discharge 86469. At this point the oscillation at around 1000 Hz in the D_α's signal changes to 500 Hz and allows for the mode to be dominant. In the discharge 86470 the mode appears after the M-mode disappears at around t=55.312 s.

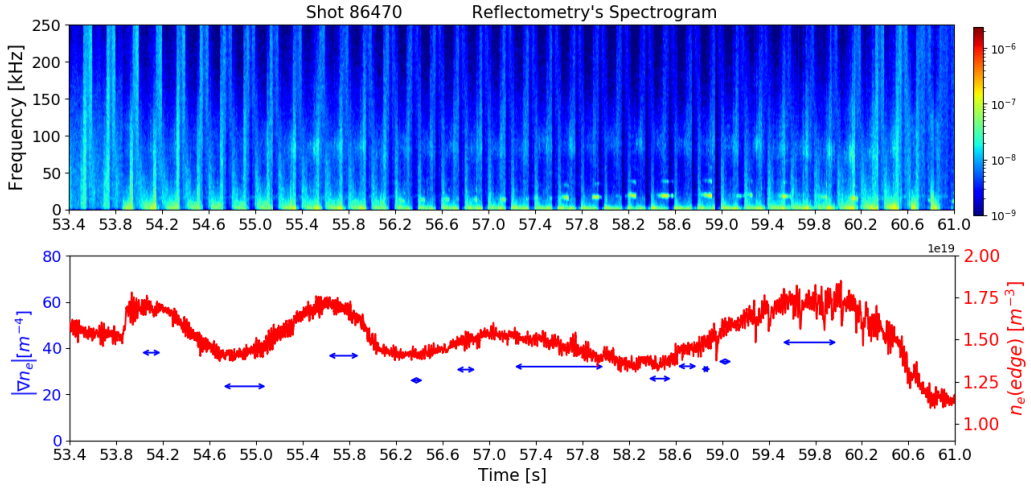

Figure 5.13: Spectrogram of reflectometry, density gradient at the inflection points of multiple density profiles and edge line-averaged density.

A quantity that seems to determine the mode behaviour is the edge density (and consequently density gradients). Observing the mode intensity in the spectrograms of figures 5.12 and 5.13, it is apparently stronger for higher edge densities. For example in #86469 at t=[56.9,57.2] s the density is at its highest and the mode appears very well defined, but as the density drops in the following instants, so does the mode visibility. Another example is at t=[58.4,59] s where the the mode intensity starts to increase again along with the edge density. In #86470, this is also noted at t=[55.4,55.8] s, where the mode becomes more or less defined as the edge density increases or decreases. Also, at t=[59.4,60.2] s, as the edge density becomes increasingly more defined, so does the mode. These examples indicate that there may

be a correlation between the mode intensity and the density gradient at the edge.

A particular behaviour that is worth noticing is that mode frequency seems to vary with the P_{NBI}. In the spectrogram of #86469, figure 5.12, the mode frequency changes a few moments after an increase in P_{NBI} at t=57.32 s. By comparing the mode at t=[56.8,57.2] s to t=[57.6,57.8] s, there is a rise in frequency from 70-90 kHz to 80-100 kHz. The opposite is shown in figure 5.14 that has the localisation of each PF (in plot a), obtained with the method described in chapter 4; the signals of n_e(edge) and Te_{38} (in plot b); the spectrogram of the master channel, with the signals of D_α (in red) and Be II (in white) overplotted (in plot c); mode detection in the frequency ranges 50-100 kHz (in plot d) and 5-50 kHz (in plot e). By comparing the 5.14a (t=[57.6,57.8] s) and 5.14b (t=[58.2,58.4] s), one can notice that 0.2 s after the P_{NBI} is reduced, at t=58 s, the mode drops back to frequencies of 70-90 kHz. There is a tendency of the mode frequency to increase and decrease along with the P_{NBI}, this trend was also verified in the discharge 86470. The dependence of the mode frequency on the heating power occurs because an increase in P_{NBI} causes a higher rotation of the plasma. This consequently causes the layer where the mode exists to rotate faster, increasing the mode frequency.

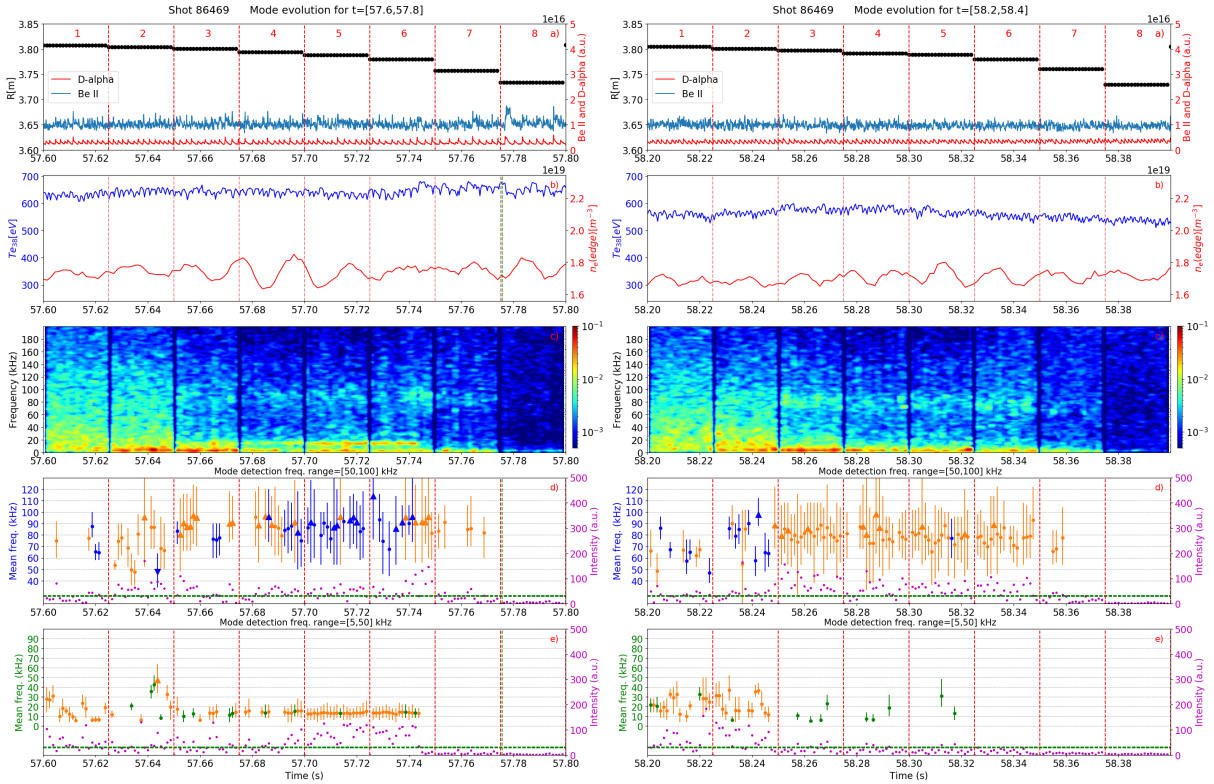

(a) Mode at higher frequencies, $P_{NBI} \approx 9.5$ MW

(b) Mode at lower frequencies, $P_{NBI} \approx 6.5$ MW

Figure 5.14: Mode evolution for different P_{NBI} in #86469. a) Radial location of the probing frequency and signals of Be II (in blue) and D_α (in red) overplotted; b) Te_{38} and n_e(edge); c) spectrogram of the reflectometry; frequency and intensity (in magenta) of the modes identified in different frequency ranges: d) 50-100 kHz; e) 5-50 kHz. The dashed vertical red lines signal the change in the PF of the reflectometer, the 8 PFs are annotated in increasing order.

In the reflectometry's spectrogram, another coherent mode is noticeable in the H-mode just before some sawtooth events that we call sawtooth mode. This mode is visible in plot e) of figure 5.14a at a frequency of 15 kHz and during t=[57.7, 57.745] s. It is noticeable for appearing more intensely in

the reflectometry signal before some stronger sawteeth happen, after the sawtooth takes place, like for example at t≈57.745 s, the sawtooth mode always disappears. In the discharge 86470, it is noticeable that the frequency of this sawtooth mode varies along the discharge: it starts at around 13 kHz, visible in figure 5.15a, appears at t=56.23 s and after the sawtooth also vanishes at t=56.28 s. The sawtooth mode increases in frequency gradually until t=58.2 s, where the frequency is around 20 kHz, presented in figure 5.15b. In this figure the sawtooth mode disappears after the sawtooth as well at t=58.27 s. In figure 5.16, we have the spectrograms of a HFS and LFS coil for the same intervals as figure 5.15, and the mode is also present with the same varying frequencies. The sawtooth mode has a much higher intensity in the magnetic signals and exists throughout the discharge, only disappearing briefly after the sawtooth events. There seems to be some connection between this sawtooth mode and the mode of interest since when it is present and intense in the reflectometry signal, there is a decrease in the strength of the mode at 70-100 kHz. This is illustrated in figure 5.15b, and it is noticeable that after the sawtooth occurs, the mode at 70-100 kHz increases in intensity immediately after to normal values. This phenomenon happens in other intervals of the discharge 86470 and in the discharge 84733, its cause may be a magnetic instability associated with the sawtooth affecting the main mode being studied.

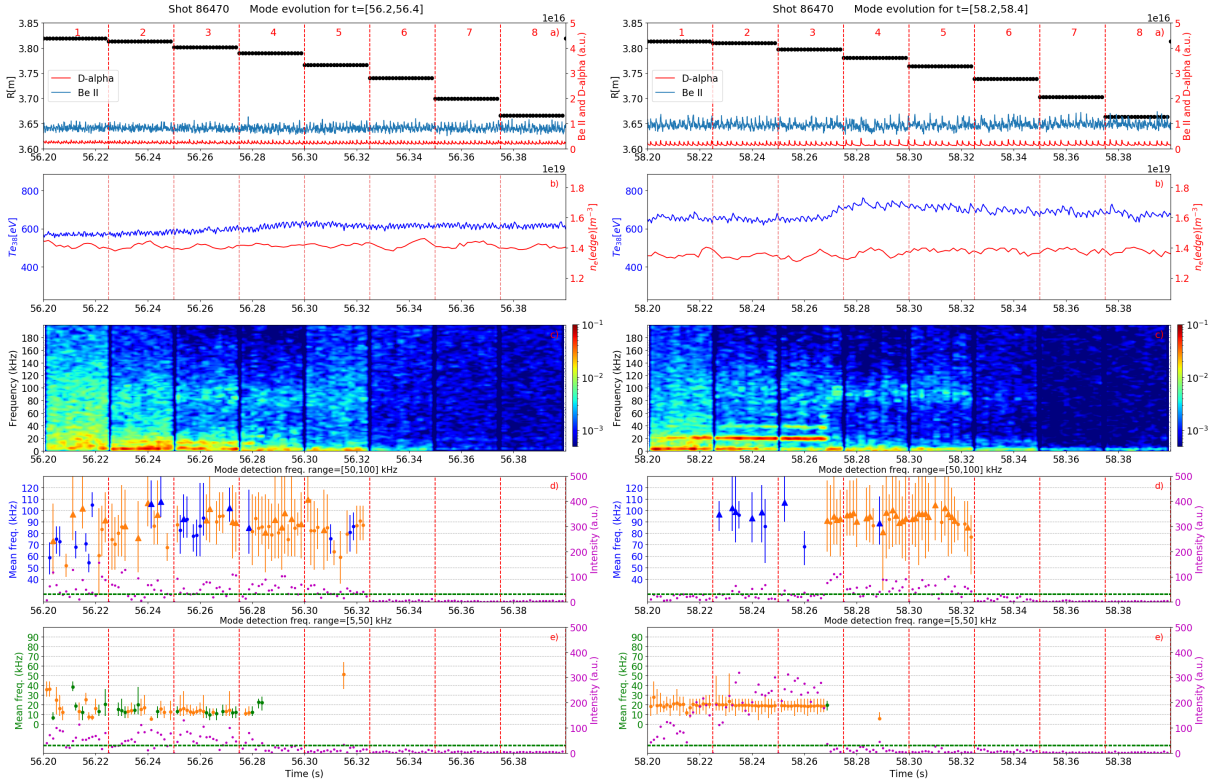

(a) Mode at lower frequencies, $P_{NBI} \approx 7.5$ MW

(b) Mode at higher frequencies, $P_{NBI} \approx 9.5$ MW

Figure 5.15: Mode evolution for different P_{NBI} in #86470.

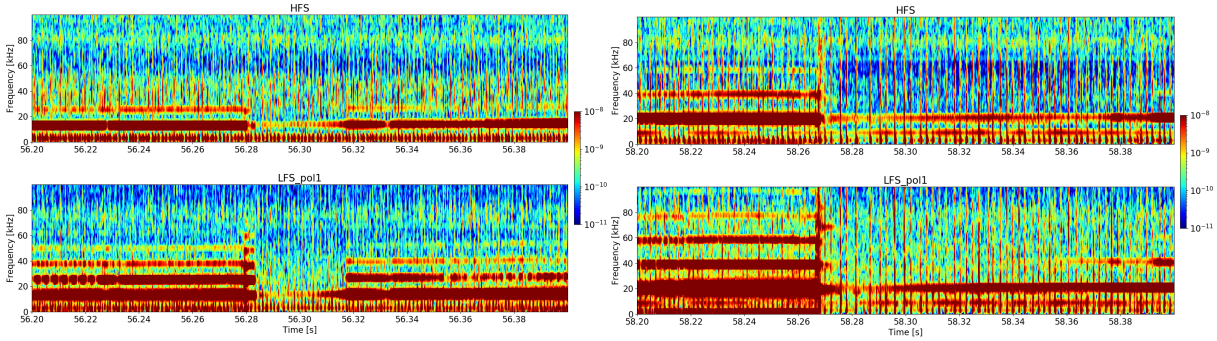

(a) Mode at lower frequencies, $P_{NBI} \approx 7.5$ MW

(b) Mode at higher frequencies, $P_{NBI} \approx 9.5$ MW

Figure 5.16: Sawtooth mode at different P_{NBI} of #86470 in the spectrograms of magnetic coils I803 (HFS) and P802B (LFS_pol1)

5.2.2 Along the ELM cycle

Between ELMs, the mode evolution in the reflectometry's spectrogram is important to explore, allowing to understand them better and if they may influence in triggering ELM events.

Density fluctuations at a fixed layer

The discharge 84733 had two sets of ELMs with different behaviour, as mentioned before, that are studied in deeper detail.

First set of ELMs

The evolution of the plasma parameters for a few ELMs close to the L-H transition are presented in figure 5.17. In this figure are also plotted the evolution of the edge density and temperature, as well as the modes detected in three frequency ranges. The method to detect and characterise these modes is described in chapter 4. Each mode detected has a frequency, a width and an intensity associated. One mode around 30 kHz wide and frequency between 70-90 kHz stands out in the reflectometry signal. This mode frequency does not vary much in the ELM cycle. There are some identified frequencies wider than usual that can be attributed to a failure in the baseline detection and subtraction, that cause the mode to be signalised as wider and more intense than it is. This mode disappears momentarily with an abrupt intensity loss whenever an ELM occurs. After the ELM, there is a recovery to pre-ELM intensities that seems to be somewhat related to the evolution of the edge density. Once the intensity of the mode stops increasing, it usually fluctuates over a value until the next ELM.

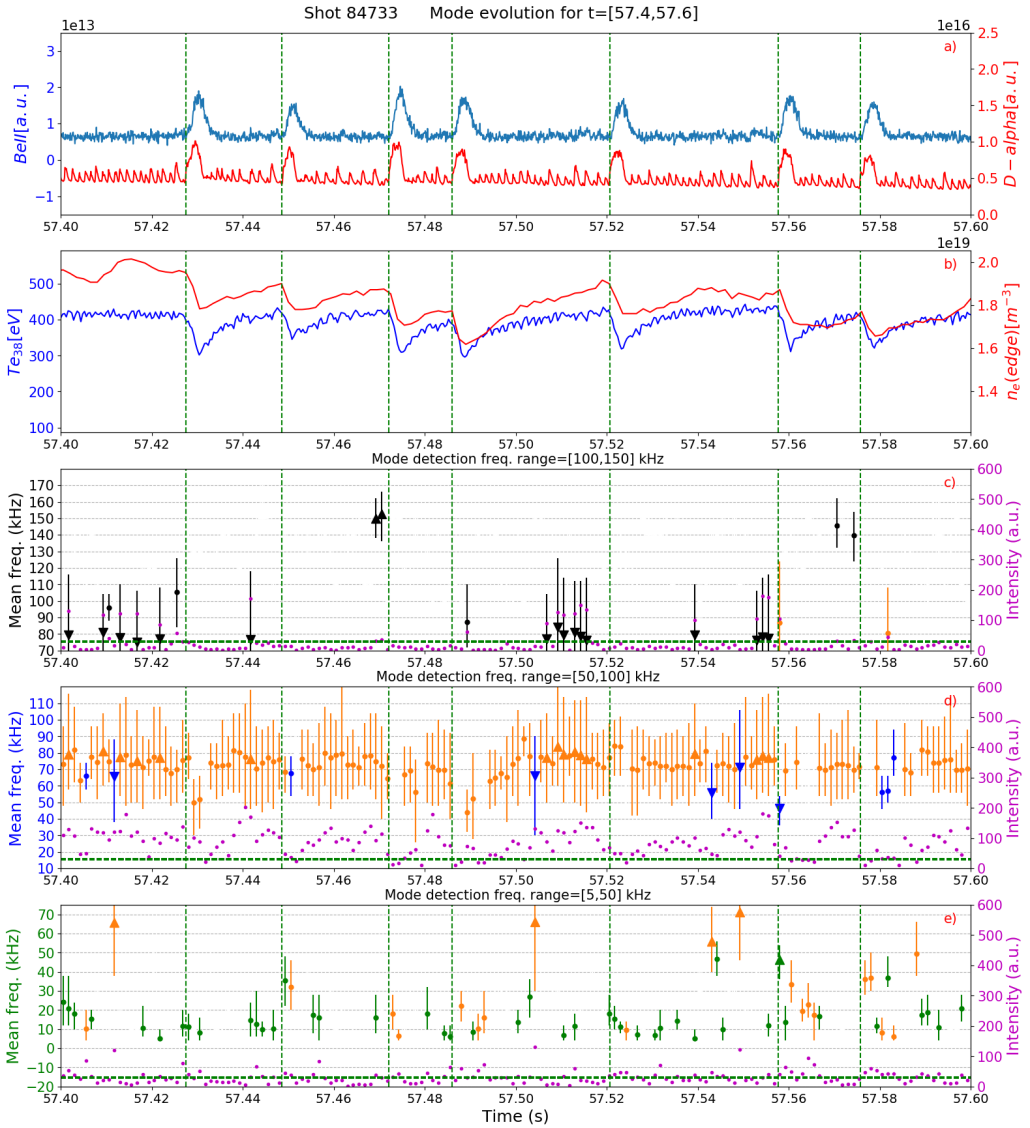

Figure 5.17: Mode evolution between ELMs. a) Be II and D_α signals, b) Te_{38} and n_e(edge), frequency of the modes and their intensity (in magenta) identified in different frequency ranges: c) 100-150 kHz; d) 50-100 kHz; e) 5-50 kHz.

Within the ELM cycle, the observed correlation between the mode intensity and the edge's line-averaged density indicates that the mode does not exist for lower density gradients (right after the ELM crash) and becomes more intense as the density gradient steepens. However, there is the possibility that the ELM crash may be causing a temporary low density profile. This changes the probing region to more inside the tokamak, where the mode is faint, consequently reducing the mode intensity. As the density profile recovers, the CR starts scanning closer to the steep gradient region, where we suppose the mode is localised, increasing the mode intensity and explaining the correlation between this quantity and the edge density. Although it is more probable the mode intensity is varying due to the gradients dropping, we can't be sure what is causing the mode intensity evolution by probing a single plasma layer. The following discharges (#86469 and #86470) will help clarify this question as these probe the plasma at different radii. They will allow to determine if the mode changes position and if its intensity is dependent on density/temperature gradients.

Second set of ELMs

In the second set of ELMs, although they are more frequent, there are inter-ELM periods without the D_α oscillations. These periods allow for a better characterisation of the mode at 70-90 kHz. In these occasions, the recovery of the mode intensity after the ELMs seems to follow the edge line-averaged density, rather than the temperature, Te_{38}. Examples of these stronger ELMs without D_α oscillations are illustrated in figure 5.18 at t=[59.465,59.485], t=[59.725,59.742] and t=[59.768,59.795].

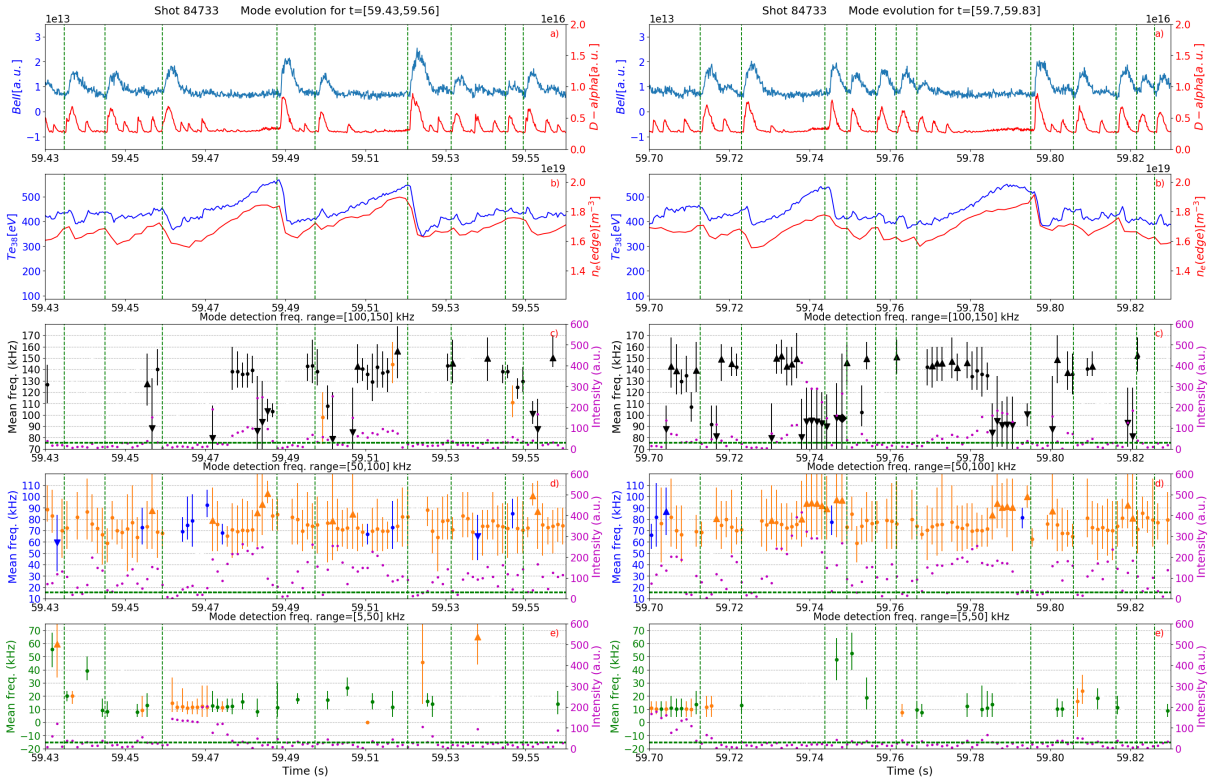

Figure 5.18: Plasma parameters and mode evolution in different frequency ranges between ELMs

These stronger ELMs that are preceded by the temporary disappearance of the D_α oscillations were studied more in depth. Two of them are displayed in figure 5.19. In this figure are illustrated the spectrograms of the master channel (plot a) and the slave channel (plot g). The parameter evolution is also shown (plots h, i and j), as well as the evolution of the modes in different frequency ranges of the master channel (plots b, c and d), similar to the figure 5.18 layout. The spectrograms of the magnetic signals are also presented for the HFS coil (plot e) and the three LFS coils (plots f, l and m).

The reduction in the D_α oscillations of these ELMs allows to observe a mode in the magnetic signals very similar in frequency and behaviour to the one in reflectometry. This magnetic mode appears mostly for these specific ELMs exclusively in the LFS, no signs of it were observed for the HFS coil. Looking at a whole spectrogram of the LFS toroidal coil in figure 5.20, the magnetic mode is faintly visible before some of these particular ELMs, but overall is not present.

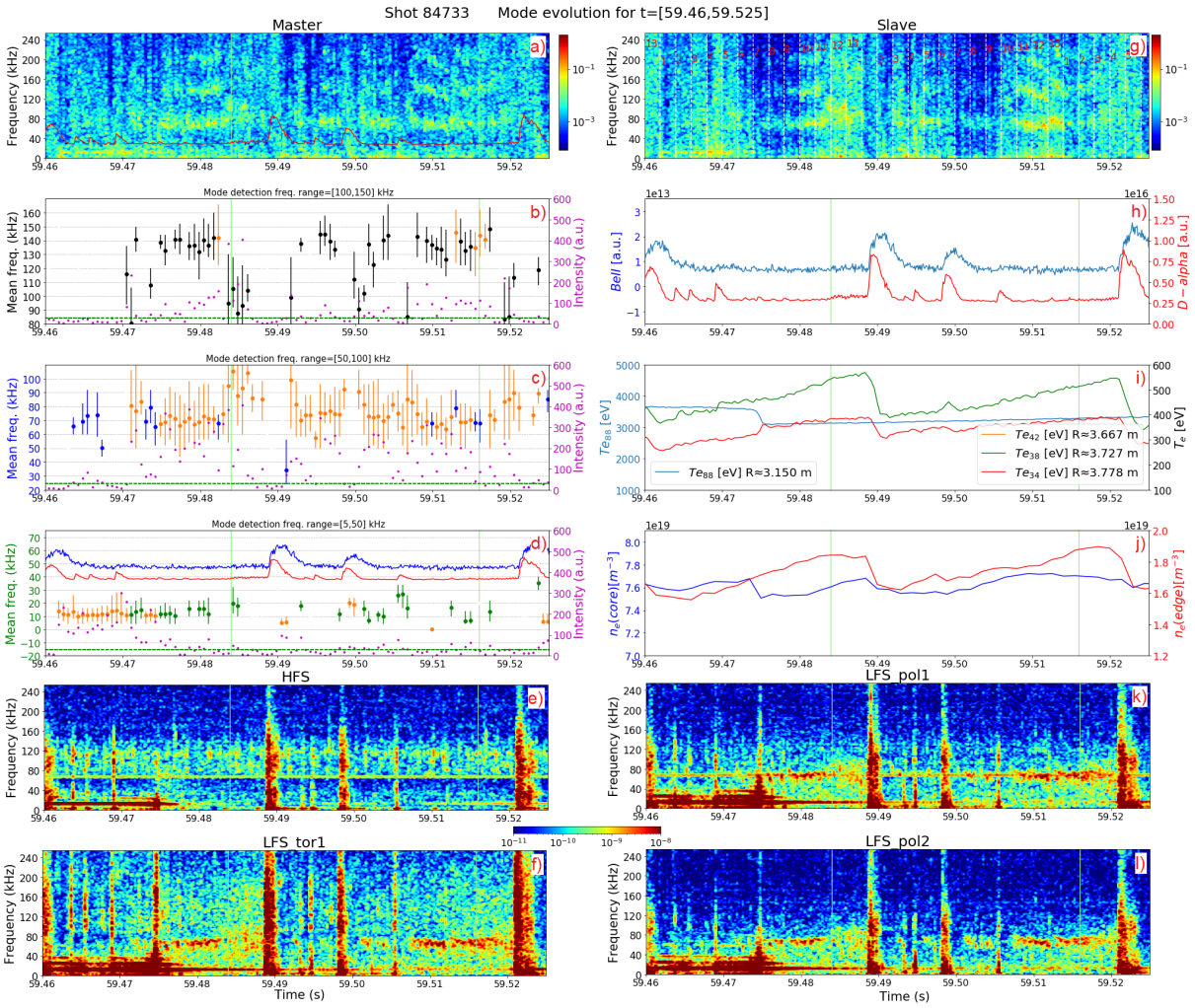

Figure 5.19: Detailed analysis of two intense ELMs. a) spectrogram of the master channel; frequency of the detected modes and their intensity (in magenta) at different frequency ranges: b) 100-150 kHz; c) 50-100 kHz; d) 5-50 kHz (overplotted are the Be II, in blue, and D_α in red); g) spectrogram of the slave channel; h) Be II and D_α signals; i) temperatures at different radii; j) electron line-averaged densities, n_e, at the edge and core of the plasma; spectrograms of magnetic coils signals: e) I803 (HFS) ; f) T001 (LFS_tor1); l) P802B (LFS_pol1); and P803B (LFS_pol2).

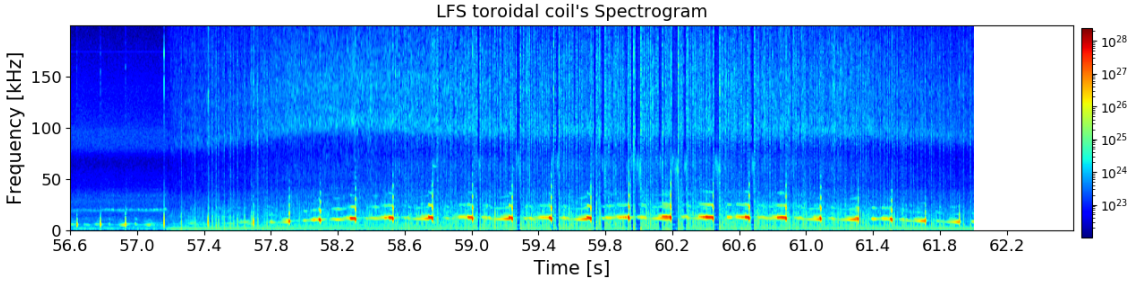

Figure 5.20: Spectrogram of LFS coil T001.

These longer periods without ELMs have the particularity that the 70-90 kHz mode becomes very well defined, a few instants before the ELM crash. This happens in both the reflectometry and magnetic signals. In the reflectometry signal these modes are so intense that a second and sometimes third harmonics are visible. In figure 5.19 this happens at t=59.48 s, the main mode (in plot c) at 60-80 kHz

has a second harmonic at 130-150 kHz (in plot b) and a third harmonic at 200-220 kHz (visible in plot a). The magnetic spectrograms do not show any sign of these harmonics, so their appearance in the reflectometry's signal should be an artefact. The reason being that the complex I.Q. depends on the amplitude of the reflected signal and on the sin/cos of the phase and therefore this non-linear dependence may lead to the observed harmonics. From inspection of the periods between these ELMs, two phases may be identified in the mode evolution. We can see two examples of this in figure 5.19 with the transition between the two stages being marked by a vertical green line. An initial phase, at t=[59.475,59.484] s and t=[59.508,59.515] s, where the mode becomes increasingly strong with intensities above the usual for this mode in normal ELMs. Followed by a phase, at t=[59.484,59.488] s and t=[59.515,59.521] s, where the mode reduces intensity, definition and becomes less coherent (much broader in frequency) until the ELM event. By looking at the spectrogram of the slave signal (in plot g) the mode is also present. The slave channel probes regions more inside the plasma, as can be seen in figure 5.21 of a typical density profile, the PFs cover the top of the pedestal and a bit inside the plasma, being useful to understand the mode extension for smaller radii. The probing frequencies (PFs) used by this signal are shown in table 5.1 and are pointed out in the spectrogram from 1-13 with the vertical white lines signaling the change in PF. The mode seems to exist along the top of the pedestal in the phase when the mode is coherent. After the phase transition, it shows the mode much broader and disappearing after t=59.485 s (in the PF 12). The behaviour is very similar to the master signal along the different PFs and there is no sign that the mode changes position to more inside the plasma after the phase transition.

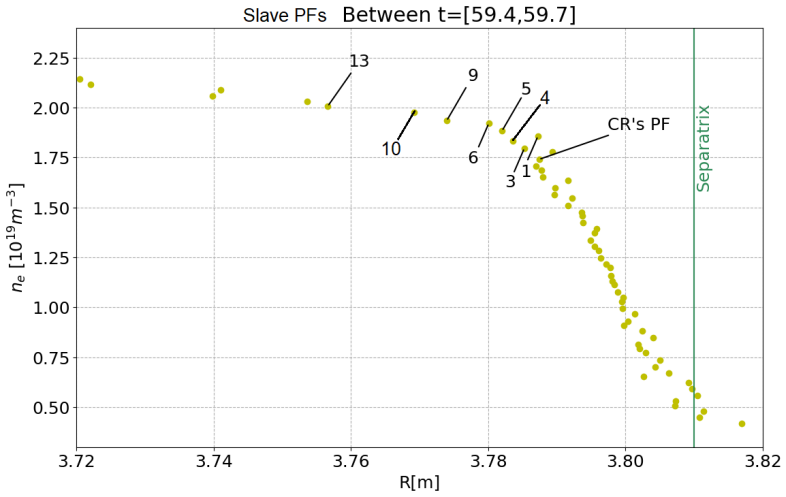

Figure 5.21: Probing frequencies of the slave (1-13) and master (CR's PF) channel in the density profile.

Most of these intense ELMs behave similarly to the one presented in figure 5.19, but there are a few that differ, like the one presented in figure 5.22. For this ELM, the mode changes behaviour in the magnetic and reflectomety signals when the edge density saturates for a short time. After this parameter increases again the mode reappears in the magnetic signal of LFS coils, but remains weak in the master channel of CR. The temperature at the top of the pedestal, Te_{38}, also seems to be somewhat related to the mode evolution with the mode becoming less coherent when the temperature is close to its maximum. In this phase transition, the mode also seems to extend to the top of the pedestal before and after the

mode becomes less coherent, existing up to the PF 12 at t=60.214 s, and from then no signs of it until the ELM crash.

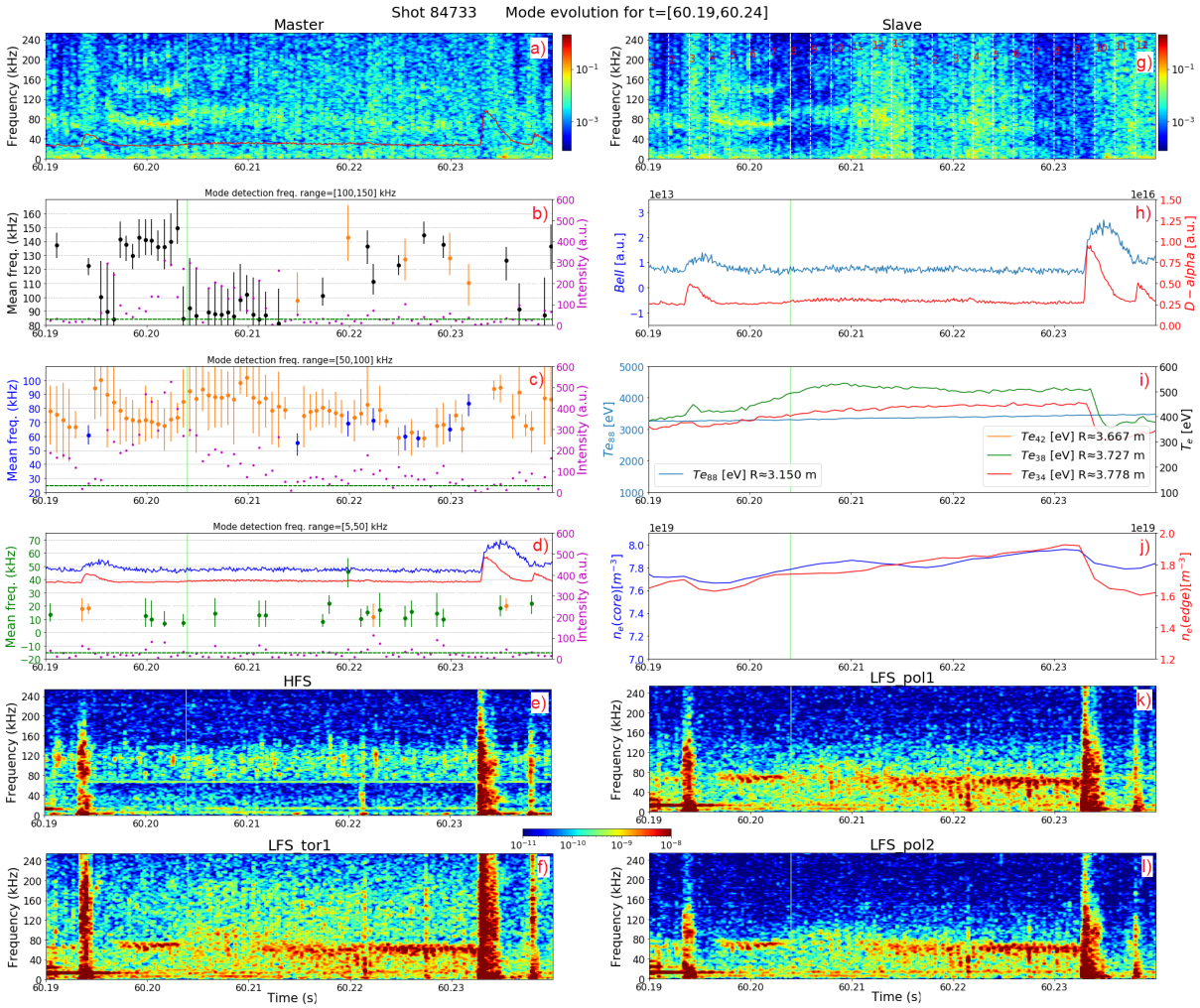

Figure 5.22: Detailed analysis of intense ELM with magnetic mode recovery.

After observing more of these ELMs like the ones presented, the onset of the second phase can usually be correlated with the saturation of the edge density and with an increase of D_α fluctuations. Indicating these oscillations may be causing increased transport which in consequence limits the density evolution. The mode is often not detected in the master reflectometry signal before some of these ELMs, suggesting the mode moves location after this change or due to becoming very broad in frequency and of lower amplitude. Looking at the magnetic signals' spectrograms, this mode only exists in the low field side, with no signs of it existing in the HFS coil, suggesting a ballooning character of the mode. After the second phase begins, there is an increase in broadband fluctuations. For the toroidal LFS coil these range up to 200 kHz, for the P802B and P803B coils they are up to 90 kHz.

In order to compare the mode characteristics in the reflectometry and magnetic signals, the mode in the ELM at t=59.49 s of figure 5.19 was analysed in more detail. We chose the intervals before and after the phase transition to overplot an averaged power spectrum of CR and magnetic signals, resulting in figures 5.23 and 5.24 respectively. In order to have a representative behaviour of the mode we did the

average during 3 ms of the reflectometry spectrogram (corresponding to 12 PSDs), and over the same interval for each coil.

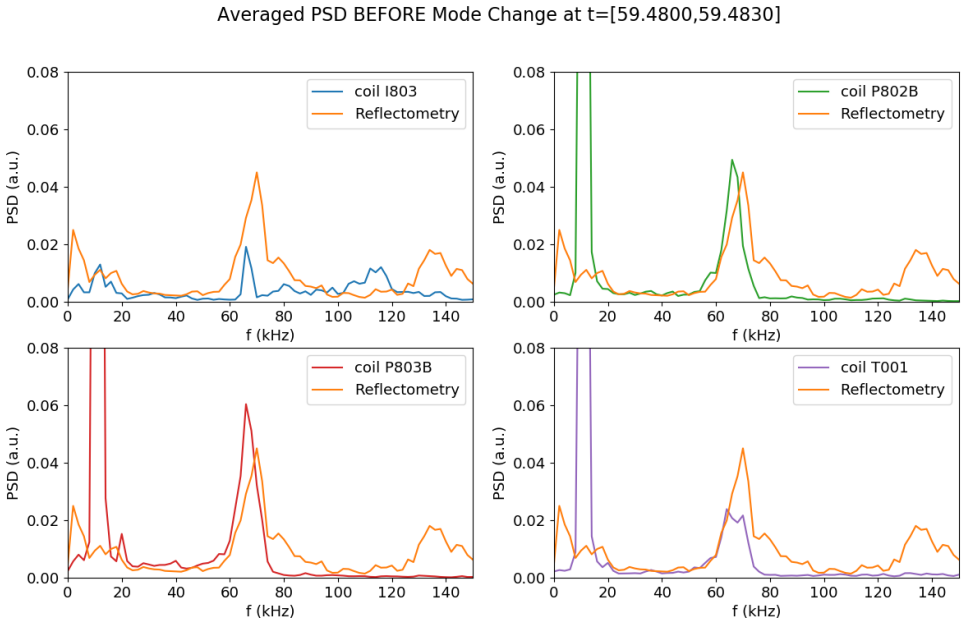

Figure 5.23: Averaged PSD of 1 HFS coil (I803) and 3 LFS coils (P802B, P803B, T001) compared to reflectometry's master channel for discharge 84733, during the coeherent phase of the mode.

In figure 5.23 the mode that seems to exist in I803, at 65 kHz, is not relevant because it exists throughout the discharge with the same frequency and intensity, being probably noise. In the LFS coils, a mode at 65 kHz is visible like the one in the CR but with a frequency shift of the mode by about 5 kHz to smaller values. The reasoning behind this shift could be explained by the fact that the mode is not localised to a single plasma layer but is instead distributed across the plasma over a radius range. Considering the magnetic perturbations decay with 1/R we could assume the outer layers of the mode to be most responsible for the magnetic mode identified in the coils. If the plasma rotation velocity for these layers is smaller than the layer identified by the CR, that would result in the mode being identified at a lower frequency, explaining the shift. The figure 5.24 shows how the mode becomes much broader in frequency for both magnetic and CR signals right after the phase change.

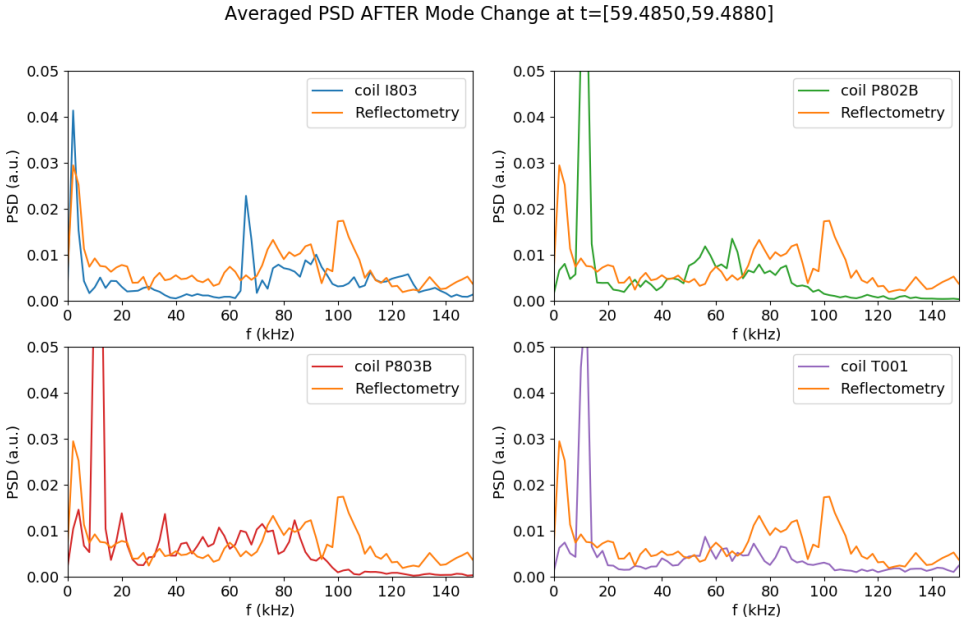

Figure 5.24: Averaged PSD of coils and reflectometry for discharge 84733, during the broadband phase of the mode.

Similar to the discharges 86469 and 86470, in the reflectometry's spectrogram of this discharge the mode near 15 kHz associated with sawteeth was also present. An example of this mode is presented in figure 5.19 d) at t=[59.464,59.475] s. In the mode evolution of [5,50] kHz frequency range, a mode around 10 kHz is very intense and well defined just before the sawtooth event at t=59.475 s, signaled by the core temperature, Te_{88}. It also exists in the magnetic signals, more in the LFS than HFS, throughout the discharge with mode harmonics when the mode is strongest and with a loss in intensity after the sawtooth event.

Density fluctuations in multiple layers

The evolution of the mode intensity in discharges 86469 and 86470 is difficult to correlate with that of the different parameters because of the observed layer varying every 25 ms. In spite of that, it is useful to analyse the mode evolution in different regions of the plasma. After looking in the magnetic coils of both discharges, no signs were found of any magnetic fluctuations that can be associated with the mode. Unlike the #84733, the D_α oscillations are always present throughout the discharges and may be the cause of these magnetic fluctuations not being found.

A concern we had with the #84733 was that after an ELM crash caused the densities to decrease temporarily, it resulted in a change of the CR probing position from near the pedestal top to closer to the core plasma. This meant we couldn't know for sure if when the mode disappeared after an ELM was due to the observed plasma layer changing or if it was correlated with the density/temperature gradients decreasing. For these discharges, this is not a worrying problem since the master channel covers more than just the top of the pedestal. This is shown in the density profiles of periods where ELMs occur, in figures 5.25a and 5.25b, for discharges 86469 and 86470 respectively. The locations where the PFs (1-8)

are probing are plotted and they cover the steep gradient region, the top of the pedestal and part of the inner plasma. Although the worry of the PF changing position remains for the PFs near the pedestal top (like 6, 7 and 8), the rest of the PFs are positioned in a region less prone to change making them more interesting to analyse for mode behaviour after an ELM crash.

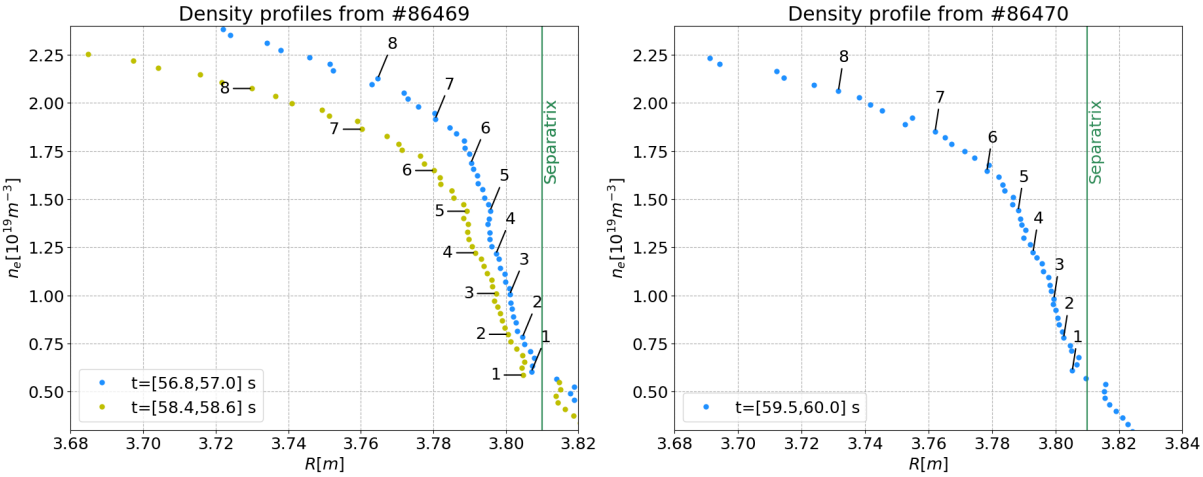

(a) Density profiles from #86469.

(b) Density profile of #86470.

Figure 5.25: Density profiles for #86469 and #86470 when ELMs occur and the position of the PFs used by the CR.

For the #86469, by looking at figure 5.26a we see some examples of the mode disappearing after some ELM crashes. The ELM at t=56.86 s occurs when the CR is using the PF 3, whose probing position shouldn't move much, yet, we observe the mode intensity dropping right after the event and behaving similarly to the edge density. It increases gradually until t=56.89 s and then both the intensity and edge density drop and recover again until the next ELM. The following ELM at t=56.902 s, also has the mode disappearing momentarily until the recovery of the edge density, which seems deeply correlated with the mode intensity until the next ELM. Other examples are presented in figure 5.27 of the next section, at t=58.45 s we see another mode losing intensity after an ELM, when the CR is operating in the PF 3. This recovery is more loosely correlated with the edge temperature Te_{38}. In the interval t=[58.67,58.74] we have recoveries of the mode intensity after 3 ELMs with the CR probing in the PFs 4, 5 and 6 and they seem to loosely follow the edge density once again. In the #86470 in the few ELMs observed, the mode also disappeared for PFs with somewhat fixed position. Namely in figure 5.26b after the ELM at t=59.285 s with the CR using the PF 4, we see the mode disappearing and recovering along with the edge density. In figure 5.32 of the next section, at t=[59.66,59.702] we see the mode lose intensity and disappear after the ELM, the mode recovery seems to follow more the edge temperature, Te_{38}, rather than density. These observations of the mode behaviour when the CR is probing in the steep density gradient region indicate that the mode existence depends in fact on the density and temperature gradients. Overall the mode recovery seems to be more correlated with the edge density, with a few cases where it evolved similarly with edge temperature. Another comment about the mode worth remarking is about being usually contained within the used PFs 1-8. So we can point to which PF the mode starts and in which it ends. This means that we can locate the ELM for most of the discharge and by looking at

the mode intensities we can usually distinguish which PF has the overall strongest intensity, suggesting we can localise the mode structure since the strength of the mode fades out as we probe farther away from this PF of higher intensity.

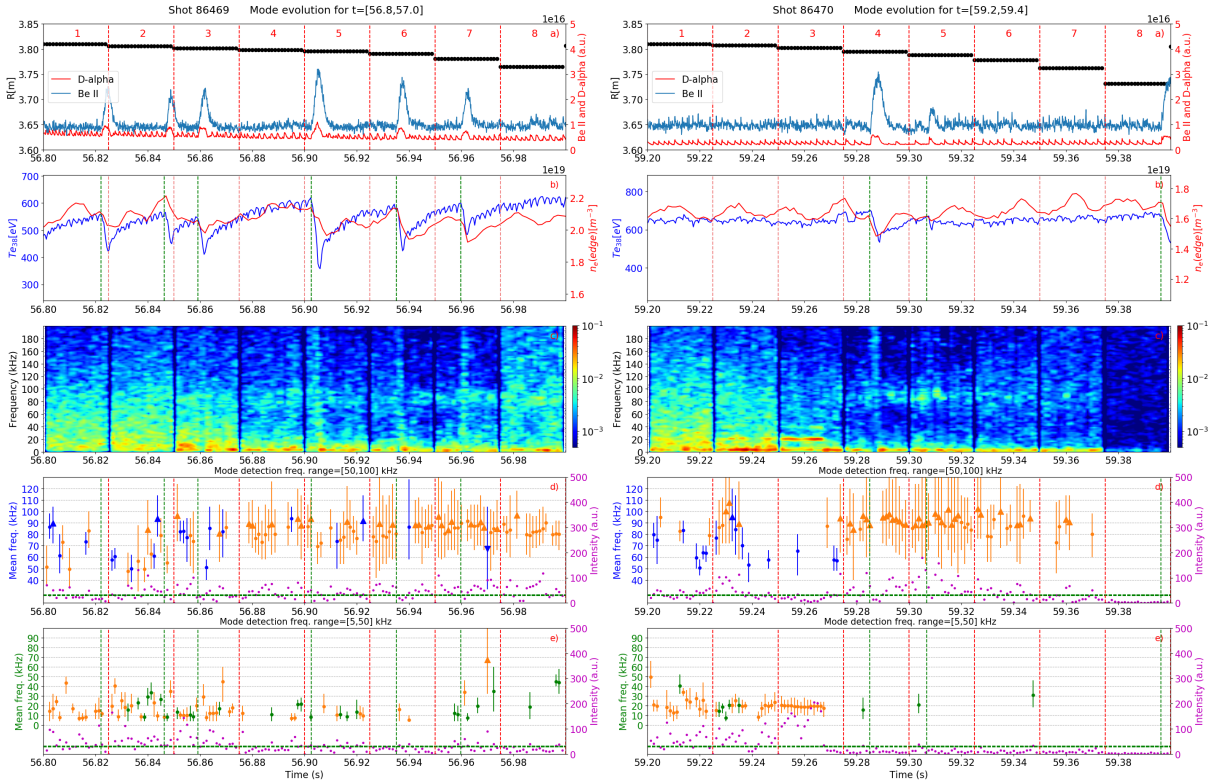

(a) #86469 (b) #86470

Figure 5.26: Mode evolution between ELMs in #86469 and #86470.

An important aspect about the mode that also needs comparison between the different PFs is its frequency. Along the two discharges, whenever the mode is present in certain PFs, its frequency usually fluctuates around the same frequency window of around 20 kHz. The fact the mode frequency is somewhat inconsistent may be mainly due to the mode being wide and behaving irregularly along the discharges accompanied with the fact that the D_α oscillations disrupt the signal constantly. Adding to this is the implemented way of obtaining the baseline, that may fail occasionally by either underestimating or overestimating the baseline, which affects in determining the mode width and, consequently, the calculated frequency. By visually comparing the mode in different PFs, there are no big differences between the mode frequencies and their width, seeming overall consistent with each other, despite that, in the next section a better comparison will be done between the frequencies of the different PFs.

5.3 Characterization of measured fluctuations at different radial positions and determination of the radial profile of the mode between ELMs

The reflectometry configuration of the master channel in the discharges 86469 and 86470 permitted to follow different density layers (near the pedestal) in time intervals of 0.2 s. The spectrogram of these reflectometry's signals indicate that the mode at 70-100 kHz, mentioned in the previous chapter, is, as mentioned before, more defined in some probing frequencies than others. This indicates that the mode is not homogeneous and varies along the radius of the tokamak, making it of interest to obtain a profile of its localisation based on intensity and frequency. To do so, we must choose an interval in which ELMs occur so we can locate this mode during the ELM cycle. Mode localisation and intensity vary along the discharge due to many factors such as D_α oscillations, changes in the P_{NBI}, ELM events, among others. One concerning factor are changes in the n_e profile that vary the probed locations and may be problematic if they occur along a PF. So it is important to choose consecutive intervals where there are no noticeable variations of the density profile. This way, for each PF we avoid varying the scanned layer during the chosen intervals for the radial profile of the mode. The sensibility to choose intervals was that the edge density should not vary more than around 10% along that period. It was also considered that the mode has a recovery time after each ELM which was critical to ignore. To implement this consideration for the ELMs and others, a method was developed for this collection of times used for the mode localisation.

We defined this algorithm respecting the following conditions:

- An interval, in which a set of ELMs are present, is chosen for the automated selection of points between the ELMs. In this period the mode location must not visibly vary between PFs.
- A time is defined after the ELM in which there is a recovery of plasma quantities, so the points in these intervals are not considered. The recovery time is obtained by first determining the periods between the ELMs of the chosen set, followed by an average over them. With the obtained mean ELM cycle period, we chose to define the recovery time as 25% of it. Ideally, this percentage would be 40-50%. However, because of the change in PF every 25 ms, following this ideal percentage would result in poor statistics to locate the mode.
- Data just before an ELM is always ignored because by being close to the event, it could be influenced, for instance, by ELM precursors.
- As noticed before, whenever the sawtooth mode is present, it affects the intensity of the mode of interest. Consequently, the data near each sawtooth crash with a visible strong sawtooth mode is ignored.

Following these conditions allows the choice of intervals for the construction of the mode localisation, an example of this algorithm's selection is shown in figure 5.27, where the selected points are shown by

the horizontal black arrows. Our objective is to know for each PF used, what is the average intensity and average frequency of the mode using the selected points. To do so we want to gather these mode characteristics based on the corresponding PF of each point from the full sweeps of the selected data. Building 8 groups that have the mode intensities and frequencies of a specific PF. With all the available points for each PF, we calculate an average of the mode intensity and frequency as well as a standard deviation, so we can understand how consistent are the determined quantities. Then we want to associate a corresponding radius with each PF, which can be done by assuming that the PFs do not vary position in the chosen intervals. So we select the n_e profile, provided by the fast sweep reflectometry, that is closest to the chosen interval and extract the positions of the PFs used. This way we can build a radial distribution for the mode intensity and frequency.

5.3.1 Discharge 86469

Taking into consideration the conditions mentioned before, the ELMs were analysed and some selected to build the radial profile of the mode. Namely, the ELMs in the interval t=[58.4,58.8] s presented in figure 5.27. The points chosen by the algorithm are marked with the horizontal black arrows.

By looking at the spectrogram and the identified modes we notice its location to be between the PFs 3 and 6. The PFs 1 and 2, which are closer to the separatrix, show a lot of turbulence with intense fluctuations up to 140 kHz. On the contrary, the PFs 7 and 8 show few activity as they probe more inside the plasma, away from edge turbulence.

The mode frequency along the PFs where it exists seems to be similar and around 70-85 kHz. However, for the PF 1 and 2, at t=[58.612,58.65], a mode seems to be identified. After checking the evolution of the PSD in this interval, they were identified as random fluctuations of high intensity that are caught by the mode detection algorithm. By generally looking at the mode intensity, it seems to be stronger for the PF 4 and fades out until it does not exist for the PF 2 and 7.

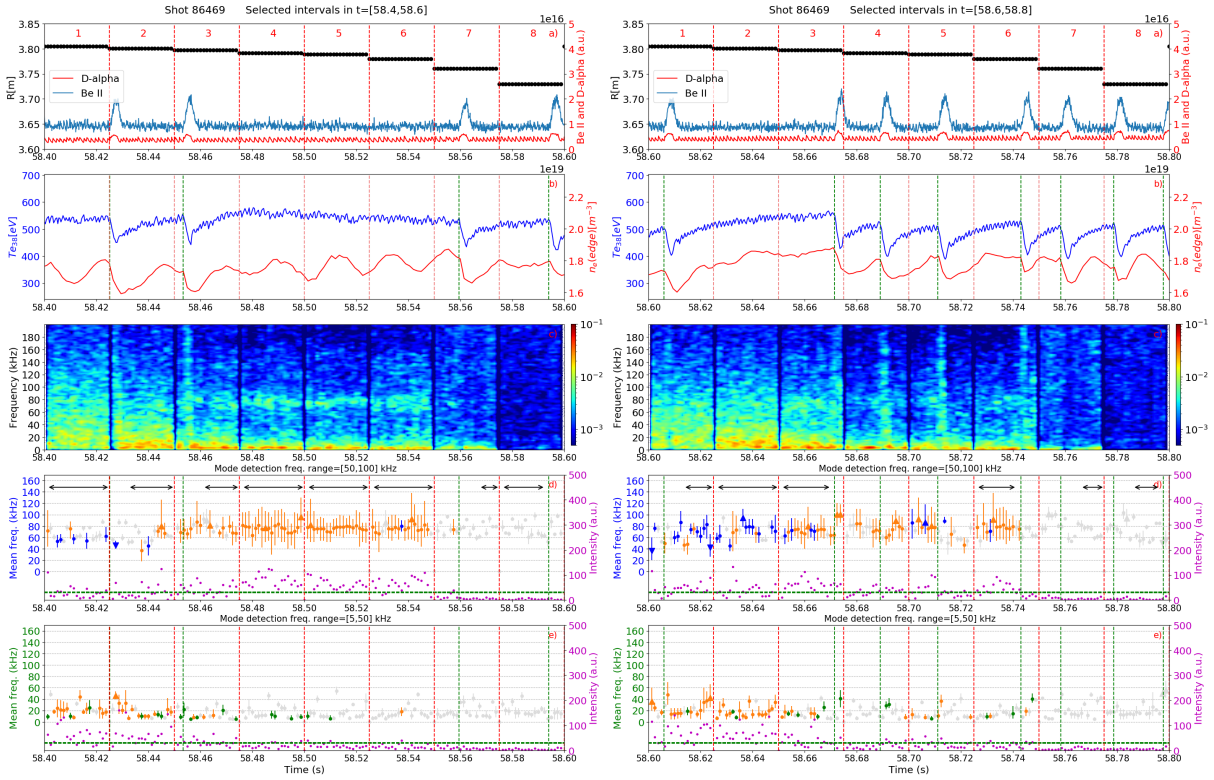

Figure 5.27: Mode evolution with black arrows that signal the points chosen for mode localization in each probing frequency of discharge 86469

With the chosen intervals, the mode localisation was done and presented in figure 5.28. In plot a), mode intensity is presented along the radius with the number of the associated PF; in plot b), the mode frequency is shown as well as the corresponding number of used points by each PF; in plot c), a density profile is presented and in plot d) are the corresponding PFs (used by the fast sweep reflectometer to determine each density). Like mentioned before, this profile was needed to locate the PFs used by the CR along a full sweep, which are annotated from 1-8 in both profiles. From the many profiles taken along the discharge, only one was used since we had already selected a period where the edge line-averaged density wouldn't vary significantly, implying the density profile would also stay relatively the same. The selection of this profile was based on its proximity to the chosen interval. The probing frequencies cover the steep density gradient region, the top of the pedestal as well as a region a few cms inside the top of the pedestal.

The intensities of the modes clearly indicate that it is localised between the PFs 3-6, around the pedestal top and extending up to the middle of the steep density gradient region. It is located between R=3.78-3.798 m being strongest for the PF 4 at R=3.79 m. Even though the probing frequencies 1 and 2 have intensities above the considered threshold value, the mode detected has high variance in both intensity and frequency. This is expected since, like examined before, the PSDs along these two PFs show that the identified modes are in fact random fluctuations of high amplitude. High enough that are picked up by the mode detection algorithm. These random fluctuations explain the variance being so high in frequency, since there is no consistent mode being detected, varying wildly along time.

In the PFs 3-6, where the mode existed, the mean frequency shows a slight decrease as the radius

increases. The mode is identified with 77.6 kHz at the top of the pedestal (PF 6) and continuously goes down to 72.2 kHz at the middle of the steep gradient region (PF 3). The frequency difference between these two PFs is 5.4 kHz. An indicative mode frequency was calculated based on a weighted average frequency over the 3 most intense PFs of the mode, the weights being the corresponding mode intensities. The result is $\overline{f} = 76$ kHz.

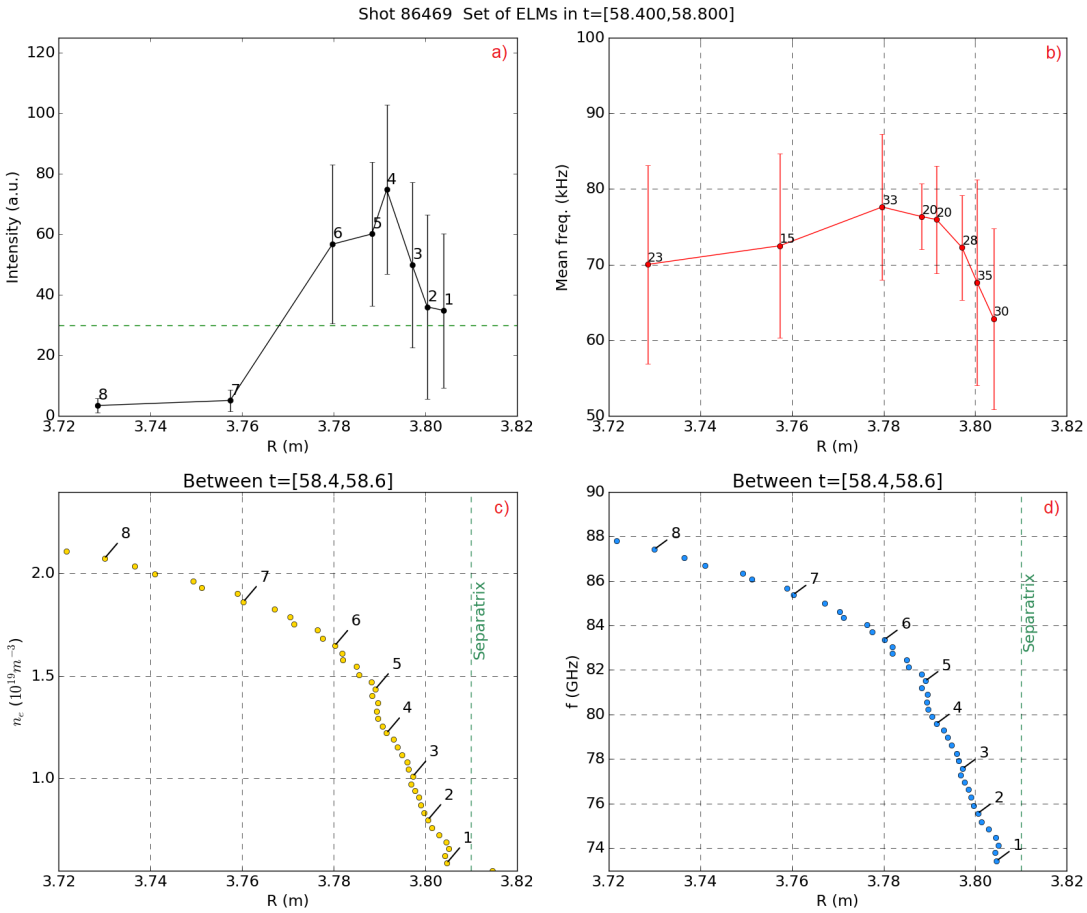

Figure 5.28: Profile of the mode obtained from the detection frequency range 50-100 kHz, in t=[58.4,58.8] s of #86469. a) Intensity of the mode along the radius (the green dashed line is the intensity threshold of a mode); b) frequency weighted by the PSD for the mode along the radius; c) average electron density profile of LFS; and d) radial profile of the PF.

First appearance of the mode

We tried to localise the mode between the first ELMs around t=[56.8,57.2] s. What was interesting in this period is the appearance of the mode for the first time in the discharge. Also, the mode moves between PFs while the edge density profile is varying giving us an opportunity to characterise the mode evolution while it is changing. To do so we subdivided the interval into two periods, so we could locate the mode using different density profiles, each period corresponds to a full sweep over 8 PFs.

The first full sweep is at t=[56.8,57] s, presented in figure 5.29a. This period is when the mode is visible for the first time in CR. The algorithm that determines the usable points was applied and because it is full of ELMs we have somewhat poor statistics for this period, specially for PF 3. The mode is not present in all the PFs, specifically the PFs 1, 2 and 3, even though these probed regions seem to have

noticeable turbulence in their spectrograms. The mode is identified in the PFs 4-8 and the frequency of the mode in these seems to be similar.

The second period starts where the previous ended and another full sweep over the PFs is done at t=[57,57.2], presented in figure 5.29b. The statistics are a bit better with less ELMs but similar to the previous period. The mode is more intense for the PFs 3-6, with the PFs 1 and 2 having a lot of intense turbulence, turbulence so intense that is identified as a mode by the algorithm. The PF 7 seems to have the mode momentarily while in the period of recovery from the ELMs, yet overall both PFs 7 and 8 do not have the mode.

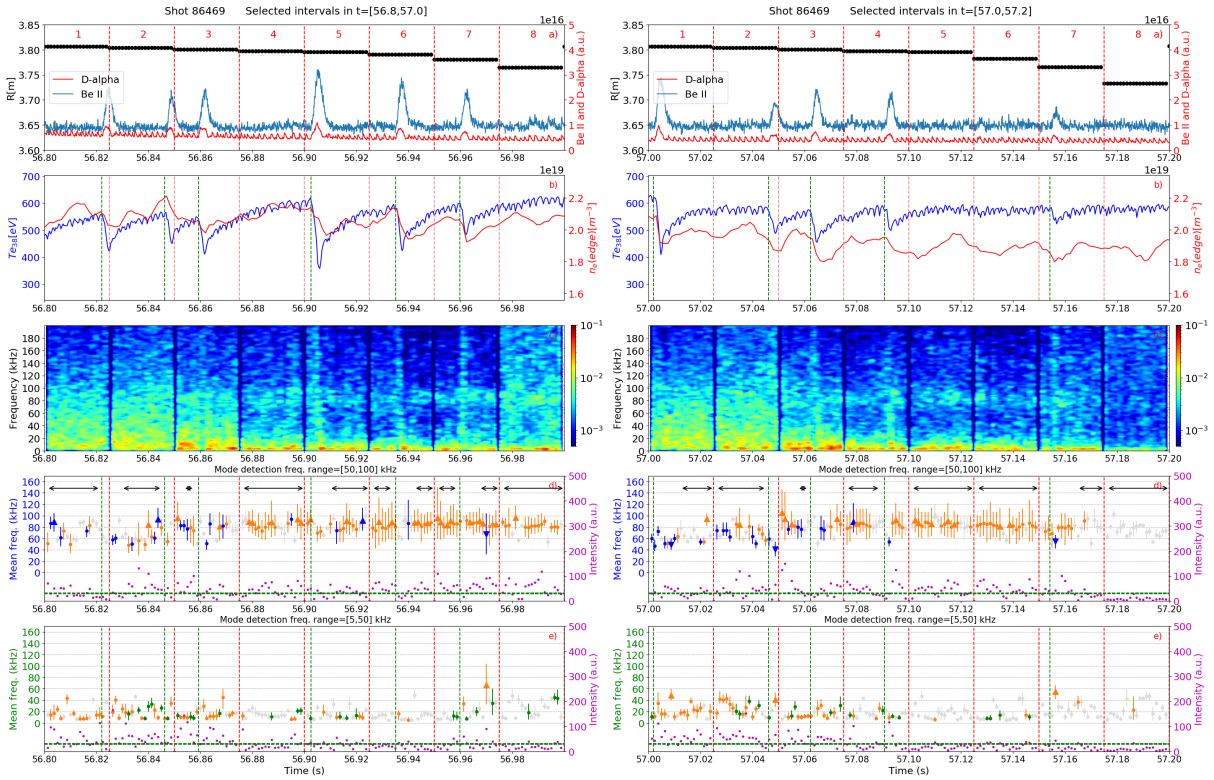

(a) First PFs full sweep

(b) Second PFs full sweep

Figure 5.29: Mode evolution with black arrows that signal the points chosen for mode localization in each probing frequency of discharge 86469

Using the selected times from the first full sweep in figure 5.29a, the mode frequency and intensity can be determined for each PF resulting in figure 5.30. The mode is localised and better defined at R=3.78 m (PF 7) and extends to R=3.762-3.799 m. The peak at the PFs 1-3 is artificial due to turbulence. The frequency of the mode is similar along the radius around 84-85 kHz for the PFs 4-7 and slightly less for PF 8 at 83 kHz.

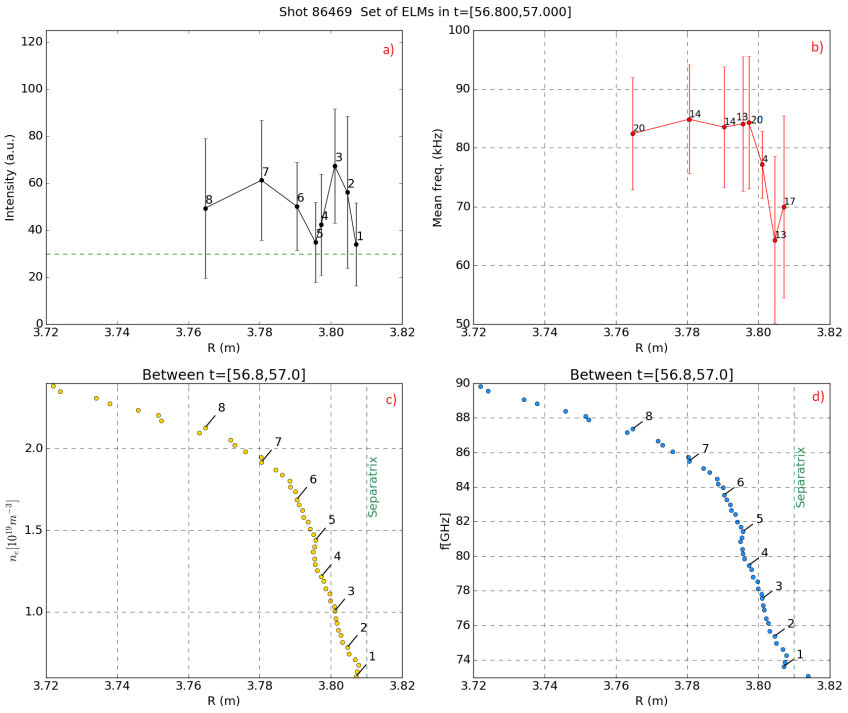

Figure 5.30: Profile of the mode obtained from the detection frequency range 50-100 kHz, in t=[56.8,57] s of #86469

With the selected times of the second full sweep in figure 5.29b, once again the mode characterisation along the PFs was obtained resulting in figure 5.31. For this sweep because the edge density drops along the discharge, another density profile, t=[57.25,57.5] s, was used to locate the PFs. This was the closest density profile we had to the selected period. However, it is of an interval with lower edge density compared to the used interval of t=[57,57.2] s. This means the density profile is underestimated and the radii of the PFs may be identified as smaller than they are supposed to be. The ideal density profile would be an intermediate profile between the previously used (t=[56.8,57] s) and this one. The mode intensity indicates that the mode is located at R=3.78-3.8 m, however taking into consideration that the density profile should be steeper, these radii would shift slightly to higher radius. The frequencies of the mode are not as similar as in figure 5.30 b). For this sweep, the frequency peaks at 86 kHz, for the PF 5, and then drops in frequency for the PFs 4 and 6. Although the statistics are not the best, this behaviour could reflect the rotation velocity profile, with the rotation velocity being highest for the density layer at R=3.79 m (PF 5), and going down for the PFs 4 and 5.

By comparing the figures 5.30 and 5.31, the location of the mode clearly shifts position from the top of the pedestal to the steep gradient region as the density profile drops, the latter location of the mode is in agreement with the one identified for the interval t=[58.4,58.6] s of figure 5.28.

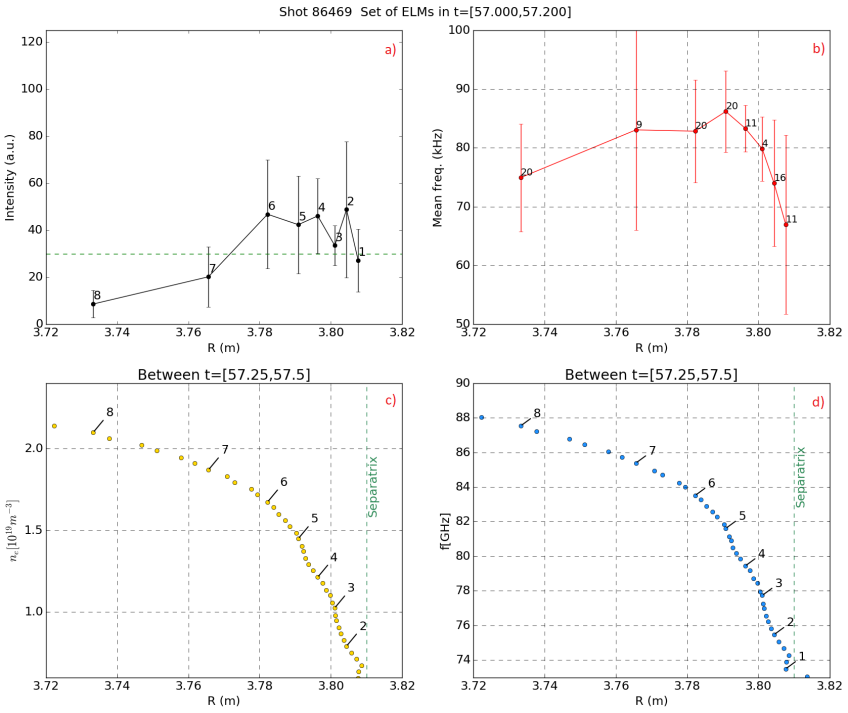

Figure 5.31: Profile of the mode obtained from the detection frequency range 50-100 kHz, in t=[57,57.2] s of #86469

5.3.2 Discharge 86470

Similar to the previous discharge, from all the ELMs in the discharge 86470, some were selected for the mode localisation. Specifically the ones in t=[59.6,60.2] s, which are presented in figure 5.32, from this chosen interval only the points indicated by the horizontal black arrows were used. From the selected intervals, the ignored time after certain ELMs seems to be satisfied, as well as not using periods where the sawtooth mode is really intense, like at t=[59.85,59.91] s and t=[60.125,60.174] s.

Analysing the various frequency sweeps we can notice a mode which is more wide spread than the one found in the previous discharge. It seems to be located somewhat between the PFs 3 and 7. The PFs 1 and 2 behaving similarly to the previous discharges with a lot of turbulence and the PF 8 showing almost no activity.

The mode of interest seems to oscillate in the same frequency range of 70-100 kHz for the PFs 3-7 and the intensity of the mode seems to be strongest for the PF 5.

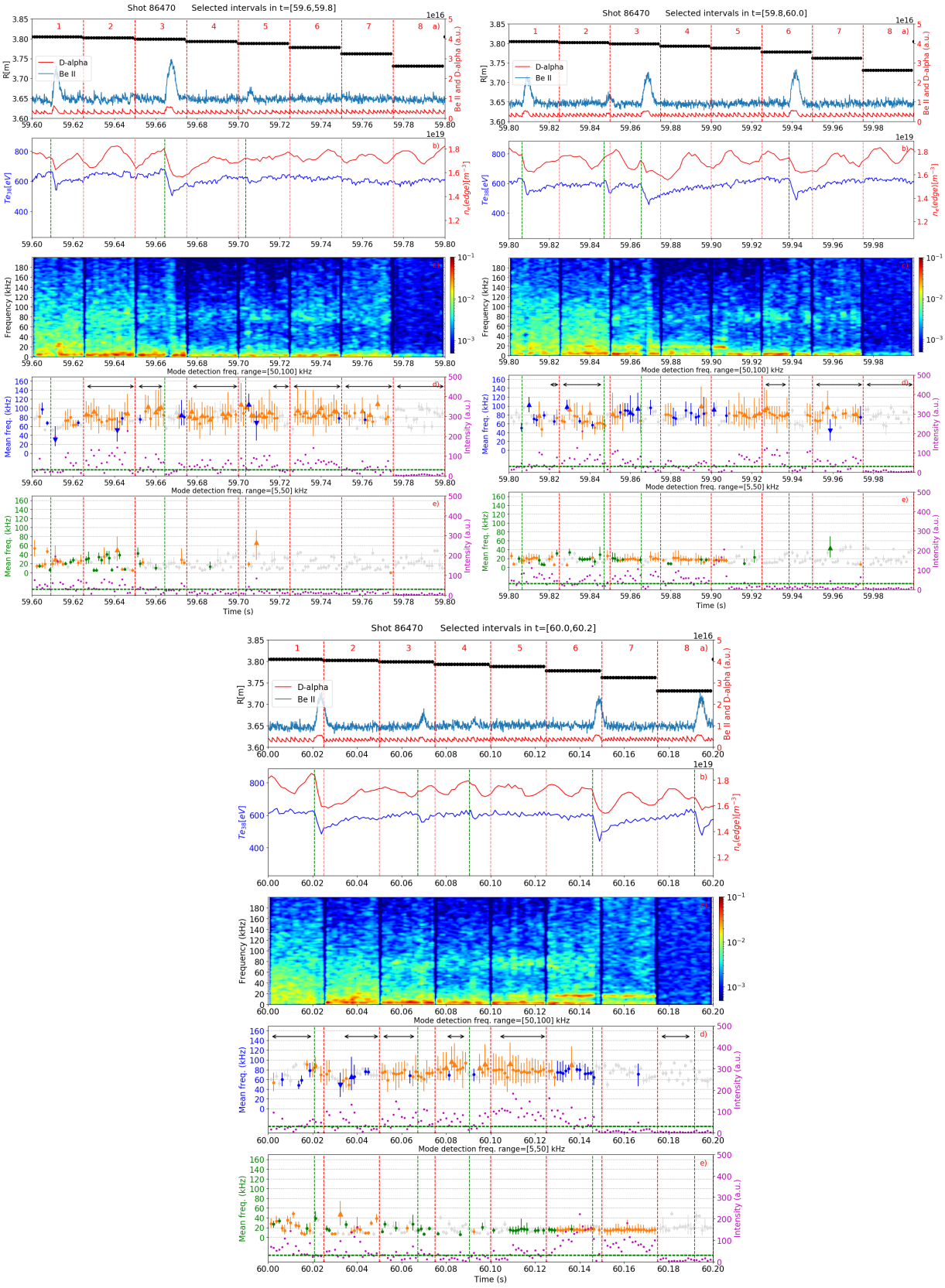

Figure 5.32: Mode evolution with black arrows that signal the points chosen for mode localization in each probing frequency in discharge 86470

The resulting mode localisation using the selected intervals is presented in figure 5.33. The probing

frequencies cover the similar regions as the previous discharge. By looking at the plot a) of the mode intensity profile, the mode location is not as obvious for this discharge.

We have two peaks along the radius, the main peak at the PFs 6 and 5 and a second peak in the PFs 2 and 3 with the 4^{th} having a lower intensity. The second peak at the PF 2 can be considered artificial since this PF has high variance in both intensity and frequency, also the mode frequency departs from the frequencies of the most intense PFs by around 10 kHz. This indicates that the mode identified in the PFs 1 and 2 might not be the coherent mode found in the PFs 3-7 but instead are the set of intense random fluctuations detected by the mode detection algorithm, like in the previous discharge. The intensity at the PF 4 should be at least bigger than the PF 3, assuming that there is only one mode localised around the PF 5 that decays as it goes further away from this PF. However, the intensity in PF 4 is lower than expected, which can be justified by the evolution along the ELM cycle. In this case the ignored time after the ELMs may not be sufficient, leading to some points where the plasma quantities are still recovering to be used. This results in an underestimation of intensity for this PF. Taking all the above into consideration, we can locate the mode around the PFs 3-7, with the PF 7 showing the mode very faintly. We can locate the mode strongly at the PF 5 at R=3.788 m, near the top of the pedestal, and is distributed across R=3.762-3.8 m, that covers the pedestal top and reaches up to the middle of the steep density gradient region.

The mean frequency profile of this discharge also shows a decreasing tendency from the top of the pedestal (PF 6) to the middle of the steep gradient region (PF 3). Although the PF 5 seems to be an outlier, its variance covers a frequency in which the trend would uphold. The mode is identified with 85.3 kHz for PF 6 and down to 80 kHz at the PF 3. Similar to the previous discharge, the difference of the mode frequency between the most distant layers where it was identified more strongly is 5.3 kHz. This frequency difference being about 5 kHz for both discharges corroborates the explanation given for the observed frequency shift between the CR and the magnetic coils of figure 5.23. In the discharge #84733, the CR was probing a density layer at the pedestal top, identifying a mode with increased frequency. While the measured fluctuations in the magnetic coils, which were caused mainly by the outer layers, have the same mode at a smaller frequency with a 5 kHz shift.

The same indicative calculation of a weighted average frequency was done for this mode with the 3 most intense PFs, ignoring the PF 2 due to the reasons mentioned before. From this calculation we have that the mode has $\overline{f} = 81$ kHz.

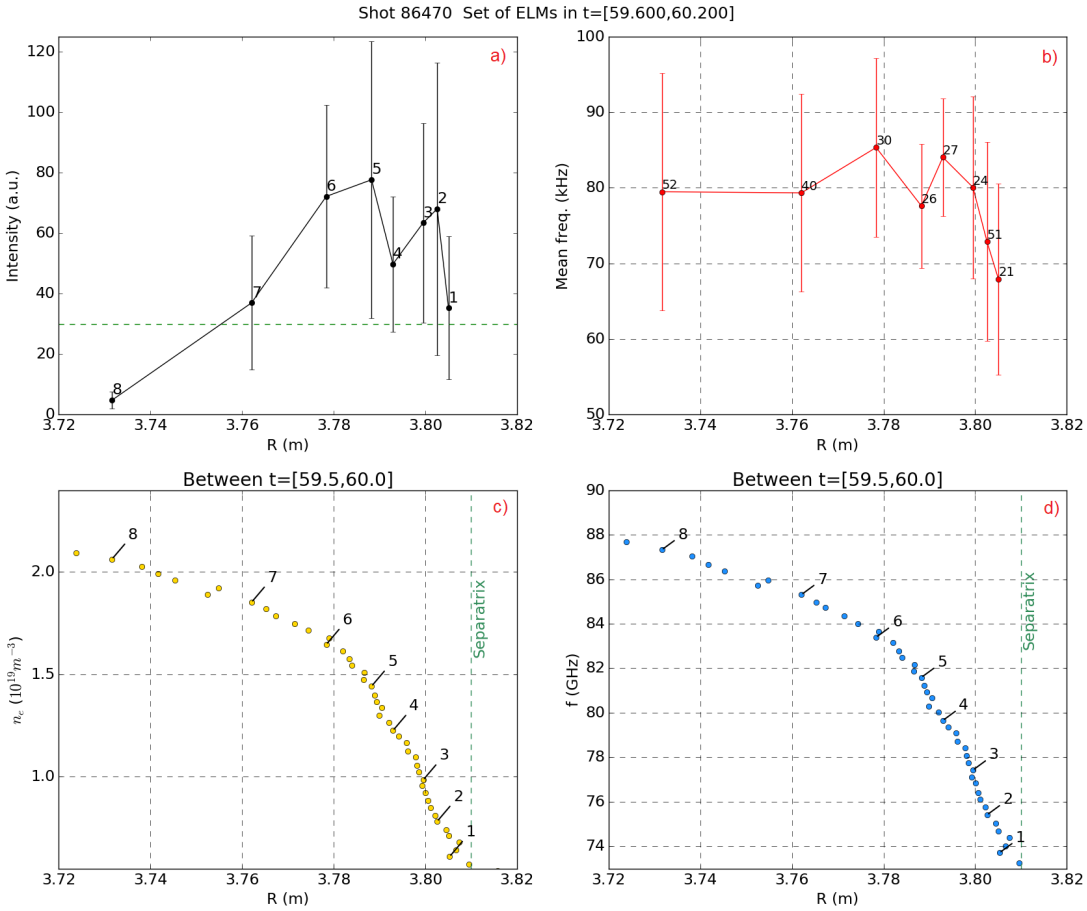

Figure 5.33: Profile of the mode obtained from the detection frequency range 50-100 kHz, in t=[59.6,60.2] s of #86470

By comparing the resulting mode frequencies from these two discharges, the #86469 at $\overline{f} = 76$ kHz and the the #86470 at $\overline{f} = 81$ kHz. These are very similar frequencies which indicate that it is the same mode. The frequency discrepancy between them can be justified by the difference in the P_{NBI} being used in the selected points. The average heating power supplied during the chosen intervals for the #86469 was of $\overline{P}_{NBI} = 7.5$ MW, while for the #86470 was higher at $\overline{P}_{NBI} = 8.3$ MW. The increased heating power in the latter may have caused the plasma layer where the mode existed to rotate faster appearing at a higher frequency. In terms of mode location they are consistent between discharges with the mode being at R=3.78-3.798 m for #86469 and at R=3.762-3.8 m for the #86470, with the maximum of the mode intensity being concordant at R=3.788 m and R=3.79 m, respectively.

Chapter 6

Concluding remarks

With this work we intended to understand better the instabilities at the edge plasma called Edge Localised Modes, that emerge when the plasma reaches an improved confinement mode. These events crash the plasma and inhibit the improvement of fusion conditions, making it crucial to determine their origin in order to help advance nuclear fusion towards commercial availability. The objective for this thesis was to make an analysis of an instability at the edge of the plasma that seemed to be correlated with ELM events. The mode had a frequency range of [60-90] kHz and was detected and monitored in three discharges using correlation reflectometry. We were able to relate its intensity with the recovery of edge density after the ELM. We also determined the mode position between ELMs by varying the probing frequency of the reflectometer in a pre determined pattern, which allowed to scan multiple density layers of the plasma.

Many tools were developed to facilitate the analysis of the different discharges. We constructed ELM detection algorithms that signaled their start, allowing for an easier tracking of mode and plasma parameters. We also detected sawtooth events because of their impact on the temperature profile and on the mode intensity. We constructed a modified Welch method that improved the mode amplitude estimation with a temporal resolution that allows to follow the ELM cycle. Upon analysing the resultant spectrograms from this method we noticed a varying background component with an amplitude decaying with frequency as $1/f^2$. Its shape changed along the different probing frequencies and made it difficult to compare the mode intensity between them, so we implemented a way to determine and subtract this baseline component to each individual power spectrum. We also defined frequency ranges where the modes typically exist to help track and characterise them by intensity, frequency and frequency width. Using the density profiles from the fast sweep reflectometry, we were able to localise each PF along time and consequently locate the mode. Some of the density profiles had to be modified to rectify an artificial shift in radius added by the evaluation of the average profile. Finally, with the selected intervals between ELMs, a set of criteria was defined to collect data for each PF in order to perform the radial localisation of the mode.

Using these tools, many observations and results are worth remarking. It was possible to observe the evolution in electron density profiles when changing from a low to high confinement mode.

An intermittent behaviour of the mode was observed in the correlation reflectometry signal for the different discharges and was attributed to low frequency oscillations. These are visible in the D_α and reduce the overall activity in the power spectrum. We noted that the mode of interest had a magnetic nature, appearing whenever these ocillations would vanish. In these intervals of low D_α activity, we compared the modes observed in the magnetic and reflectometry signals and a frequency shift of the mode by about 5 kHz to smaller values was detected in the magnetic mode. This could be justified by the mode being distributed across the edge plasma with the two diagnostics probing different regions. As the plasma rotation is expected to change with radius, this would explain the observed shift. The mode was only visible in the magnetic signals of the low field side, indicating a ballooning structure. The magnetic nature of the mode did not reveal itself in two of the analysed discharges because the heating supplied did not evolve much beyond the L-H transition, so the low frequency oscillations were always present and did not allow the mode to manifest.

The mode intensity variation in the discharge 84733 for periods with low density was discovered to be caused by the position of the correlation reflectometer. By probing at the top of the steep gradient region when the densities were higher, whenever these densities would drop, the region being probed changed to more inside the plasma, a region where the mode did not exist. After each ELM we suspect this change in scanning region also happened justifying the correlation found between the mode intensity and edge density. However, this correlation after the ELM is also present in the discharges 86469 and 86470 for probing frequencies in the steep gradient region. These do not vary position as much after the densities drop, yet, the correlation persists. This may indicate the mode intensity is in fact correlated with the density gradient. The temperature at the top of the pedestal usually recovered much faster that the n_e and mode intensity, although there were some cases where the temperature was more correlated to the mode intensity than the n_e.

A particular behaviour that is worth noticing is that mode frequency seems to vary with the heating power of neutral beam injection, P_{NBI}, along the discharges. An increase or decrease in heating power results in the modes of both reflectometry and magnetic coils to respectively increase or decrease in frequency. This dependence of the mode frequency on the heating power is because an increase in P_{NBI} causes a higher rotation of the plasma. This translates to the layer where the mode exists to rotate faster, increasing the mode frequency.

In all discharges, another mode was identified around 10-20 kHz both in the reflectometry and magnetic signals associated with sawtooth events. This mode, when strongest in the reflectometry signal, affected the intensity of the mode of interest by reducing its intensity. This phenomenon could be justified by a magnetic instability associated with sawteeth that interferes with the main mode but further studies are needed.

Along the discharges 86469 and 86470 the main mode was observed in the steep gradient region around R=3.78-3.80 m. We were able to successfully localise the mode using the developed algorithm that determined its intensity and frequency along the radius. The mode was identified to have a frequency of $\overline{f} = 76$ kHz, and located at R=3.78-3.798 m for the discharge 86469. For the discharge 86470 a similar mode was determined with $\overline{f} = 81$ kHz and located at R=3.762-3.8 m. The frequency profile obtained

from these radial discharges helped understand the frequency shift of the main mode observed between the CR and the magnetic coils for the #84733.

In summary, with this work we were able to describe the mode evolution probing a single layer of the plasma as well as show how hopping reflectometry can help determine the localisation of a mode along the radius. In future work, radial location of the mode in periods without ELMs could be explored complemented with more density profiles. This way we could correlate the mode intensity with the steepness of the density gradient at different points of the discharge. The density profiles could also be explored with more detail using a mtanh fit that would help identify with more precision the pedestal width and height, and use these to compare to the EPED model. Also, a further analysis using the phase and the amplitude separated could be done to check if the observations done with the complex signal I+jQ translate to each of these quantities.

Bibliography

[1] EIA, *Independent statistics and analysis*, URL https://www.eia.gov/outlooks/ieo/, 2019.

[2] BP, *BP statistical review of world energy*, 2019.

[3] IPCC, *Summary for policymakers*, URL https://www.ipcc.ch/sr15/chapter/spm/, 2018.

[4] *If carbon dioxide hits a new high every year, why isn't every year hotter than the last?: Noaa climate.gov*, URL https://www.climate.gov/news-features/climate-qa/if-carbon-dioxide-hits-new-high-every-year-why-isn\OT1\textquoterightt-every-year-hotter-last, Sep. 2019.

[5] K. Thoubboron, *Advantages and disadvantages of renewable energy: Energysage*, URL https://news.energysage.com/advantages-and-disadvantages-of-renewable-energy/, Oct. 2019.

[6] J. P. Freidberg, *Plasma physics and fusion energy*. Cambridge University Press, 2010.

[7] S. Li, H. Jiang, Z. Ren, and C. Xu, "Optimal tracking for a divergent-type parabolic pde system in current profile control," *Abstract and Applied Analysis*, vol. 2014, pp. 1–8, 2014. DOI: 10.1155/2014/940965.

[8] ITER, *Advantages of fusion*, URL https://www.iter.org/sci/Fusion, 2020.

[9] Fusenet, *Iter*, URL https://www.fusenet.eu/node/39.

[10] M. Shimada, D. Campbell, V. Mukhovatov, M. Fujiwara, N. Kirneva, K. Lackner, M. Nagami, V. Pustovitov, N. Uckan, J. Wesley, N. Asakura, A. Costley, A. Donné, E. Doyle, A. Fasoli, C. Gormezano, Y. Gribov, O. Gruber, T. Hender, W. Houlberg, S. Ide, Y. Kamada, A. Leonard, B. Lipschultz, A. Loarte, K. Miyamoto, V. Mukhovatov, T. Osborne, A. Polevoi, and A. Sips, "Chapter 1: Overview and summary," *Nuclear Fusion*, vol. 47, no. 6, S1–S17, Jun. 2007. DOI: 10.1088/0029-5515/47/6/s01. [Online]. Available: https://doi.org/10.1088%2F0029-5515%2F47%2F6%2Fs01.

[11] M. Kikuchi, A. Fasoli, T. Takizuka, P. Diamond, S. Medvedev, X. Duan, H. Zushi, M. Furukawa, Y. Kishimoto, Y.Wu, O. Sauter, L. Villard, S. Brunner, G. Merlo, J. Kwon, G. Zheng, K. Mishra, M. Honda, H. Urano, and F. Sano, "Negative triangularity tokamak as fusion energy system," Mar. 2014. DOI: 10.3390/ece-1-e002.

[12] M. Cavedon, "The role of the radial electric field in the development of the edge transport barrier in the asdex upgrade tokamak," Ph.D. dissertation, Technische Universität München, 2016.

[13] H. Zohm, "Edge localized modes (ELMs)," *Plasma Physics and Controlled Fusion*, vol. 38, no. 2, pp. 105–128, Feb. 1996. DOI: 10.1088/0741-3335/38/2/001.

[14] D. Hill, "A review of elms in divertor tokamaks," *Journal of Nuclear Materials*, vol. 241-243, pp. 182–198, 1997, ISSN: 0022-3115. DOI: https://doi.org/10.1016/S0022-3115(97)80039-6. [Online]. Available: http://www.sciencedirect.com/science/article/pii/S0022311597800396.

[15] A. Burckhart, E. Wolfrum, R. Fischer, K. Lackner, and H. Z. and, "Inter-ELM behaviour of the electron density and temperature pedestal in ASDEX upgrade," *Plasma Physics and Controlled Fusion*, vol. 52, no. 10, p. 105 010, Sep. 2010. DOI: 10.1088/0741-3335/52/10/105010. [Online]. Available: https://doi.org/10.1088%2F0741-3335%2F52%2F10%2F105010.

[16] F. M. Laggner, "Inter-elm pedestal structure development in asdex upgrade," Ph.D. dissertation, Technischen Universität Wien, 2017.

[17] A. F. Mink, "Structure and nonlinear development of edge localized magnetohydrodynamic instabilities on the asdex upgrade tokamak," Ph.D. dissertation, Technischen Universität Wien, 2018.

[18] P. B. Snyder, T. H. Osborne, K. H. Burrell, R. J. Groebner, A. W. Leonard, R. Nazikian, D. M. Orlov, O. Schmitz, M. R. Wade, H. R. Wilson, and et al., "The eped pedestal model and edge localized mode-suppressed regimes: Studies of quiescent h-mode and development of a model for edge localized mode suppression via resonant magnetic perturbations," *Physics of Plasmas*, vol. 19, no. 5, p. 056 115, 2012. DOI: 10.1063/1.3699623.

[19] R. J. Hastie, "Sawtooth instability in tokamak plasmas," *Astrophysics and Space Science*, vol. 256, no. 1, pp. 177–204, Mar. 1997, ISSN: 1572-946X. DOI: 10.1023/A:1001728227899. [Online]. Available: https://doi.org/10.1023/A:1001728227899.

[20] C. Woodley, *Jet: The joint european torus*, URL https://ccfe.ukaea.uk/research/joint-european-torus/, May 2019.

[21] X. L. et al, "Overview of the JET results in support to ITER," *Nuclear Fusion*, vol. 57, no. 10, p. 102 001, Jun. 2017. DOI: 10.1088/1741-4326/aa5e28. [Online]. Available: https://doi.org/10.1088%2F1741-4326%2Faa5e28.

[22] J. Mlynář, *Focus on:JET*. EFDA, 2007.

[23] E. Mazzucato, "Microwave reflectometry for magnetically confined plasmas," *Review of Scientific Instruments*, vol. 69, no. 6, pp. 2201–2217, 1998. DOI: 10.1063/1.1149121. eprint: https://doi.org/10.1063/1.1149121. [Online]. Available: https://doi.org/10.1063/1.1149121.

[24] J. A. Wesson, *Tokamaks*. Clarendon Press, 2004.

[25] J. Schirmer, "Plasma turbulence studies using correlation doppler reflectometry on the asdex upgrade tokamak," Ph.D. dissertation, 2005.

[26] A. Sirinelli, B. Alper, C. Bottereau, F. Clairet, L. Cupido, J. Fessey, C. Hogben, L. Meneses, G. Sandford, M. J. Walsh, and J.-E. Contributors, "Multiband reflectometry system for density profile measurement with high temporal resolution on jet tokamak," *Review of Scientific Instruments*, vol. 81, no. 10, p. 10D939, 2010. DOI: 10.1063/1.3502329. eprint: https://doi.org/10.1063/1.3502329. [Online]. Available: https://doi.org/10.1063/1.3502329.

[27] M. Hirsch, E. Holzhauer, J. Baldzuhn, B. Kurzan, and B. Scott, "Doppler reflectometry for the investigation of propagating density perturbations," *Plasma Physics and Controlled Fusion*, vol. 43, no. 12, pp. 1641–1660, Oct. 2001. DOI: 10.1088/0741-3335/43/12/302. [Online]. Available: https://doi.org/10.1088%2F0741-3335%2F43%2F12%2F302.

[28] C. Silva, J. Hillesheim, C. Hidalgo, E. Belonohy, E. Delabie, L. Gil, C. Maggi, L. Meneses, E. Solano, M. Tsalas, and et al., "Experimental investigation of geodesic acoustic modes on jet using doppler backscattering," *Nuclear Fusion*, vol. 56, no. 10, p. 106 026, 2016. DOI: 10.1088/0029-5515/56/10/106026.

[29] S. A. et al, *11th Int.Reflectometry Workshop (Paris)*, Apr. 2013.

[30] M. Nave, B. Alper, D. Borba, C. Boswell, C. Challis, M. Brix, S. Gerasimov, S. Hacquin, N. Hawkes, E. Joffrin, J. Mailloux, E. de la Luna, and P. Smeulders, "On the use of mhd mode analysis as a technique for determination of q-profiles in jet plasmas," *Review of Scientific Instruments*, vol. 75, Oct. 2004. DOI: 10.1063/1.1791333.

[31] C. Maggi, E. Delabie, T. Biewer, M. Groth, N. Hawkes, M. Lehnen, E. de la Luna, K. McCormick, C. Reux, F. Rimini, E. Solano, Y. Andrew, C. Bourdelle, V. Bobkov, M. Brix, G. Calabro, A. Czarnecka, J. Flanagan, E. Lerche, and J. Contributors, "L-h power threshold studies in jet with be/w and c wall," *Nuclear Fusion*, vol. 54, Jan. 2014. DOI: 10.1088/0029-5515/54/2/023007.

[32] J. C. Hillesheim, H. Meyer, C. F. Maggi, L. Meneses, E. Poli, and E. Delabie, "Stationary zonal flows during the formation of the edge transport barrier in the jet tokamak," *Physical Review Letters*, vol. 116, no. 6, Feb. 2016, ISSN: 0031-9007. DOI: 10.1103/PhysRevLett.116.065002. [Online]. Available: https://www.osti.gov/biblio/1263871.

[33] E. Solano, N. Vianello, E. Delabie, J. Hillesheim, P. Buratti, D. I. Réfy, I. Balboa, A. Boboc, R. Coelho, B. Sieglin, S. Silburn, P. Drewelow, S. Devaux, D. Dodt, A. Figueiredo, L. Frassinetti, S. Marsen, L. Meneses, C. Maggi, and C. Silva, "Axisymmetric oscillations at l–h transitions in jet: M-mode," *Nuclear Fusion*, vol. 57, p. 022 021, Feb. 2017. DOI: 10.1088/0029-5515/57/2/022021.

[34] G. Birkenmeier, M. Cavedon, G. Conway, P. Manz, U. Stroth, R. Fischer, G. Fuchert, T. Happel, F. Laggner, M. Maraschek, A. Medvedeva, V. Nikolaeva, D. Prisiazhniuk, T. Pütterich, F. Ryter, L. Shao, M. Willensdorfer, E. Wolfrum, and H. Z. and, "Magnetic structure and frequency scaling of limit-cycle oscillations close to l- to h-mode transitions," *Nuclear Fusion*, vol. 56, no. 8, p. 086 009, Jul. 2016. DOI: 10.1088/0029-5515/56/8/086009. [Online]. Available: https://doi.org/10.1088/0029-5515/56/8/086009.